UNIVERSITÀ DEGLI STUDI DI BERGAMO
SCHOOL OF ENGINEERING
DEPARTMENT OF ENGINEERING AND APPLIED SCIENCES
DOCTORAL PROGRAM IN ENGINEERING AND APPLIED SCIENCES

IMPLICIT DISCONTINUOUS GALERKIN METHODS WITH EFFICIENT TIME INTEGRATION FOR INCOMPRESSIBLE VARIABLE DENSITY AND COMPRESSIBLE TURBULENT FLOWS

Doctoral Dissertation of
Francesco Carlo Massa

Tutor
Prof. Francesco Bassi

The Chair of the Doctoral Program
Prof. Valerio Re

2016 – Round XXIX

Abstract

With this research work we want to investigate the use of the state of art implicit high-order time integration schemes to integrate in time high-order Discontinuous Galerkin (DG) space discretization of compressible and incompressible flow model equations. The final goal is to demonstrate the capabilities of an high-order accurate, both in space and time, simulation of turbulent flows. DG methods proved to be very well suited for the Direct Numerical Simulation (DNS) and the Large Eddy Simulation (LES) of turbulent flows thanks to good dissipation and dispersion properties. However, accurate turbulent flow simulations imply long term and stiffly stable time integrations. Explicit Singly Diagonally Implicit Runge-Kutta (ESDIRK) schemes, linearly implicit Rosenbrock-type Runge-Kutta (Rosenbrock) schemes and linearly implicit two-step peer (Peer) methods are implicit time integration schemes that provide very high accuracy combined with excellent stability properties. Nevertheless, since they are implicit schemes they entail the solution of several systems on linear or non-linear equations by means of iterative methods and thus can require an high computational cost. In order to reduce this cost we developed, implemented and validated the automatic step-size control, the initial guess approach and the stopping criterion for iterative methods. Furthermore, we derived a new starting procedure able to preserve the accuracy order of non self-starting multi-step Peer schemes. The potential of the proposed high-order coupling between DG method and implicit temporal schemes has been exhaustively examined on compressible and incompressible benchmark test cases and demonstrated by computing the implicit Large Eddy simulation of massively separated compressible flows over periodic hills at Re = 10595, a challenging and deeply analysed turbulent test case that is part of the test case repository defined inside the EU project TILDA (Towards Industrial LES/DNS in Aero-

nautics - Paving the Way for Future Accurate CFD) at which the Computational Fluid Dynamics group of Universit degli Studi di Bergamo is engaged.

In this work we present, in addition, a high-order Discontinuous Galerkin approach for the simulation of variable density incompressible (VDI) flows developed inside the International Research Training Group project DROPIT (Droplet Interaction Technologies). The purpose of this project is the development of an high accurate and efficient method for the thorough investigation of interface problems for incompressible flows. The method is fully implicit and applies to the VDI NavierStokes equations. More in particular, the density is treated as a purely advected property tracking possibly multiple (more than two) fluids. Furthermore, the fluids interface is captured in a diffuse fashion by the high-degree polynomial solution thus not requiring a geometrical reconstruction and preserving the mass conservation. Density over/undershoots, spurious oscillations at flows interfaces and Godunov numerical fluxes at inter-element boundaries are numerical issues investigated during the development of the present approach. Promising results on numerical experiments involving high-density ratios (water-air) and the possible interaction of more than two fluids have been obtained using a very high-order polynomial representation of the solution on relatively coarse grids.

Summary

Discontinuous Galerkin methods are a class of numerical methods for solving partial differential equations that combine features of the Finite Volume methods (FVM) and of the standard (conforming) Finite Element Methods (FEM). Firstly introduced by Reed and Hill in [56], DG methods have been developed gradually by several authors [1, 10, 11] and nowadays represent a very active field of research [8, 12, 38].

DG discretization approximates the problem solution with piecewise continuous polynomial functions inside mesh elements without imposing continuity constraints between nearby elements. Very high order accurate approximation can be achieved by simply increasing the order of polynomial functions. Furthermore, high geometrical flexibility and numerical compactness are peculiar features of DG that make these schemes very appealing to deal with problems with complex geometries and high parallelization level.

Thanks to its favourable dissipation and dispersion properties, the DG method proved to be very well suited for the Direct Numerical Simulation (DNS) [19, 22, 65], and the Large Eddy Simulation (LES) [62, 63] of turbulent flows. Moreover the application of DG methods to the simulation of multicomponent flows characterized by multiple temporal and physical scales, and where low-order methods often produce a cut-off of the short length scales, seems hence pretty natural as well.

High-order accurate turbulent flow simulations imply long term and stiffly stable time integration. For this reason the choice of the time integration method is crucial for controlling the accuracy of simulations and for enhancing their efficiency. Standard time integration schemes, like explicit Runge-Kutta and implicit backward differentiation formula (BDF2) schemes, do not guarantee high accuracy and stability at the same time. Implicit high-order time

integration schemes, instead, can provide very high accuracy without loosing stability. Therefore, in order to enhance the computational efficiency of DG simulations for turbulent flows, high-order implicit time integration schemes have been recently considered, e.g. Modified Extended Backward Differentiation Formulae (MEBDF) [21, 51] A-stable up to order four, Two Implicit Advanced Step-point (TIAS) [50, 55] A-stable up to order six, Explicit Singly Diagonally Implicit Runge-Kutta schemes (ESDIRK) [43, 52] A-stable up to order five, linearly implicit Rosenbrock-type Runge-Kutta schemes (Rosenbrock) [5,37] A-stable up to order six and linearly implicit two-step peer methods (Peer) [34, 48] A-stable up to order eight.

Despite the advantages in accuracy and stability and the improved efficiency with respect to standard ones, the high order implicit schemes can still remain expensive in terms of computational cost since at each time step they entail the solution of several systems of non-linear or linear equations by means of iterative methods, e.g. quasi-Newton method or Generalized Minimal Residual (GMRES) method.

In this work we focused on the implementation of the high-order implicit ESDIRK, Rosenbrock and Peer schemes inside a solver based on a DG finite element method. Moreover, in order to enhance the robustness and the efficiency of the above mentioned temporal schemes we developed, improved, implemented and validated three numerical strategies: the automatic step-size control, the initial guess approach and the stopping criterion of iterative methods. On the one hand, the automatic step-size control [58,59] is one of the most adopted strategies to increase both robustness and efficiency of the time integration. Indeed, the variable time step approach minimizes the computational effort by adapting the step-size to achieve a user-defined accuracy. Moreover, the time step adaptation limits at each step the local truncation error thus improving the time integration robustness. On the other hand the initial guess approach and the stopping criterion of iterative methods greatly reduce the cost of linear and non-linear system solutions since the former gives a more suitable initial value thus reducing the overall number of iterations and the latter minimises the system over-solving while preserving the local accuracy of the temporal scheme.

Furthermore, in this work we derived a new starting procedure able to preserve the theoretical order of accuracy for multi-step Peer methods.

The potential of the proposed high-order coupling between DG method and implicit temporal schemes and the efficiency of the proposed numerical strategies have been exhaustively examined on compressible and incompressible benchmark test cases and finally demonstrated by computing the implicit Large Eddy simulation of the massively separated compressible flow over periodic hills. This test case has been deeply analysed in the literature [17,32,49] since it offers a number of important features challenging from the point of

view of both turbulence modelling and simulation. Indeed, it is characterized by the formation of a large recirculation area behind the hill crest followed by a post-reattachment-recovery region. These features are difficult to simulate being strongly sensitive to numerical and modelling issues.

The turbulent flow over periodic hills is part of the test case repository defined inside the EU project TILDA (Towards Industrial LES/DNS in Aeronautics - Paving the Way for Future Accurate CFD) at which the Computational Fluid Dynamics group of Universit degli Studi di Bergamo is engaged.

In addition, in this work we investigated a high order Discontinuous Galerkin approach applied to the variable density incompressible (VDI) flow model for the simulation of interface problems. The VDI flow model [36, 47, 66] has very attractive features when dealing with multicomponent flow simulations. Indeed, the model includes the constant density incompressible NavierStokes equations equipped by an overall continuity equation governing the evolution of the density distribution. In particular, thanks to the divergence free constraint, the density is treated as a purely advected property and thus it allows to track possibly multiple (more than two) fluids preserving the mass conservation. Moreover, following a diffuse interface approach, the fluid interface can be handled by means of high-degree polynomials like any other point of the flow without requiring geometrical reconstructions.

Nevertheless, several challenging numerical issues must be taken into account when applying high-order DG methods to multicomponent flows. Above all the density positivity, the proper treatment of the discontinuities of fluid properties across the interface and the opportune definition of interface fluxes are required.

In order to ensure the density positivity we proposed a proper choice of the working variables able, besides, to limit over/undershoots. Furthermore we handled spurious density oscillations at interfaces by adding a local artificial viscosity term to the DG discretization. Finally we derived a new Riemann solver based on the artificial compressibility approach for the inviscid interface flux treatment.

In order to demonstrate the potential of the presented DG approach for the solution of interface problems, several numerical experiments of free surface flows involving also high-density ratios (water-air) and the possible interaction of more than two fluids using a very high-order polynomial representation of the solution on relatively coarse grids have been performed. Results obtained represents the first step of one task of the International Research Training Group project DROPIT (Droplet Interaction Technologies).

Contents

CHAPTER 1

Governing equations

In this chapter will be reported the set of equations used in this thesis work for compressible and incompressible flows.

1.1 Compressible flow model

Using Einstein notation, the continuity and Navier-Stokes equations read

$$\frac{\partial \rho}{\partial t} + \frac{\partial}{\partial x_j}(\rho u_j) = 0, \tag{1.1}$$

$$\frac{\partial}{\partial t}(\rho u_i) + \frac{\partial}{\partial x_j}(\rho u_i u_j) = -\frac{\partial p}{\partial x_i} + \frac{\partial \tau_{ij}}{\partial x_j} + \rho g_i, \tag{1.2}$$

where ρ is the density, p the pressure, $u_{i=1,\dots,d}$ the *i-th* component of the velocity, $g_{i=1,\dots,d}$ the *i-th* component of the body acceleration, τ_{ij} the stress tensor defined as

$$\tau_{ij} = 2\mu \left[\frac{1}{2} \left(\frac{\partial u_i}{\partial x_j} + \frac{\partial u_j}{\partial x_i} \right) - \frac{1}{3} \frac{\partial u_k}{\partial x_k} \delta_{ij} \right], \tag{1.3}$$

μ the dynamic viscosity and d the problem dimension, *i.e.* $d = 1, 2, 3$ for one-, two- and three-dimensional problems respectively. Eqs. (1.1) and (1.2) define a system of $d + 1$ equations in $d + 2$ unknowns.

For compressible flows the problem closure is achieved by adding the energy equation

$$\frac{\partial}{\partial t}(\rho E) + \frac{\partial}{\partial x_j}(\rho H u_j) = \frac{\partial}{\partial x_j}\left[u_i \tau_{ij} - q_j\right] + \rho u_j g_j, \tag{1.4}$$

and a relation between state variables named *equation of state* (EoS). For an ideal gas this equation is called *ideal gas law* and writes

$$p = \rho R T, \tag{1.5}$$

where E is the total energy, H the total enthalpy, q_j the *j-th* component of the heat flux vector, $R = R_0$ the gas constant, T the temperature and

$$E = e + \frac{u_i^2}{2}, \qquad H = h + \frac{u_i^2}{2}, \tag{1.6}$$

$$e = \frac{1}{\gamma - 1} R T, \qquad h = \frac{\gamma}{\gamma - 1} R T, \tag{1.7}$$

$$q_j = -\frac{\mu}{\mathrm{Pr}} \frac{\partial h}{\partial x_j}, \qquad \mu = \mu_0 \left(\frac{T}{T_0}\right)^{\alpha} \tag{1.8}$$

with γ the gas specific heats ratio, Pr the molecular Prandtl number and μ_0, T_0 the dynamic viscosity and the temperature at reference conditions. The body acceleration is typically set constant $|\mathbf{g}| = g = g_0$, *e.g.* the gravitational acceleration. Hereinafter, compressible flows are always referred to an ideal gas.

1.2 Constant density incompressible flow model

For constant density incompressible (CDI) flows the problem closure is typically realised considering the density as a constant value at reference conditions

$$\rho = \rho_0. \tag{1.9}$$

This assumption allows to rewrite the continuity equation (1.1) as the so called *divergence free constraint*

$$\frac{\partial u_j}{\partial x_j} = 0, \tag{1.10}$$

that means the velocity is a solenoidal field. Therefore, the set of the constant density Navier-Stokes equations is

$$\begin{aligned} \frac{\partial u_j}{\partial x_j} &= 0, \\ \frac{\partial u_i}{\partial t} + \frac{\partial}{\partial x_j}(u_i u_j) &= -\frac{\partial}{\partial x_i}\left(\frac{p}{\rho_0}\right) + \frac{\partial}{\partial x_j}\left(\frac{\tau_{ij}}{\rho_0}\right) + g_i, \end{aligned} \tag{1.11}$$

where the dynamic viscosity $\mu = \mu_0$ and the body acceleration $|\mathbf{g}| = g = g_0$ are typically set constant.

1.3 Variable density incompressible flow model

It is possible to derive a more general model for incompressible flows. Indeed, Eq. (1.9) represents only a particular case of the more general incompressible flow assumption

$$\frac{D\rho}{Dt} = 0, \tag{1.12}$$

that reads the material density is constant. Combining Eq. (1.12) with the continuity equation (1.1), the divergence free constraint (1.10) is derived again. Therefore, the set of equations for variable density incompressible flows is

$$\begin{aligned} \frac{\partial u_j}{\partial x_j} &= 0, \\ \frac{\partial}{\partial t}(\rho u_i) + \frac{\partial}{\partial x_j}(\rho u_i u_j) &= -\frac{\partial p}{\partial x_i} + \frac{\partial \tau_{ij}}{\partial x_j} + \rho g_i, \\ \frac{\partial \rho}{\partial t} + \frac{\partial}{\partial x_j}(\rho u_j) &= 0, \end{aligned} \tag{1.13}$$

where the divergence free constraint and the continuity equation must be solved together in order to verify Eq. (1.12). Notice that considering the condition (1.9) the continuity equation collapse to the divergence free constraint and the system (1.11) is recovered. Here the dynamic viscosity can be defined as a suitable function of the density $\mu = \mu(\mu_0, \rho, \rho_0)$ while the body acceleration is typically set constant $|\mathbf{g}| = g = g_0$, where subscripts 0 denotes again quantities at reference conditions.

Since the density is treated as a purely advected property, the system (1.13) is a very appealing model to deal with multicomponent flow problems, *e.g.* free surface flows. In particular the density allows to capture the interface between two or more fluids in an implicit way via the diffuse interface approach which has different advantages:

- interfaces are handled like any other point of the flow,
- mass conservation is ensured by the presence of the continuity equation,
- it allows to deal with multicomponent flows, *i.e.* multi-density flows, without the need of interface reconstruction.

However, this approach has some drawbacks:

- interfaces can be excessively diffused,
- interfaces are not explicitly defined in the sense that the system (1.13) does not provide explicitly the position of the interface,
- the model (1.13) deals only with incompressible flows.

Table 1.1: *Principal reference quantities for compressible flows*

reference quantity	symbol
length	l_r
density	ρ_r
pressure	p_r
gas constant	R_r

Table 1.2: *Principal reference quantities for incompressible flows*

reference quantity	symbol
length	l_r
density	ρ_r
velocity	u_r

1.4 Non-dimensionalization of governing equations

In the present work the dimensionless form of governing equations is obtained considering the set of principal reference quantities reported in Tab. 1.1 and Tab. 1.2 for compressible and incompressible flows respectively. Basing on principal reference quantities all remaining reference quantities can be derived through relations reported in Tab. 1.3 and Tab. 1.4.

Non-dimensional equations are obtained substituting the generic dimensional property ϕ with its non-dimensional value ϕ^* by means the relation

$$\phi = \phi^* \phi_r, \tag{1.14}$$

where ϕ_r is its reference quantity. Defining with ϕ_0 the quantity at reference conditions (*e.g.* experimental conditions), non-dimensional form of governing equations reads

- for compressible flows

$$\begin{aligned}
\frac{\partial \rho^*}{\partial t^*} + \frac{\partial}{\partial x_j^*}(\rho^* u_j^*) &= 0, \\
\frac{\partial}{\partial t^*}(\rho^* u_i^*) + \frac{\partial}{\partial x_j^*}(\rho^* u_i^* u_j^*) &= -\frac{\partial p^*}{\partial x_i^*} + \frac{\partial \tau_{ij}^*}{\partial x_j^*} + \rho^* g_i^*, \\
\frac{\partial}{\partial t^*}(\rho^* E^*) + \frac{\partial}{\partial x_j^*}(\rho^* H^* u_j^*) &= \frac{\partial}{\partial x_j^*}\left[u_i^* \tau_{ij}^* - q_j^*\right] + \rho^* u_j^* g_j^*,
\end{aligned} \tag{1.15}$$

  with

$$p^* = \rho^* R^* T^*, \tag{1.16}$$

$$l_r = l_0, \quad \rho_r = \rho_0, \quad p_r = p_0, \quad R_r = R_0, \tag{1.17}$$

Table 1.3: *Reference quantities relations for compressible flows*

reference quantity	symbol	relation
time	t_r	$l_r \rho_r^{1/2} p_r^{-1/2}$
velocity	u_r	$\rho_r^{-1/2} p_r^{1/2}$
temperature	T_r	$\rho_r^{-1} p_r R_r^{-1}$
dynamic viscosity	μ_r	$l_r \rho_r^{1/2} p_r^{1/2}$
body acceleration	g_r	$l_r^{-1} \rho_r^{-1} p_r$
internal energy	e_r	$\rho_r^{-1} p_r$
enthalpy	h_r	$\rho_r^{-1} p_r$

Table 1.4: *Reference quantities relations for incompressible flows*

reference quantity	symbol	relation
time	t_r	$l_r u_r^{-1}$
pressure	p_r	$\rho_r u_r^2$
dynamic viscosity	μ_r	$l_r \rho_r u_r$
body acceleration	g_r	$l_r^{-1} u_r^2$

and

$$l^* = \frac{l}{l_0}, \tag{1.18}$$

$$\rho^* = \frac{\rho}{\rho_0}, \tag{1.19}$$

$$p^* = \frac{p}{p_0}, \tag{1.20}$$

$$R^* = 1, \tag{1.21}$$

$$t^* = \frac{\sqrt{\mathrm{Eu}}}{\mathrm{St}} \frac{t}{t_0}, \tag{1.22}$$

$$u^* = \frac{1}{\sqrt{\mathrm{Eu}}} \frac{u}{u_0}, \tag{1.23}$$

$$T^* = \frac{T}{T_0}, \tag{1.24}$$

$$\mu^* = \frac{1}{\sqrt{\mathrm{Eu}}\,\mathrm{Re}} \left(\frac{T}{T_0} \right)^{\alpha}, \tag{1.25}$$

$$g^* = \frac{1}{\mathrm{Eu}\,\mathrm{Fr}^2}, \tag{1.26}$$

$$e^* = \frac{1}{\gamma - 1} \frac{T}{T_0}, \tag{1.27}$$

$$h^* = \frac{\gamma}{\gamma - 1} \frac{T}{T_0}, \tag{1.28}$$

- for constant density incompressible flows

$$\begin{aligned} \frac{\partial u_j^*}{\partial x_j^*} &= 0, \\ \frac{\partial u_i^*}{\partial t^*} + \frac{\partial}{\partial x_j^*}(u_i^* u_j^*) &= -\frac{\partial}{\partial x_i^*}\left(\frac{p^*}{\rho^*}\right) + \frac{\partial}{\partial x_j^*}\left(\frac{\tau_{ij}^*}{\rho^*}\right) + g_i^*, \end{aligned} \tag{1.29}$$

with

$$l_r = l_0, \quad \rho_r = \rho_0, \quad u_r = u_0, \tag{1.30}$$

and

$$l^* = \frac{l}{l_0}, \tag{1.31}$$

$$\rho^* = 1, \tag{1.32}$$

$$u^* = \frac{u}{u_0}, \tag{1.33}$$

$$t^* = \frac{1}{\mathrm{St}}\frac{t}{t_0}, \tag{1.34}$$

$$p^* = \mathrm{Eu}\frac{p}{p_0}, \tag{1.35}$$

$$\mu^* = \frac{1}{\mathrm{Re}}, \tag{1.36}$$

$$g^* = \frac{1}{\mathrm{Fr}^2}, \tag{1.37}$$

- for variable density incompressible flows

$$\begin{aligned} \frac{\partial u_j^*}{\partial x_j^*} &= 0, \\ \frac{\partial}{\partial t^*}(\rho^* u_i^*) + \frac{\partial}{\partial x_j^*}(\rho^* u_i^* u_j^*) &= -\frac{\partial p^*}{\partial x_i^*} + \frac{\partial \tau_{ij}^*}{\partial x_j^*} + \rho^* g_i^*, \\ \frac{\partial \rho^*}{\partial t^*} + \frac{\partial}{\partial x_j^*}(\rho^* u_j^*) &= 0, \end{aligned} \tag{1.38}$$

with

$$l_r = l_0, \quad \rho_r = \rho_0, \quad u_r = u_0, \tag{1.39}$$

and

$$l^* = \frac{l}{l_0}, \tag{1.40}$$

$$\rho^* = \frac{\rho}{\rho_0}, \tag{1.41}$$

$$u^* = \frac{u}{u_0}, \tag{1.42}$$

$$t^* = \frac{1}{\mathrm{St}}\frac{t}{t_0}, \tag{1.43}$$

$$p^* = \mathrm{Eu}\frac{p}{p_0}, \tag{1.44}$$

$$\mu^* = \frac{1}{\mathrm{Re}} f(\rho^*), \tag{1.45}$$

$$g^* = \frac{1}{\mathrm{Fr}^2}, \tag{1.46}$$

where

$$\begin{aligned} \mathrm{St} &= \frac{l_0}{t_0 u_0}, \qquad & \mathrm{Re} &= \frac{\rho_0 u_0 l_0}{\mu_0}, \\ \mathrm{Fr} &= \frac{u_0}{\sqrt{g_0 l_0}}, \qquad & \mathrm{Eu} &= \frac{p_0}{\rho_0 u_0^2}, \end{aligned} \tag{1.47}$$

are the Strouhal, Reynolds, Froude and Euler numbers respectively. We remember for compressible flows that from the ideal gas law (1.5) follows

$$\mathrm{Eu} = \frac{1}{\gamma \mathrm{M}^2}, \tag{1.48}$$

where $\mathrm{M} = u_0/\sqrt{\gamma R_0 T_0}$ is the Mach number.

All non-dimensional quantities have been here derived imposing that principal reference quantities (Tab. 1.1 and 1.2) are equal to respective quantities at reference conditions (subscript 0). However, for some flow problems it could be useful considering other values of principal reference quantities. For this purpose we define the generic ratio

$$\alpha_\phi = \frac{\phi_r}{\phi_0}, \tag{1.49}$$

and therefore obtain

- for compressible flows

$$\alpha_l = \frac{l_r}{l_0}, \quad \alpha_\rho = \frac{\rho_r}{\rho_0}, \quad \alpha_p = \frac{p_r}{p_0}, \quad \alpha_R = \frac{R_r}{R_0}, \tag{1.50}$$

with, from relations in Tab. 1.3

$$\alpha_t = \frac{t_r}{t_0} = \frac{\mathrm{St}}{\sqrt{\mathrm{Eu}}}\,\alpha_l\sqrt{\frac{\alpha_\rho}{\alpha_p}}, \tag{1.51}$$

$$\alpha_u = \frac{u_r}{u_0} = \sqrt{\mathrm{Eu}}\,\sqrt{\frac{\alpha_p}{\alpha_\rho}}, \tag{1.52}$$

$$\alpha_T = \frac{T_r}{T_0} = \frac{\alpha_p}{\alpha_\rho\alpha_R}, \tag{1.53}$$

$$\alpha_\mu = \frac{\mu_r}{\mu_0} = \sqrt{\mathrm{Eu}}\,\mathrm{Re}\,\alpha_l\sqrt{\alpha_\rho\alpha_p}, \tag{1.54}$$

$$\alpha_g = \frac{g_r}{g_0} = \mathrm{Eu}\,\mathrm{Fr}^2\,\frac{\alpha_p}{\alpha_l\alpha_\rho}, \tag{1.55}$$

$$\alpha_e = \frac{e_r}{e_0} = (\gamma-1)\,\frac{\alpha_p}{\alpha_\rho}, \tag{1.56}$$

$$\alpha_h = \frac{h_r}{h_0} = \frac{\gamma-1}{\gamma}\frac{\alpha_p}{\alpha_\rho}, \tag{1.57}$$

- and for (both constant and variable density) incompressible flows

$$\alpha_l = \frac{l_r}{l_0}, \quad \alpha_\rho = \frac{\rho_r}{\rho_0}, \quad \alpha_u = \frac{u_r}{u_0}, \tag{1.58}$$

with, from relations in Tab. 1.4

$$\alpha_t = \frac{t_r}{t_0} = \mathrm{St}\,\frac{\alpha_l}{\alpha_u}, \tag{1.59}$$

$$\alpha_p = \frac{p_r}{p_0} = \frac{1}{\mathrm{Eu}}\,\alpha_\rho\alpha_u^2, \tag{1.60}$$

$$\alpha_\mu = \frac{\mu_r}{\mu_0} = \mathrm{Re}\,\alpha_l\alpha_\rho\alpha_u, \tag{1.61}$$

$$\alpha_g = \frac{g_r}{g_0} = \mathrm{Fr}^2\,\frac{\alpha_u^2}{\alpha_l}. \tag{1.62}$$

Finally, combining Eq. (1.14) and Eq. (1.49) for all non-dimensional quantities it follows that

$$\phi^* = \frac{\phi}{\phi_0\alpha_\phi}. \tag{1.63}$$

Hereinafter, for clarity purpose, the superscript $*$ will be neglected and all quantities must be considered as non-dimensional unless otherwise specified.

CHAPTER 2

Space and time discretization

The governing equations both for compressible (1.15) and incompressible (1.29), (1.38) cases can be written in the following compact form

$$\mathbf{D}\frac{\partial \mathbf{u}}{\partial t} + \nabla \cdot \mathbf{F}_c(\mathbf{u}) + \nabla \cdot \mathbf{F}_v(\mathbf{u}, \nabla \mathbf{u}) + \mathbf{s}(\mathbf{u}) = \mathbf{0}, \tag{2.1}$$

where $\mathbf{u} \in \mathbb{R}^m$ is the vector of the m conservative variables, $\mathbf{F}_c, \mathbf{F}_v \in \mathbb{R}^m \otimes \mathbb{R}^d$ are the convective and viscous flux functions, $\mathbf{s}$ is the source term and $\mathbf{D} \in \mathbb{R}^m \otimes \mathbb{R}^m$ is

- for compressible flows the identity matrix

$$\mathbf{D} = \mathbf{I}, \tag{2.2}$$

- for (both constant and variable density) incompressible flows the difference between the identity and a single-entry matrix

$$\mathbf{D} = \mathbf{I} - \mathbf{J}^{11}, \tag{2.3}$$

  where the single-entry matrix is defined as

$$\mathbf{J}^{11} = \begin{cases} 1 & i = 1, j = 1 \\ 0 & \text{otherwise.} \end{cases} \tag{2.4}$$

In the following chapter we will show the high-order space and time discretization of Eqs. (2.1) adopted in this work by means of the Discontinuous Galerkin finite element method and some of the state of art implicit time integration schemes. In particular, we will emphasise the challenging features resulting from the application of such high-order methods to the variable density incompressible flow model for the simulation of multicomponent flow problems.

2.1 The DG discrete setting

Denoted $\mathcal{T}_h = \{K\}$ the mesh of the domain $\Omega \in \mathbb{R}^d, d \in \{2, 3\}$ consisting of non-overlapping arbitrarily shaped elements K such that

$$\overline{\Omega}_h = \bigcup_{K \in \mathcal{T}_h} \overline{K}, \tag{2.5}$$

and basing on the idea to define discrete polynomial spaces in physical coordinates (see [6, 10, 11, 16, 27, 33]) we consider DG approximations built on the space

$$\mathbb{P}_d^k(\mathcal{T}_h) \stackrel{\text{def}}{=} \left\{ v_h \in L^2(\Omega) \,|\, v_{h|K} \in \mathbb{P}_d^k(K),\, \forall K \in \mathcal{T}_h \right\}, \tag{2.6}$$

where k is a non-negative integer and $\mathbb{P}_d^k(K)$ denotes the restriction to K of the polynomial functions of d variables and total degree $\leq k$. To build a satisfactory basis for the space (2.6) we follow the procedure presented in [61] (see also [4,26]) allowing to obtain orthonormal and hierarchical basis functions by means of the modified Gram-Schmidt (MGS) algorithm. The starting set of basis functions for the MGS algorithm are monomials defined over each elementary space $\mathbb{P}_d^k(K)$, $K \in \mathcal{T}_h$, in a reference frame relocated in the element barycenter and aligned with the principal axes of inertia of K.

Afterwards we introduce the set $\mathcal{F}_h$ of the mesh faces $\mathcal{F}_h \stackrel{\text{def}}{=} \mathcal{F}_h^i \cup \mathcal{F}_h^b$, where $\mathcal{F}_h^b$ collects the faces located on the boundary of Ω_h and for any internal face $F \in \mathcal{F}_h^i$ there exist two elements $K^+, K^- \in \mathcal{T}_h$ such that $F \in \partial K^+ \cap \partial K^-$. Moreover, for all $F \in \mathcal{F}_h^b$, $\mathbf{n}_F$ denotes the unit outward normal to Ω_h, whereas, for all $F \in \mathcal{F}_h^i$, $\mathbf{n}_F^-$ and $\mathbf{n}_F^+$ are unit outward normals pointing to K^+ and K^-, respectively. Since a function $v_h \in \mathbb{P}_d^k(\mathcal{T}_h)$ is double valued over an internal face $F \in \mathcal{F}_h^i$, we also introduce the jump $[\![\cdot]\!]$ and average $\{\cdot\}$ trace operators, that are

$$[\![v_h]\!] \stackrel{\text{def}}{=} v_{h|K^+}\mathbf{n}_F^+ + v_{h|K^-}\mathbf{n}_F^-, \qquad \{v_h\} \stackrel{\text{def}}{=} \frac{v_{h|K^+} + v_{h|K^-}}{2}, \tag{2.7}$$

and consider them to act componentwise when applied to vector functions.

Finally, the DG discretization of second-order viscous terms employs the lifting operators $\mathbf{r}_F$ and $\mathbf{r}$. For all $F \in \mathcal{F}_h$, we define the local lifting operator

$\mathbf{r}_F : [L^2(F)]^d \to [\mathbb{P}_d^k(\mathcal{T}_h)]^d$, such that, for all $\mathbf{v} \in [L^2(F)]^d$,

$$\int_\Omega \mathbf{r}_F(\mathbf{v}) \cdot \boldsymbol{\tau}_h d\mathbf{x} = -\int_F \{\boldsymbol{\tau}_h\} \cdot \mathbf{v} dF \quad \forall \boldsymbol{\tau}_h \in [\mathbb{P}_d^k(\mathcal{T}_h)]^d. \tag{2.8}$$

The global lifting operator $\mathbf{r}$ is then defined as

$$\mathbf{r}(\mathbf{v}) \stackrel{\text{def}}{=} \sum_{F \in \mathcal{F}_h} \mathbf{r}_F(\mathbf{v}). \tag{2.9}$$

2.2 DG discretization of governing equations

The system (2.1) can be written in terms of a generic set of variables, *e.g.* conservative variables or primitive variables or another set of variables suitably defined to reach a desired property, named working variables $\mathbf{w}$

$$\mathbf{DP}(\mathbf{w})\frac{\partial \mathbf{w}}{\partial t} + \nabla \cdot \mathbf{F}_c(\mathbf{w}) + \nabla \cdot \mathbf{F}_v(\mathbf{w}, \nabla \mathbf{w}) + \mathbf{s}(\mathbf{w}) = \mathbf{0}, \tag{2.10}$$

where matrix $\mathbf{P}(\mathbf{w})$ takes into account of the transformation from conservative to working variables. The choice of the set of working variables will be analysed in Sec. 2.3.

By multiplying Eq. (2.10) by an arbitrary smooth test function $\mathbf{v} = \{v_1, \ldots, v_m\}$, and integrating by parts, we obtain the weak formulation

$$\begin{aligned}\int_\Omega \mathbf{v} \cdot \left(\mathbf{DP}(\mathbf{w})\frac{\partial \mathbf{w}}{\partial t}\right) d\mathbf{x} - \int_\Omega \nabla \mathbf{v} : [\mathbf{F}_c(\mathbf{w}) + \mathbf{F}_v(\mathbf{w}, \nabla \mathbf{w})]\, d\mathbf{x} \\ + \int_{\partial\Omega} \mathbf{v} \otimes \mathbf{n} : [\mathbf{F}_c(\mathbf{w}) + \mathbf{F}_v(\mathbf{w}, \nabla \mathbf{w})]\, d\sigma + \int_\Omega \mathbf{v} \cdot \mathbf{s}(\mathbf{w}) d\mathbf{x} = \mathbf{0},\end{aligned} \tag{2.11}$$

where $\mathbf{n}$ is the unit vector normal to the boundary.

To discretize Eq. (2.11) we replace the solution $\mathbf{w}$ and the test function $\mathbf{v}$ with a finite element approximation $\mathbf{w}_h$ and a discrete test function $\mathbf{v}_h$, respectively, where $\mathbf{w}_h$ and $\mathbf{v}_h$ belong to the space $\mathbf{V}_h \stackrel{\text{def}}{=} [\mathbb{P}_d^k(\mathcal{T}_h)]^m$. For each of the m equations of system (2.11) and for any element K, without loss of generality we choose as the set of shape and test functions the set $\{\phi\}$ of N_{dof}^K orthogonal and hierachical basis functions in that element. With this choice each component $w_{h,j}$, $j = 1, \ldots, m$, of $\mathbf{w}_h \in \mathbf{V}_h$ can be expressed, in terms of the elements of the global vector $\mathbf{W}$ of unknown degrees of freedom (DoF), as $w_{h,j} = \phi_l W_{j,l}$, $l = 1, \ldots, N_{dof}^K$, $\forall K \in \mathcal{T}_h$. Therefore, the DG discretization of the governing equations consists in seeking, for $j = 1, \ldots, m$, the elements of

$\mathbf{W}$ such that

$$\sum_{T\in\mathcal{T}_h}\int_T \phi_i D_{j,t}P_{t,k}\left(\mathbf{w}_h\right)\phi_l\frac{dW_{k,l}}{dt}d\mathbf{x} - \sum_{T\in\mathcal{T}_h}\int_T \frac{\partial\phi_i}{\partial x_n}\left[F_{c,j,n}\left(\mathbf{w}_h\right)+F_{v,j,n}\left(\mathbf{w}_h,\nabla_h\mathbf{w}_h+\mathbf{r}\left(\left[\!\left[\mathbf{w}_h\right]\!\right]\right)\right)\right]d\mathbf{x} + \sum_{F\in\mathcal{F}_h}\int_F \left[\!\left[\phi_i\right]\!\right]_n\left[\widehat{F}_{c,j,n}\left(\mathbf{w}_h^{\pm}\right)+\widehat{F}_{v,j,n}\left(\mathbf{w}_h^{\pm},\left(\nabla_h\mathbf{w}_h+\eta_F\mathbf{r}_F\left(\left[\!\left[\mathbf{w}_h\right]\!\right]\right)\right)^{\pm}\right)\right]d\sigma + \sum_{T\in\mathcal{T}_h}\int_T \phi_i s_j\left(\mathbf{w}_h\right)d\mathbf{x}=0, \quad (2.12)$$

for $i=1,\ldots,N_{dof}^K$. Repeated indices imply summation over ranges $k=1,\ldots,m$, $l=1,\ldots,N_{dof}^K$, $n=1,\ldots,d$. Moreover, integrating again by parts the inviscid flux we obtain the strong formulation (at least for the convective term)

$$\sum_{T\in\mathcal{T}_h}\int_T \phi_i D_{j,t}P_{t,k}\left(\mathbf{w}_h\right)\phi_l\frac{dW_{k,l}}{dt}d\mathbf{x} + \sum_{T\in\mathcal{T}_h}\int_T \phi_i\frac{\partial}{\partial x_n}F_{c,j,n}\left(\mathbf{w}_h\right)d\mathbf{x} - \sum_{T\in\mathcal{T}_h}\int_T \frac{\partial\phi_i}{\partial x_n}F_{v,j,n}\left(\mathbf{w}_h,\nabla_h\mathbf{w}_h+\mathbf{r}\left(\left[\!\left[\mathbf{w}_h\right]\!\right]\right)\right)d\mathbf{x} + \sum_{F\in\mathcal{F}_h}\int_F \left[\!\left[\phi_i\right]\!\right]_n\left[\widehat{F}_{c,j,n}\left(\mathbf{w}_h^{\pm}\right)-F_{c,j,n}\left(\mathbf{w}_h^{\pm}\right)\right]d\sigma + \sum_{F\in\mathcal{F}_h}\int_F \left[\!\left[\phi_i\right]\!\right]_n\widehat{F}_{v,j,n}\left(\mathbf{w}_h^{\pm},\left(\nabla_h\mathbf{w}_h+\eta_F\mathbf{r}_F\left(\left[\!\left[\mathbf{w}_h\right]\!\right]\right)\right)^{\pm}\right)d\sigma + \sum_{T\in\mathcal{T}_h}\int_T \phi_i s_j\left(\mathbf{w}_h\right)d\mathbf{x}=0. \quad (2.13)$$

Weak and strong formulations are mathematically equivalent but computationally different [39]. To the authors' knowledge there is not jet a clear way to define a priori what kind of formulation is more advisable. Basing on our experience in this work we use the strong formulation for variable density incompressible flows because it showed to be more robust with respect to weak one when dealing with incompressible multicomponent problems with very high density ratios. Conversely, since for compressible and constant density incompressible flows no differences in robustness are found for the two formulation, the weak one is implemented.

The DG discretization of the viscous fluxes is based on the BR2 scheme, proposed in [11] and theoretically analyzed in [18] and [1]. Following this scheme, the viscous numerical flux is given by

$$\widehat{\mathbf{F}}_v\left(\mathbf{w}_h^{\pm}, \left(\nabla_h \mathbf{w}_h + \eta_F \mathbf{r}_F\left(\llbracket \mathbf{w}_h \rrbracket\right)\right)^{\pm}\right) \stackrel{\text{def}}{=} \left\{\mathbf{F}_v\left(\mathbf{w}_h, \nabla_h \mathbf{w}_h + \eta_F \mathbf{r}_F\left(\llbracket \mathbf{w}_h \rrbracket\right)\right)\right\} \tag{2.14}$$

where the stability parameter η_F is defined accordingly to [1].

The convective numerical flux is computed from the solution of local Riemann problems in the normal direction at each integration point on elements boundaries. For compressible flows, the exact Riemann solver of Gottlieb and Groth [35] is used. For CDI flows, the approach proposed in [6] is employed, whereby the convective numerical flux is computed from the exact solution of local Riemann problems modified by means of an artificial compressibility perturbation. Finally, for VDI flows, following the approach of the artificial compressibility perturbation we define a new local Riemann problem able to take into account of density contributes to interface inviscid fluxes. This new approach is reported in detail in Sec. 2.5.

2.2.1 DG boundary condition treatment

The DG discretization is very well suited to weakly enforce boundary conditions, [7, 11]. This can be achieved by properly defining at each integration point on boundaries the state $\mathbf{w}^b$ and its gradient $\nabla \mathbf{w}^b$ which are used to compute the numerical convective and viscous fluxes and the lifting operators for all $F \in \mathcal{F}_h^b$.

At inflow, outflow, and farfield boundaries the state $\mathbf{w}^b$, defined using prescribed boundary data and the Riemann invariants related to the outgoing characteristics, enters in the Riemann solver and allows to compute, together with the internal state $\mathbf{w}_h^-$, the numerical convective flux. For these types of boundaries, the gradient is defined as

$$\nabla \mathbf{w}^b = \nabla \mathbf{w}_h^- + \eta_F \mathbf{r}_F\left(\llbracket \mathbf{w} \rrbracket^b\right), \tag{2.15}$$

where $\mathbf{r}_F(\llbracket \mathbf{w} \rrbracket^b)$ is the lifting associated to the jump between $\mathbf{w}^b$ and $\mathbf{w}_h^-$.

For solid wall boundaries, the state $\mathbf{w}^b$ and its gradient $\nabla \mathbf{w}^b$ are defined exactly at the wall. In particular, the state at the wall has zero velocity relative to the boundary and its pressure is determined from the analytical solution of the Riemann problem for a flow moving towards (or away from) the wall with the normal velocity component of the internal state. For compressible flows, the energy conservation equation requires a boundary condition either for the wall temperature, which is set in the state $\mathbf{w}^b$, or for the wall heat flux, which is proportional to the normal component of the temperature gradient $\nabla \mathbf{w}^b$ at the wall.

2.3 Working variables

The transformation matrix $\mathbf{P}(\mathbf{w})$ in Eq. (2.10) allows to solve the system of governing equation for a set of working variables that differs from the conservative ones $\mathbf{u}$. More in particular for each possible set of $\mathbf{w}$ for which $\mathbf{u} = \mathbf{u}(\mathbf{w})$ the matrix verifies

$$\frac{\partial \mathbf{u}}{\partial t} = \mathbf{P}(\mathbf{w}) \frac{\partial \mathbf{w}}{\partial t}. \tag{2.16}$$

Thus we define

$$\mathbf{P}(\mathbf{w}) = \frac{\partial \mathbf{u}}{\partial \mathbf{w}}. \tag{2.17}$$

2.3.1 Compressible flows

For compressible flows, the set of primitive variables (p, u_i, T) is widely used especially when dealing with low Mach number [23, 66] and recently it also proved to be effective in the context of high-order DG approximations [9]. Primitive variables allow an easier and more efficient computation of the contributions to the Jacobian matrix related to the viscous terms discretization and to the implicit treatment of boundary conditions. Furthermore, they offer the possibility to ensure the positivity of all thermodynamic variables at the discrete level. For this purpose it is sufficient to apply the DG polynomial approximation for *logarithms* of pressure and temperature [3, 5]

$$\widetilde{p} = \ln(p), \qquad \widetilde{T} = \ln(T). \tag{2.18}$$

Indeed, pressure and temperature values computed as

$$p = e^{\widetilde{p}}, \qquad T = e^{\widetilde{T}}, \tag{2.19}$$

are always positive. Therefore, defining the set of working variables for compressible flows as

$$\mathbf{w} = [\widetilde{p}, u_i, \widetilde{T}]^T, \tag{2.20}$$

and writing the set of conservative variables as

$$\mathbf{u} = \mathbf{u}(\mathbf{w}) = \begin{bmatrix} \rho \\ \rho u_i \\ \rho E \end{bmatrix} = \begin{bmatrix} \exp(\widetilde{p} - \widetilde{T}) \\ \exp(\widetilde{p} - \widetilde{T}) u_i \\ \dfrac{\exp(\widetilde{p})}{\gamma - 1} + \exp(\widetilde{p} - \widetilde{T}) \dfrac{u_i^2}{2} \end{bmatrix}, \tag{2.21}$$

the transformation matrix between $\mathbf{u}$ and $\mathbf{w}$ reads

$$\mathbf{P}(\mathbf{w}) = \begin{bmatrix} \rho_{\widetilde{p}} & 0 & 0 & 0 & \rho_{\widetilde{T}} \\ \rho_{\widetilde{p}} u_1 & \rho & 0 & 0 & \rho_{\widetilde{T}} u_1 \\ \rho_{\widetilde{p}} u_2 & 0 & \rho & 0 & \rho_{\widetilde{T}} u_2 \\ \rho_{\widetilde{p}} u_3 & 0 & 0 & \rho & \rho_{\widetilde{T}} u_3 \\ \rho_{\widetilde{p}} E & \rho E_{u_1} & \rho E_{u_2} & \rho E_{u_3} & \rho_{\widetilde{T}} E + \rho E_{\widetilde{T}} \end{bmatrix}, \tag{2.22}$$

where

$$\rho_{\widetilde{p}} = \left.\frac{\partial \rho}{\partial \widetilde{p}}\right|_{u_i, \widetilde{T}} = \rho, \qquad \rho_{\widetilde{T}} = \left.\frac{\partial \rho}{\partial \widetilde{T}}\right|_{\widetilde{p}, u_i} = -\rho, \tag{2.23}$$

$$E_{u_i} = \left.\frac{\partial E}{\partial u_i}\right|_{\widetilde{p}, \widetilde{T}} = u_i, \qquad E_{\widetilde{T}} = \left.\frac{\partial E}{\partial \widetilde{T}}\right|_{\widetilde{p}, u_i} = \frac{\exp(\widetilde{T})}{\gamma - 1}. \tag{2.24}$$

2.3.2 Constant density incompressible flows

For constant density incompressible flows it is quite natural to use the set of primitive variables

$$\mathbf{w} = [p, u_i]^T, \tag{2.25}$$

since from condition (1.9) $\mathbf{u} = \mathbf{w}$. Therefore, the transformation matrix is simply the identity matrix

$$\mathbf{P} = \mathbf{I}. \tag{2.26}$$

2.3.3 Variable density incompressible flows

In order to define the set of working variables for VDI flows it could be useful considering two important issues. The first one is that here the density is no more constant and thus it must be ensured its positivity. The second one concerns density under/overshoots deriving from the discretization of discontinuities inside density field, *i.e.* density interfaces when dealing with multicomponent flow problems.

In this work we handle both issues by discretizing and evolving in time a new density variable $\widetilde{\rho}$ which is defined in such a way that

$$\begin{aligned} \rho &= \frac{\rho_+ + \sigma_l \rho_-}{2}\left(1 + \tanh(\sigma_s \widetilde{\rho})\right) + \frac{\rho_- - \sigma_l \rho_-}{2}\left(1 - \tanh(\sigma_s \widetilde{\rho})\right) = \\ &= \rho_+ \frac{r_\rho + 1 + (r_\rho - 1 + 2\sigma_l)\tanh(\sigma_s \widetilde{\rho})}{2 r_\rho}, \end{aligned} \tag{2.27}$$

and thus

$$\widetilde{\rho} = \frac{1}{2\sigma_s} \ln\left(\frac{r_\rho \dfrac{\rho}{\rho_+} - 1 + \sigma_l}{-r_\rho \dfrac{\rho}{\rho_+} + r_\rho + \sigma_l} \right), \tag{2.28}$$

where ρ_+ (resp. ρ_-) is the user-defined maximum (resp. minimum) density field value, $r_\rho = \rho_+/\rho_-$ is the maximum density ratio and $\sigma_l \in \mathbb{R}^+$, $\sigma_s \in \mathbb{R}\backslash\{0\}$ are respectively the limiter and the scaling factors.

The limiter factor σ_l defines the infimum and the supremum of the hyperbolic transformation (2.27) as

$$\inf(\rho) = \rho_- - \sigma_l\rho_-, \qquad \sup(\rho) = \rho_+ + \sigma_l\rho_-. \tag{2.29}$$

By choosing $\sigma_l = 0$ it is clear that density under/overshoots are avoided since $\inf(\rho) = \rho_-$ and $\sup(\rho) = \rho_+$. However from Eq. (2.28) this choice implies that $\inf(\widetilde{\rho}) \to -\infty$ and $\sup(\widetilde{\rho}) \to +\infty$ thus making difficult to handle the $\widetilde{\rho}$ discretization. Therefore, in order to reduce as much as possible the magnitude of $\widetilde{\rho}$ meanwhile preserving the density positivity, we impose $\sigma_l = 1$ so that

$$\inf(\rho) = 0, \qquad \sup(\rho) = \rho_+ + \rho_-. \tag{2.30}$$

As a consequence, under/overshoots are admitted during simulations still being restricted to ρ_- value.

The scaling factor σ_s is a free parameter that can be set in order to limit the initial range $\Delta\widetilde{\rho} = \widetilde{\rho}(\rho_+) - \widetilde{\rho}(\rho_-)$ of the working variable $\widetilde{\rho}$ to the maximum value $\Delta_i\widetilde{\rho}$

$$\sigma_s = \max\left[\frac{1}{\Delta_i\widetilde{\rho}}\ln\left(\frac{r_\rho - 1 + \sigma_l}{\sigma_l}\right); 1\right]. \tag{2.31}$$

Hereafter we simply consider $\Delta_i\widetilde{\rho} = 1$.

The set of working variable is thus

$$\mathbf{w} = [p, u_i, \widetilde{\rho}]^T, \tag{2.32}$$

and starting from conservative variables $\mathbf{u} = [p, \rho u_i, \rho]^T$, the transformation matrix reads

$$\mathbf{P}(\mathbf{w}) = \begin{bmatrix} 1 & 0 & 0 & 0 & 0 \\ 0 & \rho & 0 & 0 & \rho_{\widetilde{\rho}}u_1 \\ 0 & 0 & \rho & 0 & \rho_{\widetilde{\rho}}u_2 \\ 0 & 0 & 0 & \rho & \rho_{\widetilde{\rho}}u_3 \\ 0 & 0 & 0 & 0 & \rho_{\widetilde{\rho}} \end{bmatrix}, \tag{2.33}$$

where

$$\rho_{\widetilde{\rho}} = \left.\frac{\partial\rho}{\partial\widetilde{\rho}}\right|_{p,u_i} = \sigma_s\rho_+\frac{r_\rho - 1 + 2\sigma_l}{2r_\rho\cosh^2(\sigma_s\widetilde{\rho})}. \tag{2.34}$$

We remember that, conversely to compressible flows, the (both constant and variable density) incompressible flow solution does not require to verify the positivity of pressure field at discrete level.

2.4 Discontinuities treatment for incompressible multicomponent problems

In the previous section we introduced for variable density incompressible flows the working variable $\widetilde{\rho}$ with the goal to ensure the positivity of density and to limit the oscillations on ρ arising from higher order DG approximations of density discontinuities when dealing with multicomponent problems. However, it must be clear that this strategy does not numerically control Gibbs-type phenomena. Therefore, a proper treatment of density oscillations must be introduced in order to enhance the robustness of the discretization.

For this purpose we decide to use the treatment of jumps proposed by Persson and Peraire [53] and based on shock capturing strategies inspired by early artificial viscosity methods [64]. For the sake of simplicity we can consider the generic conservation law for the variable q

$$\frac{\partial q}{\partial t} + \nabla \cdot \mathbf{F}(q) = 0, \tag{2.35}$$

with $\mathbf{F}(q)$ the fluxes vector. If the conserved variable q shows discontinuities inside the domain, higher order approximations lead to oscillations of the solution which can generate strong instabilities. The key idea of the shock capturing strategy is to add an artificial viscosity term inside the original equation

$$\frac{\partial q}{\partial t} + \nabla \cdot \mathbf{F}(q) = \nabla \cdot (\epsilon \nabla q)\,. \tag{2.36}$$

The parameter ϵ controls the amount of the viscosity and, as suggested in [53], when attempting to resolve jumps it should be defined as a function of the ratio between the element dimension (h) and the DG polynomial order ($p = k + 1$)

$$\epsilon \propto \mathcal{O}(h/p). \tag{2.37}$$

Away from discontinuities instead it should be set null ($\epsilon = 0$). This strategy fits very well with DG approximation since introduces a small quantity of viscosity which decreases with higher polynomial order allowing to capture discontinuities as thin layers with continuous sharp gradients inside a single mesh element.

The choice of the smoothness sensor that detects discontinuities inside the domain (and thus defines ϵ value) is obviously a critical element of this approach. Persson and Peraire proposed a sensor based on the modal decay of the coefficients q_l in the DG polynomial expansion

$$q_h = \phi_l q_l, \tag{2.38}$$

where $\phi_{l=1,\dots,N_{dof}^K}$ are hierarchical and orthogonal basis functions and $q_h \in \mathbb{P}_d^k(T)$. When the solution is smooth these coefficients are expected to decay

quickly. If we represent approximately the decay as an asymptotic behaviour

$$|q_l| \propto c\, l^{-s}, \qquad \forall l = 1, \dots, N_{dof}^K, \tag{2.39}$$

this means that the exponent s, that can be found through least-squares fitting, has very high values ($s \gg 1$). Conversely for non smooth solutions, *i.e.* jumps on variable q, the decay shows an exponent $s \approx 1$. More in detail, in analogy with Fourier modal decay, it is expected that $s \approx 1$ for discontinuous solutions inside the element ($u \notin C^0$), $s \approx 2$ for $u \in C^0 \setminus C^1$, $s \approx 3$ for $u \in C^1 \setminus C^2$ and so on. However, Klöckner *et al.* showed in [44] that due to even-odd effects, *i.e.* non monotone decays, a direct use of parameter s as smoothness sensor can lead to misleading results in jumps detection. For this reason they proposed a new procedure to define s, termed skyline pessimization, that defines a new set of modal coefficients

$$\overline{q}_n = \max_{i=\min(n,k-1),\dots,k} (\hat{q}_i), \tag{2.40}$$

where $n \in \{1, 2, \dots, k\}$ is the mode number and

$$\hat{q}_i = \max_{l=l_i,\dots,l_{i+1}-1} |q_l|, \tag{2.41}$$

with $[l_i, \dots, l_{i+1} - 1]$ the DoFs associated to the i-*th* mode. Then, basing on the asymptotic behaviour

$$\overline{q}_n \propto c\, m^{-s_n}, \qquad \forall n = 1, \dots, k, \tag{2.42}$$

where $m \in [\min(n, k-1), k]$ is the mode for which $\hat{q}_m = \overline{q}_n$, they compute each exponent

$$s_n = \frac{\ln(\overline{q}_n)}{\ln\left(\dfrac{1}{m}\right)}, \tag{2.43}$$

and define the smoothness sensor as the minimum of all exponent values

$$s = \min_n (s_n). \tag{2.44}$$

Once computed the smoothness sensor inside a mesh element, following the choice of Perrson and Peraire the artificial viscosity is set as

$$\epsilon = \begin{cases} \epsilon_0 & \text{if} \quad s < s_0 - \Delta s \\ \dfrac{\epsilon_0}{2}\left[1 - \sin\left(\pi \dfrac{s_0 - s}{2\Delta s}\right)\right] & \text{if} \quad s_0 - \Delta s \le s \le s_0 + \Delta s \\ 0 & \text{otherwise}, \end{cases} \tag{2.45}$$

where $\epsilon_0 \propto \mathcal{O}(h/p)$ is the maximum value of the artificial viscosity, s_0 is the user-defined threshold value of the smoothness sensor and $2\Delta s$ is the range of

smoothness sensor value for which the viscosity assumes intermediate values between 0 and ϵ_0.

The approach above described is here applied to VDI equation in order to control density oscillations when dealing with incompressible multicomponent flow problems. The artificial viscosity modified set of equations for VDI flows reads

$$\begin{aligned} \frac{\partial u_j}{\partial x_j} &= 0, \\ \frac{\partial}{\partial t}(\rho u_i) + \frac{\partial}{\partial x_j}(\rho u_i u_j) &= -\frac{\partial p}{\partial x_i} + \frac{\partial \tau_{ij}}{\partial x_j} + \rho g_i + u_i \frac{\partial}{\partial x_j}\left(\epsilon \frac{\partial \rho}{\partial x_j}\right), \\ \frac{\partial \rho}{\partial t} + \frac{\partial}{\partial x_j}(\rho u_j) &= \frac{\partial}{\partial x_j}\left(\epsilon \frac{\partial \rho}{\partial x_j}\right). \end{aligned} \tag{2.46}$$

Notice that we added the artificial viscosity term not only to the continuity equation, which rules the evolution of the density, but also to the momentum equation. With this particular choice we take into account of the effects of the artificial viscosity term on the density evolution on both equations. An interesting consequence is that the non-conservative form of the momentum equation is maintained independent from the artificial viscosity term. Indeed, combining the momentum equation with the continuity equation written in Eq. (2.46) we get

$$\frac{\partial u_i}{\partial t} + u_j \frac{\partial u_i}{\partial x_j} = -\frac{1}{\rho}\frac{\partial p}{\partial x_i} + \frac{1}{\rho}\frac{\partial \tau_{ij}}{\partial x_j} + g_i. \tag{2.47}$$

We point out that all simulations performed without the additional artificial viscosity term to the momentum equation led to meaningless solutions.

The smoothness sensor s is here defined on the modal decay of the working variable $\widetilde{\rho}$ and the parameters used for the shock capturing technique are set

$$s_0 = 1, \qquad \Delta s = 0.75, \qquad \epsilon_0 = c\frac{h}{p}, \tag{2.48}$$

where the constant c is considered unitary unless otherwise specified.

The introduction of the artificial viscosity term however requires the discretization of second order derivatives that must be opportrunely treated from the Godunov numerical fluxes point of view. In order to avoid this issue we follow the idea proposed by Jaffre *et al.* in [42] which treat the artificial viscous term as a source term. Therefore, only the volume contribute is consider and reads

$$\sum_{T\in\mathcal{T}_h} \int_T b_{\epsilon,j} \frac{\partial \phi_i}{\partial x_n} F_{\epsilon,j,n} \left(\nabla_h \mathbf{w}_h\right) d\mathbf{x}, \tag{2.49}$$

where, from Eq. (2.46)

$$\mathbf{b}_\epsilon = \begin{bmatrix} 0 \\ u_i \\ 1 \end{bmatrix}, \qquad \mathbf{F}_\epsilon(\nabla \mathbf{w}) = \begin{bmatrix} 0 \\ \epsilon \nabla \rho \\ \epsilon \nabla \rho \end{bmatrix}. \tag{2.50}$$

Finally, we point out that the mass conservation is still preserved since the artificial viscosity is applied only to the density gradient and thus does not affect the mean value inside the element.

2.5 Riemann solver for variable density incompressible flows

In order to compute Godunov numerical fluxes for VDI flows, in this work we define a new Riemann solver based on the artificial compressibility method following the previous works of Elsworth and Toro [31] and Bassi *et al.* [6] for CDI flows.

The local planar VDI set of equation modified by means of the artificial compressibility term is

$$\begin{aligned} \frac{1}{\rho c^2}\frac{\partial p}{\partial t} + \frac{\partial q_n}{\partial x} &= 0 \\ \frac{\partial \rho q_n}{\partial t} + \frac{\partial (\rho q_n^2 + p)}{\partial x} &= 0 \\ \frac{\partial \rho \theta}{\partial t} + \frac{\partial (\rho \theta q_n)}{\partial x} &= 0 \\ \frac{\partial \rho}{\partial t} + \frac{\partial (\rho q_n)}{\partial x} &= 0, \end{aligned} \tag{2.51}$$

where the hyperbolic nature of equations is restored by adding the artificial compressibility term to the the divergence free constraint. Here $c \in \mathbb{R} \setminus \{0\}$ is the artificial compressibility coefficient and q_n and θ are the normal and the tangential velocities to the element edge, respectively. x denotes a locally defined axis oriented as the normal vector pointing out of the element K^+ with origin at point P (see Fig. 2.1).

The problem (2.51) can be written in a conservative form by considering the density ρ that appears in the divergence and the momentum equations as a constant quantity $\widehat{\rho}$. This simplifying assumption allows to decouple the velocity and the pressure evolutions from the density field. Moreover, θ can be now considered as a generic conserved property, *i.e.* both density and tangential velocity. Therefore, the local planar artificial compressibility VDI system of equations becomes

$$\frac{\partial \mathbf{w}}{\partial t} + \frac{\partial \mathbf{F}(\mathbf{w})}{\partial x} = \mathbf{0}, \tag{2.52}$$

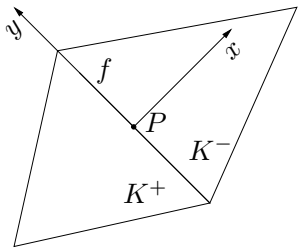

Figure 2.1: *Local frame at quadrature point P on edge f.*

with

$$\mathbf{w} = \begin{bmatrix} p \\ q_n \\ \theta \end{bmatrix}, \qquad \mathbf{F}(\mathbf{w}) = \begin{bmatrix} \widehat{\rho} c^2 q_n \\ q_n^2 + \dfrac{p}{\widehat{\rho}} \\ \theta q_n \end{bmatrix}. \tag{2.53}$$

The Jacobian matrix is given by

$$\mathbf{A} = \frac{\partial \mathbf{F}(\mathbf{w})}{\partial \mathbf{w}} = \begin{bmatrix} 0 & \widehat{\rho} c^2 & 0 \\ \dfrac{1}{\widehat{\rho}} & 2q_n & 0 \\ 0 & \theta & q_n \end{bmatrix}, \tag{2.54}$$

and eigenvalues vector $\boldsymbol{\lambda}$ and left and right eigenvector matrices $\mathbf{L}$ and $\mathbf{R}$ are

$$\boldsymbol{\lambda} = \begin{bmatrix} q_n - a \\ q_n \\ q_n + a \end{bmatrix},$$

$$\mathbf{L} = \begin{bmatrix} \dfrac{1}{\widehat{\rho}} & q_n - a & 0 \\ -\dfrac{1}{\widehat{\rho}} & -q_n & \dfrac{a^2}{\theta} \\ \dfrac{1}{\widehat{\rho}} & q_n + a & 0 \end{bmatrix}, \tag{2.55}$$

$$\mathbf{R} = \frac{1}{2a} \begin{bmatrix} \widehat{\rho}(q_n + a) & 0 & -\widehat{\rho}(q_n - a) \\ -1 & 0 & 1 \\ \dfrac{\theta}{a} & \dfrac{2\theta}{a} & \dfrac{\theta}{a} \end{bmatrix},$$

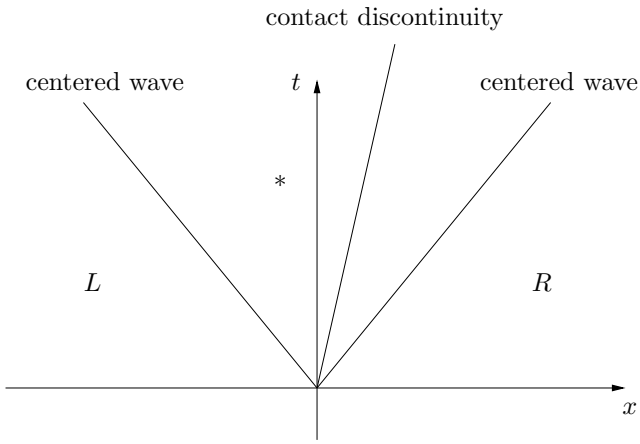

Figure 2.2: *Structure of the Riemann problem.*

where

$$a = \sqrt{q_n^2 + c^2}. \tag{2.56}$$

By definitions of c and a is clear that $\lambda_1 < 0$, $\lambda_3 > 0$ and $\lambda_1 < \lambda_2 < \lambda_3$.

Starting from the piece-wise constant initial datum

$$\mathbf{w}_0 = \begin{cases} \mathbf{w}_L & x < 0 \\ \mathbf{w}_R & x > 0, \end{cases} \tag{2.57}$$

the exact solution of the local problem (2.52) can be found following the procedure described in [6, 31]. The Riemann problem solution entails four states separated by two centered waves, hereafter called left (L) and right (R) waves and associated with the eigenvalues λ_1 and λ_3 respectively, and a contact discontinuity referred to the eigenvalue λ_2 (see Fig. 2.2). Left and right waves can be either rarefaction or shock waves depending on $\mathbf{w}_0$ and across them all the unknowns $\mathbf{w}$ can change. Instead, in the region between waves, called *star region* ($\star$), pressure and normal velocity are constant and only the conserved property θ can vary. Since the star region holds the Riemann solution on $x/t = 0$ line which is used for the computation of the Godunov numerical fluxes, in the following we describe in detail the procedure to obtain $\mathbf{w}_\star$.

2.5.1 Rarefaction waves and Riemann invariants

The solution across a rarefaction wave can be obtained by means of Riemann invariants $\mathbf{\Gamma}$. Indeed, invariants are conserved inside this kind of wave. In particular Riemann invariants assume constant values along the *caracteristic curves*

$$C_i\,(x,t) = x + \lambda_i t. \tag{2.58}$$

By definition, the gradients of Riemann invariants are the left eigenvectors $\mathbf{L}_i$ of matrix $\mathbf{A}$, where $i = 1, 2, 3$ is the row number of matrix $\mathbf{L}$. It follows that

$$\begin{aligned} d\Gamma_1 = \mathbf{L}_1 \cdot d\mathbf{w} = \frac{1}{\widehat{\rho}} dp + (q_n - a)\, dq_n = 0 \qquad \text{on} \qquad C_1 \\ d\Gamma_2 = \mathbf{L}_2 \cdot d\mathbf{w} = -\frac{1}{\widehat{\rho}} dp - q_n dq_n + \frac{a^2}{\theta} d\theta = 0 \qquad \text{on} \qquad C_2 \\ d\Gamma_3 = \mathbf{L}_3 \cdot d\mathbf{w} = \frac{1}{\widehat{\rho}} dp + (q_n + a)\, dq_n = 0 \qquad \text{on} \qquad C_3. \end{aligned} \tag{2.59}$$

Therefore, Riemann invariants are

$$\begin{aligned} \Gamma_1 = \frac{p}{\widehat{\rho}} + \frac{1}{2}\left[q_n (q_n - a) - c^2 \ln (q_n + a)\right] = const. \quad \text{on} \quad C_1 \\ \Gamma_{2,1} = \frac{\theta}{q_n + a} = const. \quad \text{on} \quad C_2 \cap C_1 \\ \Gamma_{2,3} = \theta (q_n + a) = const. \quad \text{on} \quad C_2 \cap C_3 \\ \Gamma_3 = \frac{p}{\widehat{\rho}} + \frac{1}{2}\left[q_n (q_n + a) + c^2 \ln (q_n + a)\right] = const. \quad \text{on} \quad C_3. \end{aligned} \tag{2.60}$$

For solution purposes it must be pointed out that a left rarefaction is crossed by C_3 and C_2 lines and a right rarefaction by C_1 and C_2 lines.

2.5.2 Shock waves and Rankine-Hugoniot jump conditions

Jumps $\Delta\mathbf{w} = \mathbf{w}_2 - \mathbf{w}_1$ and $\Delta\mathbf{F} = \mathbf{F}(\mathbf{w}_2) - \mathbf{F}(\mathbf{w}_1)$ across a shock are related to each other by means of Rankine-Hugoniot conditions

$$\Delta\mathbf{F} = s\Delta\mathbf{w}, \tag{2.61}$$

where here s is the shock speed. Apply (2.61) to (2.53) gives

$$\begin{aligned} \widehat{\rho} c^2 \Delta q_n = s\Delta p \\ \Delta q_n^2 + \frac{\Delta p}{\widehat{\rho}} = s\Delta q_n \\ \Delta (\theta q_n) = s\Delta\theta. \end{aligned} \tag{2.62}$$

It follows that

$$\begin{aligned} \frac{p_2 - p_1}{\widehat{\rho}} = \frac{c^2 (q_{n2} - q_{n1})}{s} \\ \frac{\theta_2}{\theta_1} = \frac{q_{n1} - s}{q_{n2} - s}, \end{aligned} \tag{2.63}$$

with the shock speed computed combining the first two relations of (2.62)

$$s_\pm = \frac{q_{n2} + q_{n1}}{2} \pm \sqrt{\left(\frac{q_{n2} + q_{n1}}{2}\right)^2 + c^2}, \tag{2.64}$$

where $s_- < 0$ and $s_+ > 0$ are the left and right shock speed respectively. Notice that Rankine-Hugoniot conditions can be applied only because the problem (2.52) is written in the conservative form.

2.5.3 Star region solution

The Riemann solution in the star region can be obtained as a function of the initial datum $\mathbf{w}_0$ exploiting Riemann invariants and Rankine-Hugoniot conditions across rarefaction (superscript R) and shock (superscript S) waves respectively.

- If the left wave is a rarefaction then Γ_3 and $\Gamma_{2,3}$ Riemann invariants are preserved

$$\begin{aligned} \Gamma_{3\star} &= \Gamma_{3L} \\ \Gamma_{2,3\star} &= \Gamma_{2,3L}, \end{aligned} \tag{2.65}$$

that means

$$\begin{aligned} p_\star &= p_L + f_L^R(q_{n\star}, q_{nL}) \\ \theta_{\star L} &= \theta_L \, f_{\theta L}^R(q_{n\star}, q_{nL}), \end{aligned} \tag{2.66}$$

with

$$\begin{aligned} f_L^R(q_{n\star}, q_{nL}) \stackrel{\text{def}}{=} \frac{1}{2}\widehat{\rho}\big[&q_{nL}\left(q_{nL}+a_L\right) + c^2 \ln\left(q_{nL}+a_L\right) \\ &- q_{n\star}\left(q_{n\star}+a_\star\right) - c^2 \ln\left(q_{n\star}+a_\star\right)\big] \\ f_{\theta L}^R(q_{n\star}, q_{nL}) \stackrel{\text{def}}{=} &\frac{q_{nL}+a_L}{q_{n\star}+a_\star}. \end{aligned} \tag{2.67}$$

- If the left wave is a shock then from relations (2.63) it follows that

$$\begin{aligned} p_\star &= p_L + f_L^S(q_{n\star}, q_{nL}) \\ \theta_{\star L} &= \theta_L \, f_{\theta L}^S(q_{n\star}, q_{nL}), \end{aligned} \tag{2.68}$$

with

$$\begin{aligned} f_L^S(q_{n\star}, q_{nL}) &\stackrel{\text{def}}{=} \widehat{\rho}\frac{c^2\left(q_{n\star}-q_{nL}\right)}{s_{\star L}} \\ f_{\theta L}^S(q_{n\star}, q_{nL}) &\stackrel{\text{def}}{=} \frac{q_{nL}-s_{\star L}}{q_{n\star}-s_{\star L}} \end{aligned} \tag{2.69}$$

where

$$s_{\star L} = \frac{q_{n\star}+q_{nL}}{2} - \sqrt{\left(\frac{q_{n\star}+q_{nL}}{2}\right)^2 + c^2}. \tag{2.70}$$

- If the right wave is a rarefaction then Γ_1 and $\Gamma_{2,1}$ Riemann invariants are conserved

$$\begin{aligned} \Gamma_{1R} &= \Gamma_{1\star} \\ \Gamma_{2,1R} &= \Gamma_{2,1\star}, \end{aligned} \tag{2.71}$$

that is

$$\begin{aligned} p_\star &= p_R + f_R^R(q_{nR}, q_{n\star}) \\ \theta_{\star R} &= \theta_R \, f_{\theta R}^R(q_{nR}, q_{n\star}), \end{aligned} \tag{2.72}$$

with

$$\begin{aligned} f_R^R(q_{nR}, q_{n\star}) &\stackrel{\text{def}}{=} \frac{1}{2}\widehat{\rho}\left[q_{nR}\left(q_{nR} - a_R\right) - c^2 \ln\left(q_{nR} + a_R\right)\right. \\ &\qquad \left. - q_{n\star}\left(q_{n\star} - a_\star\right) + c^2 \ln\left(q_{n\star} + a_\star\right)\right] \\ f_{\theta R}^R(q_{nR}, q_{n\star}) &\stackrel{\text{def}}{=} \frac{q_{n\star} + a_\star}{q_{nR} + a_R}. \end{aligned} \tag{2.73}$$

- If the right wave is a shock then relations (2.63) can be applied to get

$$\begin{aligned} p_\star &= p_R + f_R^S(q_{nR}, q_{n\star}) \\ \theta_{\star R} &= \theta_R \, f_{\theta R}^S(q_{nR}, q_{n\star}), \end{aligned} \tag{2.74}$$

with

$$\begin{aligned} f_R^S(q_{nR}, q_{n\star}) &\stackrel{\text{def}}{=} \widehat{\rho}\frac{c^2\left(q_{n\star} - q_{nR}\right)}{s_{R\star}} \\ f_{\theta R}^S(q_{nR}, q_{n\star}) &\stackrel{\text{def}}{=} \frac{q_{nR} - s_{R\star}}{q_{n\star} - s_{R\star}} \end{aligned} \tag{2.75}$$

where

$$s_{R\star} = \frac{q_{nR} + q_{n\star}}{2} + \sqrt{\left(\frac{q_{nR} + q_{n\star}}{2}\right)^2 + c^2}. \tag{2.76}$$

Comparing Eqs. (2.66), (2.68), (2.72) and (2.74), it is an easy matter to derive the following equation

$$F(q_{n\star}) = p_R - p_L + f_R(q_{nR}, q_{n\star}) - f_L(q_{n\star}, q_{nL}) = 0, \tag{2.77}$$

where $f_R(q_{nR}, q_{n\star})$ and $f_L(q_{n\star}, q_{nL})$ must be set according to the nature of centered waves. In particular

$$\begin{aligned} f_R(q_{nR}, q_{n\star}) &= \begin{cases} f_R^S(q_{nR}, q_{n\star}) & q_{nR} < q_{n\star} \\ f_R^R(q_{nR}, q_{n\star}) & \text{otherwise}, \end{cases} \\ f_L(q_{n\star}, q_{nL}) &= \begin{cases} f_L^S(q_{n\star}, q_{nL}) & q_{n\star} < q_{nL} \\ f_L^R(q_{n\star}, q_{nL}) & \text{otherwise}, \end{cases} \end{aligned} \tag{2.78}$$

where the $q_{nR} < q_{n\star}$ and $q_{n\star} < q_{nL}$ inequalities satisfy the entropy condition for the right and left shock respectively, *i.e.* shocks are always compressive (see first relation of (2.63)).

The solution of the nonlinear Eq. (2.77) gives the normal component of the velocity $q_{n\star}$ in the star region and is performed using an iterative Newton method

$$\begin{cases} q_{n\star}^{k+1} = q_{n\star}^{k} - \dfrac{F(q_{n\star}^{k})}{F'(q_{n\star}^{k})} \\ q_{n\star}^{0} = \dfrac{q_{nR} + q_{nL}}{2}. \end{cases} \tag{2.79}$$

At each iteration k the function F must follow the correct wave pattern defined by Eq. (2.78). Typically, a relative convergence tolerance of 10^{-14} is achieved in 4 or 5 iterations. For the sake of completeness, derivative functions with respect to $q_{n\star}$ are reported

$$\begin{aligned} f_L^{'R}(q_{n\star}) &= -\widehat{\rho}\,(q_{n\star} + a_\star) \\ f_L^{'S}(q_{n\star}, q_{nL}) &= \frac{2\widehat{\rho}c^2\,(q_{n\star} - s_{\star L})}{s_{\star L}\,(q_{n\star} + q_{nL} - 2s_{\star L})} \\ f_R^{'R}(q_{n\star}) &= -\widehat{\rho}\,(q_{n\star} - a_\star) \\ f_R^{'S}(q_{nR}, q_{n\star}) &= \frac{2\widehat{\rho}c^2\,(q_{n\star} - s_{R\star})}{s_{R\star}\,(q_{n\star} + q_{nR} - 2s_{R\star})}, \end{aligned} \tag{2.80}$$

reminding that

$$F'(q_{n\star}) = f_R^{'}(q_{n\star}) - f_L^{'}(q_{n\star}). \tag{2.81}$$

Known $q_{n\star}$ from (2.79) and basing on (2.78), the pressure $p_\star$ in the star region can be computed as

$$p_\star = p_R + f_R(q_{nR}, q_{n\star}) = p_L + f_L(q_{n\star}, q_{nL}). \tag{2.82}$$

Finally, the conserved property $\theta_\star$ on the space-time line $x/t = 0$ is obtained by means of Eqs. (2.66), (2.68), (2.72) and (2.74) and the position of the contact discontinuity, *i.e.* the sign of $q_{n\star}$

$$\theta_\star = \begin{cases} \theta_R\, f_{\theta R} & q_{n\star} < 0 \\ \theta_L\, f_{\theta L} & \text{otherwise}, \end{cases} \tag{2.83}$$

where

$$\begin{aligned} f_{\theta R}(q_{nR}, q_{n\star}) &= \begin{cases} f_{\theta R}^{S}(q_{nR}, q_{n\star}) & q_{nR} < q_{n\star} \\ f_{\theta R}^{R}(q_{nR}, q_{n\star}) & \text{otherwise}, \end{cases} \\ f_{\theta L}(q_{n\star}, q_{nL}) &= \begin{cases} f_{\theta L}^{S}(q_{n\star}, q_{nL}) & q_{n\star} < q_{nL} \\ f_{\theta L}^{R}(q_{n\star}, q_{nL}) & \text{otherwise}, \end{cases} \end{aligned} \tag{2.84}$$

in order to satisfy the entropy condition on shock waves.

The solution in the star region is so far considered as a function of a generic reference density $\widehat{\rho}$. Since no particular conditions are defined on its value, in this work we impose to be unitary in all situations ($\widehat{\rho} = 1$).

2.5.4 Wave speeds

As seen previously, the Riemann problem solution entails four states separated by two external centered waves, *i.e.* rarefaction or shock waves, and a contact discontinuity (see Fig. 2.2). Nevertheless, even if the eigenvalue λ_2 associated with the contact discontinuity verifies the condition $\lambda_1 < \lambda_2 < \lambda_3$, for the local system (2.52) it is not at all ensured that the contact discontinuity lies between centered waves.

This can be easily proved considering that the speed of the contact S^C is the normal velocity in the star region

$$S^C = q_{n\star}, \tag{2.85}$$

and the left and right speeds of rarefactions S^R and shocks S^S are

$$q_{nL} - a_L \leq S_L^R \leq q_{n\star} - a_\star, \qquad q_{n\star} + a_\star \leq S_R^R \leq q_{nR} + a_R, \tag{2.86}$$

and

$$S_L^S = s_{\star L}, \qquad S_R^S = s_{\star R}. \tag{2.87}$$

From the definition (2.56) it follows that the contact discontinuity always lies between rarefactions

$$S_L^R < S^C < S_R^R. \tag{2.88}$$

In general this is not true with shocks. Indeed, it is an easy matter to verify for the left shock that

$$S_L^S > S^C \quad \Longleftrightarrow \quad \begin{cases} q_{nL} > 0 \\ q_{n\star} < -\dfrac{c^2}{q_{nL}}, \end{cases} \tag{2.89}$$

and for the right shock that

$$S_R^S < S^C \quad \Longleftrightarrow \quad \begin{cases} q_{nR} < 0 \\ q_{n\star} > -\dfrac{c^2}{q_{nR}}, \end{cases} \tag{2.90}$$

or in other words find a critical condition for which the contact discontinuity is faster than the shock. Notice furthermore that this behaviour is independent of the density and thus can be found also in the original Riemann solver of [6,31], even for constant density flows.

Since these conditions are more difficult to obtain for $c \to \infty$, it seems that such behaviour derives from the introduction of the artificial compressibility term inside the system (2.51) in order to restore the hyperbolic nature of equations allowing to locally couple pressure and velocity. However, our experience suggests that the effects of critical conditions (2.89) and (2.90) are negligible even for small values of the compressibility coefficient, *i.e.* $c \in [0.01, 100]$, as shown in several numerical experiments [6, 24].

2.6 Time integration

Numerical integration of Eqs. (2.12) and (2.13) by means of suitable Gauss quadrature rules leads to a system of nonlinear ODEs, or DAEs for incompressible flows, that can be written as

$$\mathbf{M_P}\left(\mathbf{W}\right)\frac{d\mathbf{W}}{dt} + \mathbf{R}\left(\mathbf{W}\right) = \mathbf{0}, \tag{2.91}$$

where $\mathbf{R}\left(\mathbf{W}\right)$ is the vector of residuals and $\mathbf{M_P}\left(\mathbf{W}\right)$ is the global block diagonal matrix arising from the discretization of the first term in Eq. (2.12). Thanks to the use of orthonormal basis functions defined in the physical space, with the set of conservative variables $\mathbf{w} = \mathbf{u}$ the matrix $\mathbf{M_P}$ reduces to the identity matrix for compressible flows and to a modified identity matrix with zeros in the diagonal positions corresponding to the pressure degrees of freedom for the incompressible flows. However, for a set of working variables that differs from the conservative one, the transformation matrix $\mathbf{P}$ couples the degrees of freedom of variables $\mathbf{w}_h$ within each block of $\mathbf{M_P}$ hence making the global mass matrix dependent from the solution and no longer diagonal at the element level.

In this work we advance in time the DG discretized equations (2.91) by using high-order implicit time integration schemes. Before analysing in detail the formulation of each scheme we want to point out the effects resulting from the use of a solution dependent block diagonal matrix $\mathbf{M_P}(\mathbf{W})$. For this purpose we apply the well known non-linear backward Euler (BE) implicit scheme to advance in time the global system (2.91)

$$\mathbf{W}^{n+1} = \mathbf{W}^{n} - \Delta t^{n}\left(\mathbf{M_P^{-1}R}\right)^{n+1}, \tag{2.92}$$

where $\Delta t^n = t^{n+1} - t^n$ is the step-size, $\mathbf{W}^n \approx \mathbf{W}(t^n)$ is the numerical approximation of the exact solution at time t^n and $\mathbf{W}^0 = \mathbf{W}(t^0)$ is the initial condition. The dependence on $\mathbf{W}$ is omitted for notational convenience.

By solving the non-linear system (2.92) through the iterative Newton-Krylov method we get for each k-*th* iteration the linear system

$$\left(\frac{\mathbf{I}}{\Delta t^n} + \mathbf{M_P^{-1}J_P}\right)_k \left(\mathbf{W}_{k+1} - \mathbf{W}_k\right) = -\frac{\mathbf{W}_k - \mathbf{W}^n}{\Delta t^n} - \left(\mathbf{M_P^{-1}R}\right)_k. \tag{2.93}$$

where the Jacobian matrix $\mathbf{J_P}$, which is computed analytically, must take into account of the solution dependent matrix $\mathbf{M_P}$

$$\mathbf{J_P} = \mathbf{J} - \frac{\partial \mathbf{M_P}}{\partial \mathbf{W}} \mathbf{M_P^{-1}} \mathbf{R}, \tag{2.94}$$

with

$$\begin{aligned} \mathbf{J} &= \frac{\partial \mathbf{R}}{\partial \mathbf{W}}, \\ \frac{\partial \mathbf{M_P^{-1}}}{\partial \mathbf{W}} &= -\mathbf{M_P^{-1}} \frac{\partial \mathbf{M_P}}{\partial \mathbf{W}} \mathbf{M_P^{-1}}. \end{aligned} \tag{2.95}$$

Notice that the linear system (2.93) can not be solved for CDI and VDI flows since the global mass matrix is singular. In order to avoid matrix inversions ($\mathbf{M_P^{-1}}$) we multiply the linear system (2.93) by the global mass matrix and get

$$\left(\frac{\mathbf{M_P}}{\Delta t^n} + \mathbf{J_P} \right)_k (\mathbf{W}_{k+1} - \mathbf{W}_k) = -\frac{\mathbf{M_P}_k}{\Delta t^n} (\mathbf{W}_k - \mathbf{W}^n) - \mathbf{R}_k. \tag{2.96}$$

where we clearly considered

$$\mathbf{M_P}_k \mathbf{M_P^{-1}}_k = \mathbf{I}. \tag{2.97}$$

despite the matrix singularity.

More in general, for CDI and VDI flows we can prove that the product between the solution dependent global mass matrix and its inverse, also computed at different instants t^n and $t^{n'}$, gives always real values. Indeed, remembering that $\mathbf{M_P}$ arises from the discretization of the first term in Eq. (2.12), it must be verified at each Gauss point that

$$\mathbf{DP}(\mathbf{w}^n) \left[\mathbf{DP}(\mathbf{w}^{n'}) \right]^{-1} \in \mathbb{R}^{m \times m}. \tag{2.98}$$

By writing the singular matrix $\mathbf{D} = \mathbf{I} - \mathbf{J}^{11}$ and its inverse as

$$\mathbf{D} = \lim_{c \to \infty} \begin{bmatrix} \frac{1}{c} & 0 & 0 & 0 & 0 \\ 0 & 1 & 0 & 0 & 0 \\ 0 & 0 & 1 & 0 & 0 \\ 0 & 0 & 0 & 1 & 0 \\ 0 & 0 & 0 & 0 & 1 \end{bmatrix}, \qquad \mathbf{D}^{-1} = \lim_{c \to \infty} \begin{bmatrix} c & 0 & 0 & 0 & 0 \\ 0 & 1 & 0 & 0 & 0 \\ 0 & 0 & 1 & 0 & 0 \\ 0 & 0 & 0 & 1 & 0 \\ 0 & 0 & 0 & 0 & 1 \end{bmatrix}, \tag{2.99}$$

and applying the limit only after matrix products, for CDI flows we obtain

$$\mathbf{DP}(\mathbf{w}^n) \left[\mathbf{DP}(\mathbf{w}^{n'}) \right]^{-1} = \mathbf{I}, \tag{2.100}$$

since $\mathbf{P} = \mathbf{I}$, and for VDI flows

$$\mathbf{DP}(\mathbf{w}^n)\left[\mathbf{DP}(\mathbf{w}^{n'})\right]^{-1} = \begin{bmatrix} 1 & 0 & 0 & 0 & 0 \\ 0 & \frac{\rho^n}{\rho^{n'}} & 0 & 0 & \frac{(\rho_{\tilde{\rho}})^n u_1^n}{(\rho_{\tilde{\rho}})^{n'}} - \frac{\rho^n u_1^{n'}}{\rho^{n'}} \\ 0 & 0 & \frac{\rho^n}{\rho^{n'}} & 0 & \frac{(\rho_{\tilde{\rho}})^n u_2^n}{(\rho_{\tilde{\rho}})^{n'}} - \frac{\rho^n u_2^{n'}}{\rho^{n'}} \\ 0 & 0 & 0 & \frac{\rho^n}{\rho^{n'}} & \frac{(\rho_{\tilde{\rho}})^n u_3^n}{(\rho_{\tilde{\rho}})^{n'}} - \frac{\rho^n u_3^{n'}}{\rho^{n'}} \\ 0 & 0 & 0 & 0 & \frac{(\rho_{\tilde{\rho}})^n}{(\rho_{\tilde{\rho}})^{n'}} \end{bmatrix}, \quad (2.101)$$

where $\mathbf{P}$ is defined by (2.33) (notice that if $t^n = t^{n'}$ than (2.101) becomes the identity matrix). Moreover, by applying the limit in (2.99) only after matrix products, it can be proved also that the additional term $(\partial \mathbf{M_P}/\partial \mathbf{W})\mathbf{M_P}^{-1}\mathbf{R}$ inside the Jacobian matrix always assumes real values.

High order implicit time integration schemes used in this work are the non-linear Explicit Singly Diagonally Implicit Runge-Kutta (ESDIRK) schemes [43] up to order five, the linearly implicit Rosenbrock-type Runge-Kutta (Rosenbrock) schemes [37] up to order five, and the linearly implicit two-step peer (Peer) methods [54] up to order six. One of the advantages in using these temporal schemes is that they can be designed to preserve their accuracy also with DAEs, *i.e.* incompressible flows. Moreover, Peer schemes proved to be able to avoid order reduction typical of one step methods when dealing with very stiff problems or problems with time-dependent boundary conditions as shown by Podhaisky *et al.* [54].

Since all considered schemes are implicit they entail the solution of several systems of non-linear or linear equations. Non-linear systems are solved using Newton-Krylov method and linear systems using Generalized Minimal Residual (GMRES) method. The GMRES method is here applied by means the algorithm available inside PETSc library [2] with a preconditioning of the iterative solver based on the block Jacobi method with one block per process, each of which is solved with ILU(0), or on the Additive Schwarz Method (ASM). We pointed out that thanks to the peculiar treatment of incompressible convective numerical fluxes (see [6] and Sec. 2.5) the Jacobian matrix has non null pressure degrees of freedom so that the global matrix arising from the implicit time discretization is non singular and the system (2.96) can be solved with standard algorithms also for CDI and VDI flows.

2.6.1 Explicit Singly Diagonally Implicit Runge-Kutta schemes

ESDIRK schemes are a class of one-step multi-stage implicit Runge-Kutta schemes that can be constructed to be $A-$ and $L-$stable for any temporal order of accuracy. Starting from a given initial solution $\mathbf{W}^0 = \mathbf{W}(t^0)$ and

omitting the dependence on $\mathbf{W}$ for notational convenience, an $s-$stages ESDIRK scheme applied to the system (2.91) is written as

$$\mathbf{W}^{n+1} = \mathbf{W}^n - \Delta t^n \sum_{i=1}^{s} b_i \left(\mathbf{M}_\mathbf{P}^{-1}\mathbf{R}\right)^i, \tag{2.102}$$

where each stage $i = 1, \ldots, s$ requires the solution of the non-linear system

$$\mathbf{W}^i = \mathbf{W}^n - \Delta t^n \sum_{j=1}^{i} a_{ij} \left(\mathbf{M}_\mathbf{P}^{-1}\mathbf{R}\right)^j, \tag{2.103}$$

with $\mathbf{W}^i \approx \mathbf{W}(t^n + c_i\Delta t^n)$ the stage solution. The non-linear system (2.103) can be solved by means of an iterative Newton-Krylov method whose k-th non-linear iteration entails the solution of the linear system

$$\begin{aligned}\left(\frac{\mathbf{M}_\mathbf{P}}{a_{ii}\Delta t^n} + \mathbf{J}_\mathbf{P}\right)_k^i \left(\mathbf{W}_{k+1}^i - \mathbf{W}_k^i\right) = &-\frac{\mathbf{M}_\mathbf{P}{}_k^i}{a_{ii}\Delta t^n}\left(\mathbf{W}_k^i - \mathbf{W}^n\right) \\ &- \sum_{j=1}^{i-1} \frac{a_{ij}}{a_{ii}} \mathbf{M}_\mathbf{P}{}_k^i \left(\mathbf{M}_\mathbf{P}^{-1}\mathbf{R}\right)^j - \mathbf{R}_k^i, \qquad k \geq 0,\end{aligned} \tag{2.104}$$

where $\mathbf{W}_0^i$ is a suitable initial guess for the Newton-Krylov method at the i-th ESDIRK stage. After solving at each stage the non-linear system (2.103) we can simply invert the relation in order to get

$$\left(\mathbf{M}_\mathbf{P}^{-1}\mathbf{R}\right)^i = \frac{\mathbf{W}^i - \mathbf{W}^n}{a_{ii}\Delta t^n} + \sum_{j=1}^{i-1} \frac{a_{ij}}{a_{ii}} \left(\mathbf{M}_\mathbf{P}^{-1}\mathbf{R}\right)^j, \quad i = 1, \ldots, s, \tag{2.105}$$

thus avoiding a costly evaluation of the right hand side.

For ESDIRK schemes the embedded solution is defined as

$$\hat{\mathbf{W}}^{n+1} = \mathbf{W}^n - \Delta t^n \sum_{i=1}^{s} \hat{b}_i \left(\mathbf{M}_\mathbf{P}^{-1}\mathbf{R}\right)^i. \tag{2.106}$$

Nevertheless, when dealing with incompressible flows no product $\mathbf{M}_\mathbf{P}\mathbf{M}_\mathbf{P}^{-1}$ can be recovered in this definition in order to avoid mass matrix inversion and thus it is impossible to compute the embedded solution for pressure field. In order to overcome this issue for such flows we simply impose the embedded solution of the pressure field equal to the embedded solution for the velocity component u_1 field.

Real coefficients a_{ij}, b_i, $\hat{b}_i$ and c_i, with $i, j = 1, \ldots, s$, uniquely define an $s-$stages ESDIRK scheme and all its stability and accuracy properties. These

coefficients have in general the following features

$$\begin{cases} a_{ii} = 0 & i = 0 \\ a_{ii} = const. & i \geq 1 \\ b_i = a_{si} & \forall i \\ c_i = \sum_{j=1}^{i} a_{ij} & \forall i. \end{cases} \tag{2.107}$$

It is an easy matter to see that the first stage is explicit and thus an $s-$stages ESDIRK scheme requires the solution of only $s-1$ non-linear systems (2.103). Moreover, the solution of the last stage is the step solution $\mathbf{W}^s = \mathbf{W}^{n+1}$.

In this work we consider the third order of accuracy - four stages (ESDIRK34), the fourth order - six stages (ESDIRK46) and the fifth order - eight stages (ESDIRK58) ESDIRK schemes designed by Kennedy and Carpenter in [43].

2.6.2 Linearly implicit Rosenbrock-type Runge-Kutta schemes

The time integration of Eq. (2.91) by means of one-step multi-stage Rosenbrock schemes, omitting the dependence on $\mathbf{W}$, can be written as

$$\mathbf{W}^{n+1} = \mathbf{W}^n + \sum_{i=1}^{s} b_i \mathbf{K}^i, \tag{2.108}$$

with $\mathbf{W}^0 = \mathbf{W}(t^0)$ as initial solution. The vector $\mathbf{K}^i = -\Delta t^n \left(\mathbf{M}_\mathbf{P}^{-1}\mathbf{R}\right)^i = -\Delta t^n \widetilde{\mathbf{R}}(\mathbf{W}^i)$ is computed at each stage $i = 1, \ldots, s$ by solving the linear system

$$\mathbf{K}^i = -\Delta t^n \widetilde{\mathbf{R}} \left(\mathbf{W}^n + \sum_{j=1}^{i-1} \alpha_{ij} \mathbf{K}^j \right) - \left(\Delta t \mathbf{M}_\mathbf{P}^{-1} \mathbf{J}_\mathbf{P}\right)^n \sum_{j=1}^{i} \gamma_{ij} \mathbf{K}^j, \tag{2.109}$$

where the Jacobian matrix is computed only once per step on the solution $\mathbf{W}^n$. The embedded solution is defined as

$$\hat{\mathbf{W}}^{n+1} = \mathbf{W}^n + \sum_{i=1}^{s} \hat{b}_i \mathbf{K}^i. \tag{2.110}$$

This Rosenbrock formulation entails the cumbersome matrix-vector product $\mathbf{J}_\mathbf{P}^\mathbf{n} \sum_{j=1}^{i-1} \gamma_{ij} \mathbf{K}^j$. In practice this can be avoided by means of the following transformation [37]

$$\sum_{j=1}^{i} \gamma_{ij} \mathbf{K}^j = \mathbf{Y}^i, \quad i = 1, \ldots, s, \tag{2.111}$$

and thus

$$\mathbf{K}^i = \frac{1}{\gamma_{ii}}\mathbf{Y}^i - \sum_{j=1}^{i-1} c_{ij}\mathbf{Y}^j, \quad i = 1, \ldots, s, \tag{2.112}$$

for which Eqs. (2.108) and (2.109) can be reduced to the equivalent formulation

$$\begin{aligned} \mathbf{W}^{n+1} &= \mathbf{W}^n + \sum_{j=1}^{s} m_j \mathbf{Y}^j, \\ \left(\frac{\mathbf{M_P}}{\gamma_{ii}\Delta t} + \mathbf{J_P}\right)^n \mathbf{Y}^i &= -\mathbf{M}_\mathbf{P}^n \left[\widetilde{\mathbf{R}}\left(\mathbf{W}^n + \sum_{j=1}^{i-1} a_{ij}\mathbf{Y}^j\right) + \sum_{j=1}^{i-1} \frac{c_{ij}}{\Delta t^n}\mathbf{Y}^j\right], \end{aligned} \tag{2.113}$$

with the embedded solution

$$\hat{\mathbf{W}}^{n+1} = \mathbf{W}^n + \sum_{i=1}^{s} \hat{m}_i \mathbf{Y}^i. \tag{2.114}$$

Real coefficients α_{ij}, γ_{ij}, b_i, $\hat{b}_i$, a_{ij}, c_{ij}, m_i and $\hat{m}_i$ of the two formulations uniquely define the Rosenbrock scheme and are related by the equations

$$\begin{aligned} (c_{ij}) &= diag(\gamma_{11}^{-1}, \ldots, \gamma_{ss}^{-1}) - \mathbf{\Gamma}^{-1}, \\ (a_{ij}) &= (\alpha_{ij})\,\mathbf{\Gamma}^{-1}, \\ (m_1, \ldots, m_s) &= (b_1, \ldots, b_s)\,\mathbf{\Gamma}^{-1}, \\ (\hat{m}_1, \ldots, \hat{m}_s) &= \left(\hat{b}_1, \ldots, \hat{b}_s\right)\mathbf{\Gamma}^{-1}, \end{aligned} \tag{2.115}$$

where $\mathbf{\Gamma} \overset{\text{def}}{=} (\gamma_{ij})$ and $\gamma_{ii} = \gamma \neq 0$.

Rosenbrock schemes considered in this work are the second order - two stages IB scheme of Iannelli and Baker [41], the third order - four stages ROS3PL of Lang and Teleaga [46], the fourth order - six stages RODASP of Steinebach [60] and the fifth order - eight stages Rod5_1 of Di Marzo [25]. All schemes are designed to be A-stable and preserve their accuracy with DAEs.

2.6.3 Linearly implicit two-step Peer methods

Peer methods are multi-stage implicit temporal schemes with two steps that compute solution approximations $\mathbf{W}^{i,n} \approx \mathbf{W}(t^n + c_i\Delta t^n)$, with $i = 1, \ldots, s$, of the Eq. (2.91) by means of s linear systems

$$\left(\frac{\mathbf{M}_\mathbf{P}^{s,n-1}}{\gamma\Delta t^n} + \mathbf{J}_\mathbf{P}^{s,n-1}\right)\left(\mathbf{W}^{i,n} - \mathbf{W}_0^i\right) = -\mathbf{M}_\mathbf{P}^{s,n-1}\left(\widetilde{\mathbf{R}}_0^{i,n} + \frac{\mathbf{Y}^i - \mathbf{W}_0^i}{\gamma\Delta t^n}\right) \tag{2.116}$$

Table 2.1: *List of γ values and corresponding θ angles of $A(\theta)$-stability and $L(\theta)$-stability for each Peer method used in this work*

	s	γ	θ
peer3A	3	$2.165162598341552E+00$	$90°$
peer4A	4	$1.038881828680110E+00$	$90°$
peer5A	5	$5.614731292097847E-01$	$90°$
peer6A	6	$3.476356828221134E-01$	$90°$

with

$$\mathbf{Y}^i = \sum_{j=1}^{i-1} \frac{a_{ij}}{\gamma} \left(\mathbf{W}^{j,n} - \mathbf{Y}^j \right) + \sum_{j=1}^{s} u_{ij}(\sigma^n) \mathbf{W}^{j,n-1}, \tag{2.117}$$

$$\mathbf{W}_0^i = \sum_{j=1}^{i-1} \frac{a_{0ij}}{\gamma} \left(\mathbf{W}^{j,n} - \mathbf{Y}^j \right) + \sum_{j=1}^{s} u_{0ij}(\sigma^n) \mathbf{W}^{j,n-1}, \tag{2.118}$$

where s is the number of stages and the Jacobian matrix of the DG space discretization $\mathbf{J}_{\mathbf{P}}^{s,n-1}$ is computed only once per step with the last stage solution of the previous step $\mathbf{W}^{s,n-1}$. At each step, the embedded solution is given by

$$\hat{\mathbf{W}}^{s,n} = \sum_{i=1}^{s-1} \alpha_i \mathbf{W}^{i,n}. \tag{2.119}$$

Notice that like any other multi-step scheme Peer methods are non-self-starting. Indeed, in order to compute step $n = 1$ of the formulation (2.116), starting solutions $\mathbf{W}^{i,0}$, with $i = 1, \ldots, s$, at times $t^{i,0} = t^{st} + c_i \Delta t^{st}$ must be available, where superscript st denotes the starting step. The algorithm proposed in this work to compute $\mathbf{W}^{i,0}$ will be described in detail in Sec. 3.6.

$\mathbf{A} = \{a_{ij}\}$, $\mathbf{U} = \{u_{ij}\}$, $\mathbf{A}_0 = \{a_{0ij}\}$ and $\mathbf{U}_0 = \{u_{0ij}\}$ are $s \times s$ matrices of real coefficients and α_i, c_i and γ are real parameters. Matrices $\mathbf{U}$ and $\mathbf{U}_0$ depend on the step size ratio $\sigma^n = \Delta t^n / \Delta t^{n-1}$ between the current and the previous step in order to ensure accuracy and stability properties for variable step sizes. More in general, matrices $\mathbf{A}$, $\mathbf{U}$, $\mathbf{A}_0$ and $\mathbf{U}_0$ and parameters γ and c_i uniquely define accuracy and stability properties of an s-stages Peer method. Consistency and zero stability conditions that ensure an order of accuracy equal to $s - 1$ for all Peer stages and for all step size ratios $\sigma > 0$ are provided in [34, 54]. These conditions are derived independently from the Jacobian matrix which thus can be computed numerically, *e.g.* by means of finite differences. Since all stage solutions have the same accuracy and stability properties a continuous output of high-order is available with no extra-cost.

As proposed by Podhaisky *et al.* [54], matrices $\mathbf{A}$, $\mathbf{U}$, $\mathbf{A}_0$ and $\mathbf{U}_0$ are functions of parameters c_i and γ, where coefficients c_i are chosen to be stretched

Chebychev nodes in the interval $[-1, 1]$:

$$c_i = -\frac{\cos\left(\left(i - \frac{1}{2}\right)\frac{\pi}{s}\right)}{\cos\left(\frac{\pi}{2s}\right)}, \qquad i = 1, \ldots, s. \tag{2.120}$$

Following this choice it is clear that $c_s = 1$ and thus

$$\mathbf{W}^{n+1} = \mathbf{W}^{s,n} \qquad \text{and} \qquad \hat{\mathbf{W}}^{n+1} = \hat{\mathbf{W}}^{s,n}. \tag{2.121}$$

The last free parameter γ specifies the θ angle of the $A(\theta)$- and $L(\theta)$-stability. Moreover, as demonstrated in [54] only for constant time-steps, particular values of γ can guarantee an additional order of accuracy which thus becomes equal to the number of stages s. Finally, coefficients α_i, $i = 1, \ldots, s-1$, are only function of nodes c_i and are computed such that the order of accuracy of the embedded solution is equal to $s - 2$ (see [34]).

Peer methods used in this work have three, four, five and six stages and are referred as peer3A, peer4A, peer5A and peer6A, where the capital "A" points out the fact that they are derived in order to be A-stable and L-stable, *i.e.* $\theta = 90°$. Parameter γ values adopted for each scheme are reported in Tab. 2.1. For these values, Peer methods show an order of accuracy equal to s for constant time-steps.

CHAPTER 3

Robustness and efficiency enhancement of high order linear/non-linear implicit time integration schemes

ESDIRK, Rosenbrock and Peer time integration schemes are implicit schemes and therefore entail the solution of several systems of linear/non-linear equations that represent one of the main sources of computational cost. In order to reduce this cost, an efficiency enhancement of iterative methods that compute system solutions is required. Nevertheless, despite any advantage in terms of efficiency it must be clear that the time integration robustness remains of utmost importance.

In this chapter we firstly show how to improve the time integration robustness by means of the adaptive time step approach. Successively, we describe strategies for both the initial guess setting and the stopping criteria definition that we apply to iterative methods. Moreover, we provide some useful tricks adopted in this work for the efficiency enhancement of the non-linear Newton-Krylov method. Finally, a new starting procedure able to preserve the accuracy of Peer methods is derived. The norm symbol $\|\cdot\|$ used in this chapter is always referred to the euclidean norm although a generic user-defined norm can be used without any restriction.

The authors would like to underline that all the reported strategies can be used independently on the nature of the ODE/DAE systems on which the time

Table 3.1: *List of global, local and estimator constants and orders of ESDIRK, Rosenbrock and Peer schemes obtained for the model ODE. The global error is computed at the final step while the LTE and the local estimator are computed after the first step.*

	ψ_g^N	ψ_l^1	ψ_r^1	q_g	q_l	q_r
BE	$2.71\text{E}-01$	$2.00\text{E}+00$	$2.71\text{E}-01$	1	2	1
CN	$9.02\text{E}-02$	$6.67\text{E}-01$	$2.71\text{E}-01$	2	3	2
ESDIRK34	$5.61\text{E}-02$	$4.14\text{E}-01$	$2.56\text{E}-03$	3	4	3
ESDIRK46	$3.67\text{E}-03$	$2.70\text{E}-02$	$4.84\text{E}-04$	4	5	4
ESDIRK58	$9.92\text{E}-04$	$7.24\text{E}-03$	$1.15\text{E}-04$	5	6	6
LBE	$2.71\text{E}-01$	$2.00\text{E}+00$	$2.71\text{E}-01$	1	2	1
IB	$4.38\text{E}-02$	$3.24\text{E}-01$	$1.12\text{E}-01$	2	3	2
ROS3PL	$5.61\text{E}-02$	$4.14\text{E}-01$	$2.24\text{E}-02$	3	4	3
RODASP	$3.77\text{E}-03$	$2.78\text{E}-02$	$8.45\text{E}-03$	4	5	4
Rod5_1	$4.42\text{E}-04$	$3.23\text{E}-03$	$2.46\text{E}-03$	5	6	5
peer3A	$1.45\text{E}+01$	$2.51\text{E}+01$	$5.41\text{E}-01$	3	3	2
peer4A	$3.42\text{E}+00$	$1.33\text{E}+01$	$2.99\text{E}-01$	4	4	3
peer5A	$8.21\text{E}-01$	$5.64\text{E}+00$	$1.12\text{E}-01$	5	5	4
peer6A	$1.93\text{E}-01$	$2.05\text{E}+00$	$3.12\text{E}-02$	6	6	5

integration is applied.

3.1 Asymptotic model

As first step we introduce three quantities that will be used in next sections.

- The *global error* at time t^{n+1} represents the numerical error of the time integration and is defined as the difference between the exact and the numerical solution

$$err^{n+1} = \mathbf{W}(t^{n+1}) - \mathbf{W}^{n+1}. \tag{3.1}$$

- The *Local Truncation Error* (LTE) is the numerical error introduced by the temporal scheme at the single step level and is defined as

$$LTE^{n+1} = \mathbf{W}(t^{n+1}) - \mathbf{W}_\star^{n+1}. \tag{3.2}$$

  $\mathbf{W}_\star^{n+1}$ is the solution approximation computed applying one step of the prescribed temporal scheme starting from the exact solution $\mathbf{W}(t^n)$ (or $\mathbf{W}(t^{n-1} + c_{i=1,\dots,s}\Delta t^{n-1})$ for Peer methods). Since the exact solution $\mathbf{W}(t)$ is in general not available for complex problems except for the initial condition $\mathbf{W}^0 = \mathbf{W}(t^0)$, the LTE can be computed only at the first step with the exact solution $\mathbf{W}(t^1)$ replaced by a reference numerical solution $\mathbf{W}_r^1$ more accurate than $\mathbf{W}^1 = \mathbf{W}_\star^1$

$$LTE^1 = \mathbf{W}(t^1) - \mathbf{W}_\star^1 \approx \mathbf{W}_r^1 - \mathbf{W}^1. \tag{3.3}$$

Figure 3.1: *Convergence analysis of the global error at the end time $t^N = 1$ and of the LTE after the first step for ESDIRK, Rosenbrock and Peer schemes.*

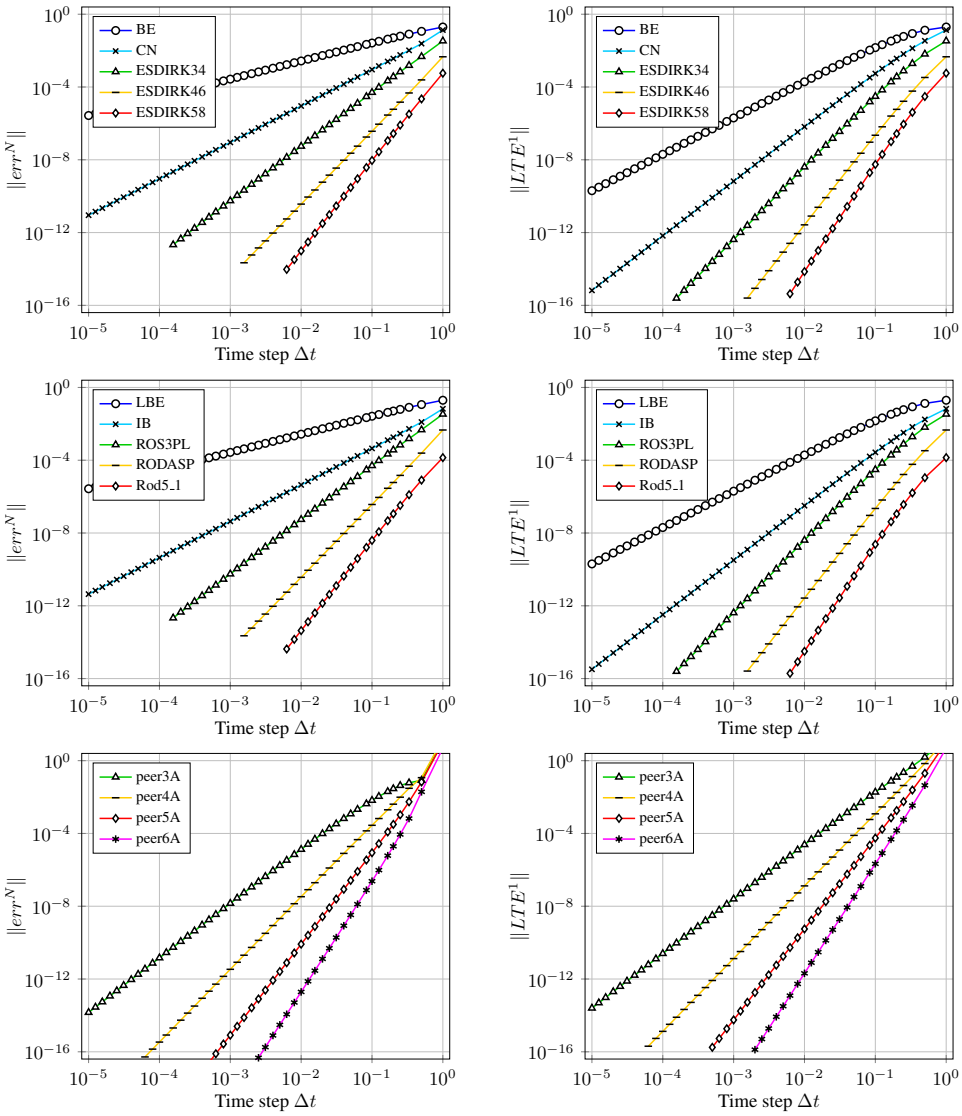

- the *local estimator* is defined by means of the temporal scheme embedded solution $\hat{\mathbf{W}}$ as

$$r^{n+1} = \|\mathbf{W}^{n+1} - \hat{\mathbf{W}}^{n+1}\|. \tag{3.4}$$

  Notice that, conversely to the LTE, the local estimator can be cheaply computed at each time step.

Each quantity above mentioned can be represented by means of the asymp-

Figure 3.2: *Convergence analysis for the local estimator after the first step of ESDIRK, Rosenbrock and Peer schemes.*

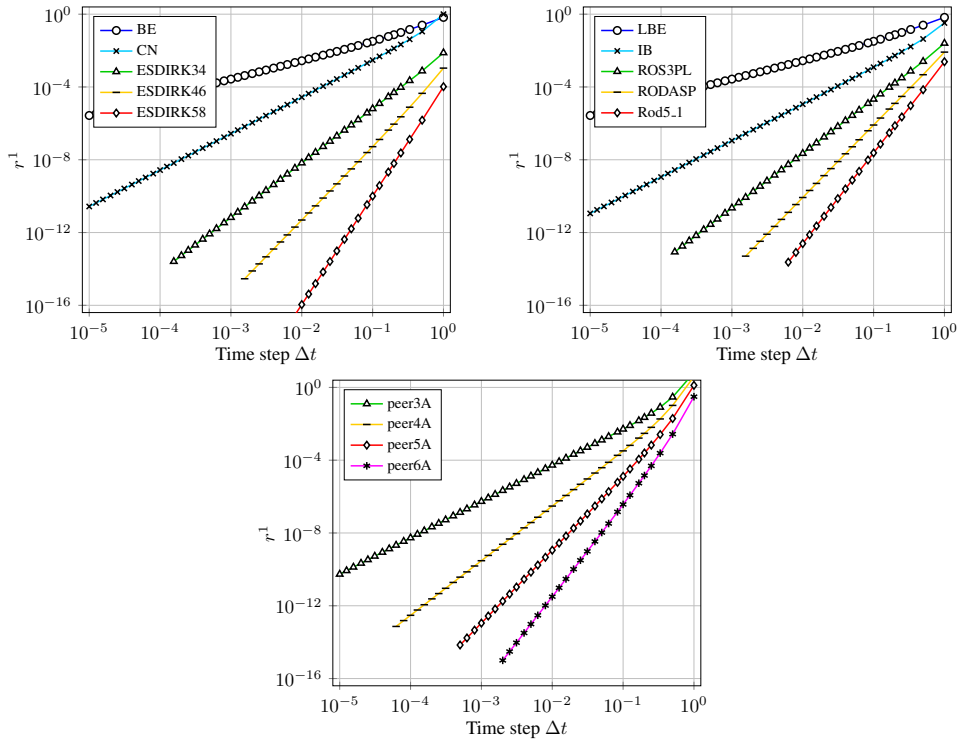

totic model

$$\|err^{n+1}\| = \psi_g^{n+1} \left(\Delta t\right)^{q_g}, \tag{3.5}$$

$$\|LTE^{n+1}\| = \psi_l^{n+1} \left(\Delta t^n\right)^{q_l}, \tag{3.6}$$

$$r^{n+1} = \psi_r^{n+1} \left(\Delta t^n\right)^{q_r}, \tag{3.7}$$

where ψ_g, ψ_l, ψ_r are the global, local, estimator constants and q_g, q_l, q_r are the global, local, estimator order of convergence. Δt is defined as the arithmetic mean of the step sizes during the time integration

$$\Delta t = \frac{1}{N} \sum_{k=1}^{N} \Delta t^{k-1}, \tag{3.8}$$

with N the number of performed steps at time t^{n+1}.

For the sake of clarity, in Fig. 3.1 and 3.2 we show as exemplary case the asymptotic behaviour of the global error, the LTE and the local estimator for ESDIRK, Rosenbrock and Peer schemes applied to the test ODE

$$\frac{\partial y(t)}{\partial t} = \lambda y(t), \tag{3.9}$$

where $\lambda = 2$, $t^N = 1$ is the end time, $y(0) = 1$ is the initial condition and $y(t) = \exp(\lambda t)$ the exact solution.

Backward Euler (BE) and Crank-Nicolson (CN) time integration schemes are here included inside the ESDIRK class since they can be considered as a particular formulation of ESDIRK schemes ($s = a_{11} = b_1 = c_1 = 1$ and $\hat{b}_1 = 0$ for BE and $s = 2$ with $a_{11} = c_1 = \hat{b}_1 = 0$, $a_{21} = a_{22} = b_1 = b_2 = 1/2$ and $c_2 = \hat{b}_2 = 1$ for CN). For the same reason the Linearised Backward Euler (LBE) scheme is included in Rosenbrock class ($s = \gamma = m_1 = 1$ and $a_{11} = c_{11} = \hat{m}_1 = 0$).

In Tab. 3.1 are reported error constants ψ and orders q computed for each scheme with the smallest time-step used. Notice that Peer methods show higher values of the constants. Moreover, temporal schemes verify in general $q_g = q_r = q_l - 1$. Exceptions are the ESDIRK58, for which $q_r = q_l$, and all Peer methods, where $q_g = q_l$ thanks to the particular choice of γ parameter that allows to obtain for constant step-sizes an order of convergence equal to the number of stages.

3.2 Adaptive time-step strategy

The automatic step-size control is an important feature to increase the efficiency and robustness of a time integration scheme. A constant time step may result in a large number of small steps, increasing computational costs of a simulation. A variable time step instead can enhance the efficiency of time integration by minimizing the computational effort to achieve a user-defined accuracy. Moreover, the time step adaptation limits at each step the local truncation error thus improving the time integration robustness.

The approach consists in adapting the step-size in order to control the local truncation error of the scheme, *i.e.* keeping it constant during the time integration. However, as shown in Sec. 3.1, when the analytic solution is unavailable the LTE can be computed only at the first step. In order to overcome this issue we impose that the LTE is a function of the local estimator (3.7) only

$$LTE^{n+1} = LTE(r^{n+1}). \tag{3.10}$$

This hypothesis allows to build the adaptive algorithm on the local estimator knowing that if we are able to maintain r as much as possible constant during the integration in time then the LTE will be constant as well.

The standard step-size algorithm [58, 59] requires at each time step that

$$r^{n+1} < \zeta_a \eta \tag{3.11}$$

where η is a properly defined threshold value and ζ_a is a user-defined safety factor, here set $\zeta_a = 2/3$. If the condition (3.11) is verified than the solution

$\mathbf{W}^{n+1}$ is accepted and the next step-size is defined requiring $r^{n+2} = \eta$ and exploiting the asymptotic behaviour (3.7)

$$\Delta t^{n+1} = \left(\frac{\eta}{\psi_r^{n+2}} \right)^{\frac{1}{q_r}}; \tag{3.12}$$

otherwise, $\mathbf{W}^{n+1}$ is rejected and the step is redone imposing

$$\Delta t^{n} = \left(\frac{\eta}{\psi_r^{n+1}} \right)^{\frac{1}{q_r}}, \tag{3.13}$$

where the constant ψ_r^{n+1} is computed by means the available local estimator at the time step rejected $\overline{\Delta t}^n$

$$\psi_r^{n+1} = \frac{r^{n+1}}{\left(\overline{\Delta t}^n\right)^{q_r}}. \tag{3.14}$$

The adaptive step-size algorithm is here applied to control the LTE of only one of the working variables $\mathbf{w}$. In particular we control the second velocity component u_2 for compressible and constant density incompressible flows and the working density $\widetilde{\rho}$ for variable density incompressible flows. Other choices can be done without any restriction. Hereinafter in this section the reference to the chosen variable is omitted for notational convenience.

3.2.1 Prediction of the estimator constant

The unknown estimator constant ψ_r^{n+2} in Eq. (3.12) must be properly predicted in order to maximise the efficiency of the adaptive algorithm, *i.e.* reduce as much as possible the number of rejected steps.

In this work we propose to extrapolate the required value from estimator constants at previous steps by means of high order Lagrangian polynomials. Therefore, considering the logarithmic transformation

$$\widetilde{\psi_r} = \ln\left(\psi_r\right), \tag{3.15}$$

we apply the approximation

$$\widetilde{\psi_r}^{n+2} \approx \widetilde{\psi_r}_z^{n+2} = \sum_{j=1}^{z} l_{zj}(t^{n+2}) \widetilde{\psi_r}^{n+2-j}, \tag{3.16}$$

where $l_{zj}(t^{n+2})$ are the Lagrange basis polynomials

$$l_{zj}(t^{n+2}) = \begin{cases} 1 & z = 1 \\ \prod_{i \neq j, i=1}^{z} \dfrac{t^{n+2} - t^{n+2-i}}{t^{n+2-j} - t^{n+2-i}} & \text{otherwise,} \end{cases} \tag{3.17}$$

thus obtaining

$$\psi_r^{n+2} = \prod_{j=1}^{z} \left(\psi_r^{n+2-j}\right)^{l_{zj}(t^{n+2})}. \tag{3.18}$$

Notice that due to the logarithmic approach the predicted estimator constant is always positive regardless of the Lagrangian basis values.

Since the time t^{n+2} needed for the definition of Lagrangian basis is unknown (see Eq. (3.12)), first we set an attempt value of t^{n+2} using Eq. (3.12)) and (3.18) with $z = 1$

$$t_\star^{n+2} = t^{n+1} + \left(\frac{\eta}{\psi_r^{n+1}}\right)^{\frac{1}{q_r}}, \tag{3.19}$$

and then we impose

$$\psi_r^{n+2} = \prod_{j=1}^{z} \left(\psi_r^{n+2-j}\right)^{l_{zj}(t_\star^{n+2})}. \tag{3.20}$$

The parameter $z \in [1, z_{max}]$, with $z_{max} = 4$ the number of stored past estimator constants, is here set at each time step in such a way to minimise the approximation error $|\widetilde{\psi_r}^{n+1} - \widetilde{\psi_{r_z}}^{n+1}|$ at the actual step.

3.2.2 Tolerance proportionality and calibration

The threshold value η used in Eq. (3.11) is defined as

$$\eta = \tau_c \tau, \qquad \tau = \max\left(\tau_r \|\mathbf{W}_{w_j}^{n+1}\|, \tau_a\right), \tag{3.21}$$

where τ_c is a scaling factor, τ_r and τ_a are the prescribed relative and absolute adaptive tolerances, respectively, and $\mathbf{W}_{w_j}^{n+1}$ are the DoFs related the the working variable w_j controlled by the adaptive algorithm.

Söderlind and Wang [59] suggest that an adaptive algorithm should work in a tolerance proportional mode. This implies that if τ_r or τ_a are changed of one order of magnitude, then also the global error should change by one order of magnitude. Moreover, it should desirable to calibrate the threshold value in such a way to obtain a global error equal to the prescribed tolerance τ. Here we achieve both goals by properly defining the scaling factor τ_s.

Thanks to the adaptive algorithm we can assume that

$$r^{n+1} \approx \eta, \qquad \forall n = 0, \ldots, N-1. \tag{3.22}$$

Basing on the asymptotic behaviours of the global error (3.5) and of the local estimator (3.7), it follows that

$$\Delta t = \left(\frac{\|err^N\|}{\psi_g^N}\right)^{\frac{1}{q_g}} = \left(\frac{\eta}{\psi_r}\right)^{\frac{1}{q_r}}, \tag{3.23}$$

with ψ_r the weighed mean value of the estimator constant during the time integration. Therefore, imposing the tolerance proportionality

$$\|err^N\| \propto \tau, \tag{3.24}$$

and, more in particular, the desired calibration

$$\|err^N\| = \tau, \tag{3.25}$$

and substituting the Eq. (3.21) inside the Eq. (3.23) we get

$$\tau_c = \tau_\psi \tau^{\frac{q_r - q_g}{q_g}}, \tag{3.26}$$

where

$$\tau_\psi = \psi_r \left(\psi_g^N\right)^{-\frac{q_r}{q_g}}. \tag{3.27}$$

The constant τ_ψ defines the calibration and can be computed noting from Eq.(3.23) that

$$\tau_\psi = const. = \eta_0 \left(err_0^N\right)^{-\frac{q_r}{q_g}} \tag{3.28}$$

with η_0 a reference threshold value used in a test simulation with the adaptive time step algorithm and err_0^N the obtained global error at output time t^N. Unfortunately, the parameter τ_ψ is strongly case dependent. Moreover, for the same case it assumes different values for different simulation end times t^N, *i.e.* different values of err_0^N. This implies that the calibration can be performed only for simple test cases thus imposing for more complex problems the simple choice $\tau_\psi = 1$.

Notice that the tolerance proportionality remains verified by Eq. (3.26) regardless of the τ_ψ value since it is constant.

3.2.3 Smooth limiter

Following the idea of Söderlind and Wang [59], in order to improve the the robustness and the efficiency of the adaptive algorithm we limit the max step-size increase/reduction by introducing the smooth limiter function

$$\Delta t^m = \Delta t^n \left[1 + \kappa \arctan\left(\frac{\Delta t^\star - \Delta t^n}{\kappa \Delta t^n}\right)\right], \tag{3.29}$$

where $\Delta t^\star$ is the step-size computed by either Eq. (3.12) or Eq. (3.13) in accordance with the condition (3.11) and the Δt^m is the new limited value of the next time step.

It is an easy matter to see that until the predicted time step variations are small ($\Delta t^\star \approx \Delta t^n$) the effects of the smooth limiter are negligible ($\Delta t^m \approx \Delta t^\star$). Conversely large variations result in a restriction on Δt^m values. More in detail, smooth limiter bounds are defined by means the user defined parameter

κ. In [59] the authors suggest to use $\kappa \in [0.7, 2]$. However in this work we set the κ value as a function of temporal scheme accuracy. Indeed, from the asymptotic behaviour of the LTE (3.6) we can derive

$$\Delta t^m = \left(\frac{\psi_l^{n+1}}{\psi_l^{m+1}} \frac{\|LTE^{m+1}\|}{\|LTE^{n+1}\|} \right)^{\frac{1}{q_l}} \Delta t^n. \tag{3.30}$$

Assuming $\psi_l^{n+1} \approx \psi_l^{m+1}$ in the first instance and writing

$$\frac{\|LTE^{m+1}\|}{\|LTE^{n+1}\|} = 10^{\lambda}, \tag{3.31}$$

then the Eq. (3.29) in the limit of $\Delta t^\star \to +\infty$ leads to the relation

$$\kappa = \frac{2}{\pi} \left(10^{\frac{\lambda}{q_l}} - 1 \right), \tag{3.32}$$

where λ represents the admitted maximum growth of the LTE during one step in terms of orders of magnitude. In this work we set $\lambda = 1$.

3.3 Initial guess for iterative methods

Implicit temporal schemes entail the solution of linear and non-linear systems of equation by means of iterative methods. Natural choices for initial guesses of such methods are

- for ESDIRK schemes (2.103)

$$\mathbf{W}_0^{i,n} = \mathbf{W}^n, \tag{3.33}$$

- for Rosenbrock schemes (2.113)

$$\mathbf{Y}_0^{i,n} = 0, \tag{3.34}$$

- for Peer schemes (2.116)

$$\mathbf{W}_0^{i,n} - \mathbf{W}_0^{i} = 0, \tag{3.35}$$

where the apex n points out the time step associated.

First attempts to provide better choices and thus to improve iterative method performances were made in the context of multi-step schemes for which a straightforward way consists in extrapolate an high-order approximation by means of the past solutions available from the temporal scheme (see [20, 21]).

Recently, Boom and Zingg in [15] applied the multi-step strategy to the one-step ESDIRK schemes using Lagrange basis polynomials with up to three past solutions as a balance between accuracy and memory usage. Moreover, Hairer

and Wanner [37] proposed to extrapolate the initial guess for ESDRIK schemes using stage solutions at the previous step. Attempts to provide a better initial guess for Rosenbrock schemes, instead, are not yet available in the literature at authors knowledge. Finally for Peer methods, relation (3.35) already represents a very efficient choice since $\mathbf{W}_0^i$ (2.118) is a high-order approximation of the solution.

In this section we improve the Hairer-Wanner interstage approach and extend the multi-step extrapolation for ESDIRK schemes. Furthermore, we show how to apply both approached to Rosenbrock schemes as well.

The Hairer-Wanner approach has the advantage of being very accurate without requiring further memory usage but it works well only for schemes with an high number of stages s. Conversely, the multi-step approach can be applied independently on s but needs to store past solutions. In order to maximise the efficiency we implement and activate both strategies. As a consequence a choice between the approaches must be done. The strategy selection, performed at each stage of each time step, is based on which approach minimizes the initial guess error of the same stage at the previous time step. Moreover, this selection is carried out at the mesh element level thus avoiding message-passing communication and minimising the computational cost especially when dealing with massively parallel simulations.

We point out that, since both approaches rely on the extrapolation from past values, for robustness purposes it would be useful to avoid their application for large step-sizes. However, our experience suggests that no issues occur in using such strategies until very large step-sizes are used (step-sizes for which the time integration accuracy, even for higher order schemes, is remarkably poor).

3.3.1 Improved Hairer-Wanner approach

The Hairer-Wanner approach extrapolate the initial guess of ESDIRK scheme stages by means of Lagrange basis polynomials from stage solutions at previous time steps $\mathbf{W}^{i,n-1}$, $i = 1, \dots, s$.

We improve this approach simply noting that at each stage i we can define the new set of data

$$\mathbf{W}^k = \begin{cases} \mathbf{W}^{k,n-1} & k \leq i \\ \mathbf{W}^{k,n} & \text{otherwise,} \end{cases} \qquad t^k = \begin{cases} t^{k,n-1} & k \leq i \\ t^{k,n} & \text{otherwise,} \end{cases} \tag{3.36}$$

that allows to use the available solutions from previous stages at the actual step which, in general, give more suitable information for the prediction of $\mathbf{W}^{i,n}$. Moreover, we sort the new set of data $\mathbf{W}^k$ as $\mathbf{W}^j$ basing on the distance with respect to the stage time $t^{i,n}$

$$|t^j - t^{i,n}| < |t^{j+1} - t^{i,n}|, \qquad \forall j = 1, \dots, s-1, \tag{3.37}$$

reminding that for ESDIRK schemes

$$t^{i,n} = t^n + c_i \Delta t^n. \tag{3.38}$$

Notice that for $j = k$ in general $\mathbf{W}^j \neq \mathbf{W}^k$ and $t^j \neq t^k$.

Therefore, the initial guess for ESDIRK schemes is set as

$$\mathbf{W}_0^{i,n} = \sum_{j=1}^{z} l_{zj}(t^{i,n}) \mathbf{W}^j, \tag{3.39}$$

where $l_{zj}(t^{i,n})$ are the Lagrange basis polynomials defined on t^j sorted nodes and $z \in [1, s]$ is set as the number of solutions $\mathbf{W}^j$ that minimises the approximation error $\|\mathbf{W}^{i,n-1} - \mathbf{W}_0^{i,n-1}\|_K$ of the stage at the past step. As pointed out, the norm is performed at the mesh element K level. As a consequence, the parameter z is also defined for each element.

For robustness purposes, when the initial guess approach is applied together with the time step adaptation, we always impose $z = 1$ for $\Delta t^{n+1} > 1.2\Delta t^n$.

3.3.2 Extended multi-step approach

The multi-step approach of Boom and Zingg defines the initial guess at the i-th ESDIRK stage as the Lagrangian extrapolation

$$\mathbf{W}_0^{i,n} = \sum_{j=1}^{z} l_{zj}(t^{i,n}) \mathbf{W}^{n+1-j}. \tag{3.40}$$

where $l_{zj}(t^{i,n})$ are the Lagrangian basis defined on nodes t^{n+1-j}.

Although this formulation provide good initial guesses, it is limited by the fact that the accuracy of the step solutions $\mathbf{W}^{n+1-j}$ used for the extrapolation is in general different with respect to the accuracy of the stage solution $\mathbf{W}^{i,n}$ (notice for example that the solution of the second ESDIRK stage always corresponds to the solution of a second order CN scheme). For this reason we perform the extrapolation on the past solutions of the same stage in which the initial guess is required

$$\mathbf{W}_0^{i,n} = \sum_{j=1}^{z} l_{zj}(t^{i,n}) \mathbf{W}^{i,n+1-j}, \tag{3.41}$$

where $l_{zj}(t^{i,n})$ are now defined on nodes $t^{i,n+1-j}$. Indeed, using Eq. (3.41) the initial guess is extrapolated from past solutions which have the same accuracy of the sought stage solution.

Once again $z \in [1, z_{max}]$ is defined for each mesh element and is set for each stage in order to minimise the approximation error $\|\mathbf{W}^{i,n-1} - \mathbf{W}_0^{i,n-1}\|_K$

at the past step. Here we impose $z_{max} = 10$. For robustness purposes we set $z = 1$ for $\Delta t^{n+1} > 1.2\Delta t^n$ when the time step adaptation is activate.

It is an easy matter to see that the formulation (3.41) requires a large memory usage since one set of past solutions must be now stored for each stage. However in our simulations this drawback is a relatively minor issue due to the fact that we need to store the analytically computed Jacobian matrix whose memory request can be much higher, especially for very high DG discretization orders.

3.3.3 Initial guess for Rosenbrock schemes

Initial guess strategies defined for ESDIRK schemes can be applied with some slight modifications to Rosenbrock schemes as well. However, the stage solution of Rosenbrock schemes $\mathbf{Y}^{i,n}$ (2.111) is a linear combination of right-hand-sides computed at different stages. Moreover it is not associated to a particular time thus making a direct extrapolation impossible.

We overcome the issue by defining the initial guess directly on the right-hand-side associated with the i$-th$ stage

$$\widetilde{\mathbf{R}}(\mathbf{W}_0^{i,n}) = \left(\mathbf{M}_{\mathbf{P}}^{-1}\mathbf{R}\right)_0^{i,n} = -\frac{\mathbf{K}_0^{i,n}}{\Delta t^n}, \tag{3.42}$$

and therefore imposing from (2.112)

$$\mathbf{Y}_0^{i,n} = -\gamma_{ii}\Delta t^n \widetilde{\mathbf{R}}(\mathbf{W}_0^{i,n}) + \sum_{j=1}^{i-1} c_{ij}\mathbf{Y}^{j,n}. \tag{3.43}$$

As a consequence, for Rosenbrock schemes the improved Hairer-Wanner approach requires that

$$\widetilde{\mathbf{R}}(\mathbf{W}_0^{i,n}) = \sum_{j=1}^{z} l_{zj}(t^{i,n})\widetilde{\mathbf{R}}(\mathbf{W}^j), \tag{3.44}$$

while the extended multi-step approach reads

$$\widetilde{\mathbf{R}}(\mathbf{W}_0^{i,n}) = \sum_{j=1}^{z} l_{zj}(t^{i,n})\widetilde{\mathbf{R}}(\mathbf{W}^{i,n+1-j}). \tag{3.45}$$

Notice that right-hand-sides at previous stages and times used for extrapolations can be cheaply computed at each previous stage inverting the relation (3.43) after the linear system solution.

In order to compute Lagrangian basis we remember that for Rosenbrock schemes

$$t^{i,n} = t^n + \beta_i \Delta t^n, \tag{3.46}$$

where

$$\beta_i = \sum_{j=1}^{s} \beta_{ij} = \sum_{j=1}^{s} (\alpha_{ij} + \gamma_{ij}) \,. \tag{3.47}$$

3.4 Termination criterion for iterative methods

When an implicit temporal scheme is applied to a system of ODEs/DAEs, a linear/non-linear system of the general form

$$\mathcal{R}(\mathbf{X}) = \mathbf{A}\mathbf{X} + \mathbf{B} = \mathbf{0}, \tag{3.48}$$

must be solved, where $\mathcal{R}$ is the residual vector, $\mathbf{X}$ the unknown solution vector and $\mathbf{A}$ and $\mathbf{B}$ are the matrix and the column vector of coefficients, respectively. Iterative methods, such as Newton-Krylov method and GMRES method, are able to compute only an approximated solution of the system (3.48) by means of an iterative process. Therefore, a stopping criterion must be used in order to achieve a properly defined accuracy τ_s hence reducing the computational cost without losing the global accuracy of the time integration.

Several authors [14, 37, 59] provided different termination criteria for both linear and non-linear iterative methods. Anyway, we can distinguish them into two classes

- the *residual criterion* class, where the iterative process is stopped at the first k$-th$ iteration for which

$$\| \mathcal{R}(\mathbf{X}_k) \| < \tau_s, \tag{3.49}$$

- and the *increment criterion* class, for which the arrest occurs when is verified that

$$\| \mathbf{X}_{k-1} - \mathbf{X}_k \| < \tau_s. \tag{3.50}$$

The residual criterion has the advantage to deal with the exact approximation error of the residual $\mathcal{R}(\mathbf{X_k})$ at the k$-th$ iteration. Indeed, the residual computed with the exact solution $\mathbf{X}^\star$ is null thus leading to

$$\| \mathcal{R}(\mathbf{X_k}) - \mathcal{R}(\mathbf{X}^\star) \| = \| \mathcal{R}(\mathbf{X_k}) \|, \qquad k \geq 0. \tag{3.51}$$

Unfortunately this criterion class does not provide any information about the approximation error of the solution $\mathbf{X_k}$ at the actual iteration.

The increment criterion, instead, gives only an estimation of approximation error of the solution at the previous iteration $k-1$ since for a convergent iterative process we can consider

$$\| \mathbf{X}_{k-1} - \mathbf{X}_k \| \approx \| \mathbf{X}_{k-1} - \mathbf{X}^\star \|, \qquad k \geq 1. \tag{3.52}$$

Moreover, this criterion can not be performed before starting the iterations ($k = 0$).

It is clear that none of the mentioned criterion is able to detect the approximation error on the system solution at the actual iteration k

$$\|\mathbf{X}_k - \mathbf{X}^\star\|, \qquad k \geq 0. \tag{3.53}$$

For this reason in this work we define a new termination criterion based on the assumption that during the convergence of a generic iterative method it is possible to consider approximately constant the ratio

$$\frac{\|\mathcal{R}(\mathbf{X}_k)\|}{\|\mathbf{X}_k - \mathbf{X}^\star\|} \approx const, \qquad k \geq 0. \tag{3.54}$$

Exploiting the relation (3.52), we can define then a scaling ratio

$$r_s = \min_{i \in [1,k]} \frac{\|\mathcal{R}(\mathbf{X}_{i-1})\|}{\|\mathbf{X}_{i-1} - \mathbf{X}_i\|}, \tag{3.55}$$

and estimate the sought solution approximation error as

$$\|\mathbf{X}_k - \mathbf{X}^\star\| \approx \frac{\|\mathcal{R}(\mathbf{X}_k)\|}{r_s}, \qquad k \geq 0, \tag{3.56}$$

where in Eq. (3.55) the minimum value is kept for safety purposes. Therefore, the new termination criterion, hereafter named *hybrid criterion*, requires that

$$\|\mathcal{R}(\mathbf{X}_k)\| < r_s \tau_s, \qquad k \geq 0. \tag{3.57}$$

Notice that the relation (3.57) can be applied also before starting the iterations, *i.e.* $k = 0$, by using the scaling ratio r_s defined in the previous system solution.

The hybrid criterion has the clear advantage to control the solution approximation error at the actual iteration k of the iterative method. Nevertheless, this criterion may require a higher computational cost because of the computation of both residuals and increments; moreover for a small number of iterations the scaling ratio r_s can be inaccurate since the condition (3.54) is true for $k \to \infty$ but could not be verified for early iterations.

In order to reduce the computational cost of the hybrid criterion we decide to compute increments only for the first linear/non-linear system solution at the time step $n = 1 + iM$, with M user-defined and $i \in \mathbb{N}$. Furthermore, for these particular systems the iterative process is performed until the machine error ε limit thus defining r_s with the maximum accuracy. Notice that r_s is frozen over M steps.

The hybrid criterion is here applied to all implicit schemes defined in Sec. 2.6 and thus to both linear and non-linear iterative methods, *i.e.* GMRES and

Newton-Krylov methods. However, we define one scaling ratio for each working variable w_j

$$r_{s,w_j} = \min_{i\in[1,k]} \frac{\|\mathcal{R}\left(\mathbf{X}_{i-1}\right)\|}{\|\mathbf{X}_{w_j,i-1} - \mathbf{X}_{w_j,i}\|}, \qquad \forall j = 1,\dots,m. \tag{3.58}$$

As a consequence, the iteration process is stopped only if the relation (3.57) is verified for all working variables

$$\|\mathcal{R}\left(\mathbf{X}_k\right)\| < r_{s,w_j}\tau_{s,w_j}, \qquad \forall j = 1,\dots,m. \tag{3.59}$$

When the machine error limit is required, the stop condition becomes

$$\|\mathcal{R}\left(\mathbf{X}_k\right)\| < 10 \max_{j\in[1,m]} \left(r_{s,w_j}\right)\varepsilon, \tag{3.60}$$

where 10 is a safety factor.

We remember that $\mathbf{X}_k = \mathbf{W}_k^i$, $\mathbf{X}_k = \mathbf{Y}_k^i$ and $\mathbf{X}_k = \mathbf{W}_k^{i,n} - \mathbf{W}_0^i$ for ESDIRK, Rosenbrock and Peer schemes, respectively.

3.4.1 Threshold tolerance and Local Truncation Error

In order the preserve the time integration accuracy, the approximation error of the system solution must be smaller than the local truncation error. Moreover, when the adaptive step-size algorithm is activated the correct evaluation of the local estimator must be ensured. Therefore, the threshold tolerance of iterative methods is set for all stages at the step Δt^n as

$$\tau_{s,w_j} = \zeta_s \ \min\left(\|LTE_{w_j}^{n+1}\|, r_{w_j}^{n+1}\right), \tag{3.61}$$

where ζ_s is a safety factor hereafter imposed $\zeta_s = 1/10$ unless otherwise specified.

The local estimator r is computed from the asymptotic behaviour (3.7) where the constant error is extrapolated from previous steps using the same process described for the adaptive algorithm in Sec. 3.2.1.

The local truncation error LTE, instead, can be computed only at the first step as pointed out in Sec. 3.1. However, simply exploiting the hypothesis of the adaptive time step strategy (3.10), here we derive an approximating value. Indeed, combining the asymptotic behaviours (3.6) and (3.7)

$$\|LTE^{n+1}\| = \psi_l^{n+1}\left(\psi_r^{n+1}\right)^{-\frac{q_l}{q_r}}\left(r^{n+1}\right)^{\frac{q_l}{q_r}}, \tag{3.62}$$

and applying the hypothesis (3.10) it follows that

$$\psi_l^{n+1}\left(\psi_r^{n+1}\right)^{-\frac{q_l}{q_r}} = cost. = \psi_l^{1}\left(\psi_r^{1}\right)^{-\frac{q_l}{q_r}}, \tag{3.63}$$

where the dependence on the working variable w_j is omitted for notational convenience. Therefore, the LTE is derived by Eq. (3.6) imposing the local constant as

$$\psi_l^{n+1} = \psi_l^1 \left(\frac{\psi_r^{n+1}}{\psi_r^1} \right)^{\frac{q_l}{q_r}}. \tag{3.64}$$

Local and estimator constants at the first step can be easily defined only once during a pre-processing step.

The threshold tolerance τ_{s,w_j} defined in Eq. (3.61) fulfils the local accuracy of the temporal scheme ensuring at the same time the correct evaluation of the local estimator. However, for robustness purposes, when a time step is rejected by the adaptation algorithm we impose the machine error limit condition (3.60) to the hybrid criterion.

3.5 Modified Newton-Krylov method

The ESDIRK time integration lead to the non-linear system of equations (2.103) that written in the compact form reads

$$\mathcal{R}(\mathbf{W}^i) = \mathbf{A}\mathbf{W}^i + \mathbf{B}(\mathbf{W}^i) = \mathbf{0}. \tag{3.65}$$

Here we solve the system (3.65) by means of the iterative Newton-Krylov method which entails the repeated solution of linear systems (2.104) in the compact form

$$\left. \frac{\partial \mathcal{R}(\mathbf{W}^i)}{\partial \mathbf{W}^i} \right|_k \Delta \mathbf{W}_k^i - \mathcal{R}(\mathbf{W}_k^i) = \mathbf{0}, \qquad k \geq 0, \tag{3.66}$$

$$\Delta \mathbf{W}_k^i = \mathbf{W}_{k+1}^i - \mathbf{W}_k^i, \tag{3.67}$$

which must be solved again iteratively using a linear method, *i.e.* GMRES method.

It is therefore easy to realize that, even with the adoption of initial guess approaches and of termination criteria described in previous sections, the non-linear solution can still require an high computational cost. Indeed, the global matrix $\partial \mathcal{R}(\mathbf{W}^i)/\partial \mathbf{W}^i$, and thus the analytical Jacobian matrix $\mathbf{J_P}$, should be computed at each newton iteration k hence representing a strong source of computational cost especially when using higher DG polynomial orders. Besides, solve each linear system (3.66) with the maximum accuracy, *i.e.* machine error, is in general too much expensive and moreover useless since it is not a necessary condition for preserving the Newton quadratic convergence rate.

In order to reduce these costs, several strategies can be applied to Newton method which hence is renamed as *modified/inexact* Newton method. Eisenstat and Walker [30] defined an algorithm to determine the cut-off criterion of the

linear systems solution able to ensure the expected convergence rate of Newton method. Moreover, Knoll and Keyes [45] suggest the possibility to replace the Jacobian matrix by a finite differences approximation. However, in this work we follow different approaches.

The global matrix, computed at the first iteration of the first non-linear system solution, is here recomputed only if the convergence rate of the modified Newton method between iteration $k-1$ and k decreases below a given threshold value

$$\frac{\|\Delta \mathbf{W}_k^i\|}{\|\Delta \mathbf{W}_{k-1}^i\|} > \tau_J, \qquad k \geq 1, \tag{3.68}$$

where τ_J is here set to 0.2. This choice requires to freeze the Jacobian matrix between iterations, stages and steps as well and, despite the main disadvantage of degrading the Newton quadratic convergence rate, it lead to the saving of a large amount of computational resources.

Notice that the condition (3.68) can be applied only for $k \geq 1$ thus giving none information for the first iteration where the matrix remains frozen. Basing on our experience no issues are expected until very large step-sizes are used (step-sizes for which the time integration accuracy, even for higher order ESDIRK schemes, is remarkably poor).

Since the choice of freezing the Jacobian matrix reduces the convergence rate then it reduces the linear solution accuracy requirement as well. Therefore, the forcing term η_J, defined as the relative tolerance of the linear system solution (3.66)

$$\left\| \left. \frac{\partial \mathcal{R}(\mathbf{W}^i)}{\partial \mathbf{W}^i} \right|_k \Delta \mathbf{W}_k^i - \mathcal{R}(\mathbf{W}_k^i) \right\| \leq \eta_J \left\| \mathcal{R}(\mathbf{W}_k^i) \right\|, \qquad k \geq 0, \tag{3.69}$$

can be set much higher. Forcing term values of $\eta_J = 1/10$ and $\eta_J = 1/100$ proved to be good choices for compressible and incompressible flows, respectively.

3.6 Peer methods starting procedure

Peer methods defined in Sec. 2.6.3 are multi-step and multi-stage time integration schemes. As all multi-step schemes, they are not self-starting, that means they need a set of starting solutions $\mathbf{W}^{i,0}$ at times

$$t^{i,0} = t^{st} + c_i \Delta t^{st}, \qquad i = 1, \ldots, s, \tag{3.70}$$

where

$$\Delta t^{st} = t^1 - t^{st}, \tag{3.71}$$

in order to perform the first step $n = 1$.

Gerisch *et al.* [34] suggest to compute starting solutions using one time step of a one-step method with continuous output and to control their accuracy by means of standard adaptive time step algorithm or by choosing Δt^{st} sufficiently small. However, even if straightforward and fast this strategy has three main drawbacks

- the one-step method must provide a continuous output,
- the continuous output, in general, has a different accuracy with respect to the one-step method and this must be taken into account for the choice of the starting step-size Δt^{st},
- for continuous output with low order of accuracy the starting step-size can be excessively small, leading to a large first step-size ratio $\sigma^1 = \Delta t^1 / \Delta t^{st}$ that reduces the peer order from s to $s-1$.

In order to overcome these drawbacks in this work we introduce a new starting procedure for Peer methods based on the local and global asymptotic behaviours of time integration errors.

Defining

$$c^- = \min_{i \in [1,s]} (c_i), \qquad t^- = t^{st} + c^- \Delta t^{st}, \tag{3.72}$$

as the minimum value of nodes c_i and the smallest time point of the starting procedure, respectively, and imposing that

$$t^- = t^0, \tag{3.73}$$

with t^0 the initial time, it follows from Eq. (3.70)

$$t^{i,0} = t^0 + \left(c_i - c^-\right) \Delta t^{st}, \qquad i = 1, \ldots, s, \tag{3.74}$$

and from Eq. (3.71)

$$t^1 = t^0 + \left(1 - c^-\right) \Delta t^{st}. \tag{3.75}$$

The starting procedure time-step Δt^{st} is here imposed equal to the user-defined initial time-step Δt^1 of Peer methods,

$$\Delta t^{st} = \Delta t^1, \tag{3.76}$$

in order to ensure $\sigma^1 = 1$. Moreover, the starting procedure time integration period can be derived from (3.74) as

$$T^{st} = \left(c^+ - c^-\right) \Delta t^{st}, \tag{3.77}$$

with $c^+ = \max_{i \in [1,s]} (c_i)$.

Starting solutions at corresponding times $t^{i,0}$ can be obtained by means of a one-step time integration scheme, *e.g.* Rosenbrock or ESDIRK schemes with

global order q'_g and local order q'_l, knowing that for small time integration periods T' the asymptotic behaviour of the global error (3.5) can be written in a more general form

$$\|err_{T'}\| \propto (T')^x (\Delta t')^y , \tag{3.78}$$

where $\Delta t'$ is the arithmetic mean value of the step size during the time integration of the one-step scheme and the exponents x and y can be defined from global and local error definitions noting that

$$\begin{cases} \|err_{T'}\| \propto (\Delta t')^y \propto (\Delta t')^{q'_g} & T' = const. \\ \|err_{T'}\| \propto (\Delta t')^{x+y} \propto (\Delta t')^{q'_l} & T' = \Delta t', \end{cases} \tag{3.79}$$

that means

$$x = q'_l - q'_g, \qquad y = q'_g. \tag{3.80}$$

Imposing then a starting solution accuracy proportional to the accuracy of the Peer method used for the simulation, we find the relation

$$(T')^{q'_l - q'_g} (\Delta t')^{q'_g} \propto (\Delta t)^{q_g} , \tag{3.81}$$

where Δt is the arithmetic mean time-step used by the Peer method of order q_g. Knowing that

$$T' = T^{st}, \qquad \Delta t \approx \Delta t^1, \tag{3.82}$$

the mean step-size of the one-step method is derived from Eq. (3.81) exploiting Eqs. (3.76) and (3.77)

$$\Delta t' = \psi \left(\Delta t^1\right)^{\frac{q_g + q'_g - q'_l}{q'_g}} , \tag{3.83}$$

where the constant value must be defined by the user (for simplicity we consider $\psi = 1$).

After sorting the starting time points such that

$$t^0_j < t^0_{j+1}, \qquad j = 1, \ldots, s-1, \tag{3.84}$$

with in general $t^0_j \neq t^0_i$ for $j = i$, we find the number of steps,

$$N'_j = \text{int}\left(\frac{t^0_{j+1} - t^0_j}{\Delta t'}\right) + 1, \tag{3.85}$$

needed to integrate in time from t^0_j to t^0_{j+1} by means of the one-step scheme and, as a consequence, the corresponding fixed time-step

$$\Delta t'_j = \frac{t^0_{j+1} - t^0_j}{N'_j}. \tag{3.86}$$

Notice that $\Delta t'_j \leq \Delta t'$. Finally, imposing the initial condition

$$\mathbf{W}^{j=1,0} = \mathbf{W}(t^0), \tag{3.87}$$

the solution $\mathbf{W}^{j+1,0}$, with $j = 1, \ldots, s-1$, can be computed starting from $\mathbf{W}^{j,0}$ after N'_j steps of dimension $\Delta t'_j$ performed with the one-step temporal scheme.

The procedure described is applicable for a generic one-step scheme independently on its accuracy and without requiring any dense output, meanwhile ensuring the accuracy of the Peer method. However, we suggest to avoid the use of this strategy for $q'_g << q_g$ since from Eq. (3.83) the step-size $\Delta t'$ could became too small leading to an excessively expensive starting procedure. Furthermore, since it is not ensured in general that a one-step method provides the same order of accuracy for all system variables, *e.g.* some Rosenbrock schemes show an order reduction only for the pressure variable when applied to incompressible flows [5], then the exponent in Eq. (3.83) is set for safety purposes as the maximum between exponents computed from one-step scheme orders shown for each variable w_j

$$\frac{q_g + q'_g - q'_l}{q'_g} = \max_{j \in [1,m]} \left(\frac{q_g + q'_g - q'_l}{q'_g} \right)_{w_j} . \tag{3.88}$$

CHAPTER 4

Numerical results: part A

In this chapter we show and examine the robustness and efficiency improvements of the numerical strategies proposed in Cap. 3 for the simulation of two benchmark test cases: the advection of a compressible isentropic vortex and the advection-diffusion of incompressible travelling waves.

Afterwards, the potential of the proposed high-order coupling between DG method and implicit temporal schemes is demonstrated by performing the implicit Large Eddy simulation (ILES) of the massively separated compressible flow over periodic hills at $\mathrm{Re} = 10595$.

4.1 The isentropic vortex and travelling waves test cases

In this section we show the efficiency and robustness improvements of implicit time integration schemes introduced with the approaches proposed Chap. 3. Benchmark test cases are the transport of a compressible inviscid isentropic vortex [5,40,50] and the transport-diffusion of incompressible travelling waves [5].

The isentropic vortex (vortex) is defined by velocity and temperature perturbations of a uniform flow, with pressure, temperature, density and velocity

Figure 4.1: *Initial pressure and velocity magnitude fields for isentropic vortex (left) and travelling waves (right) test cases, respectively.*

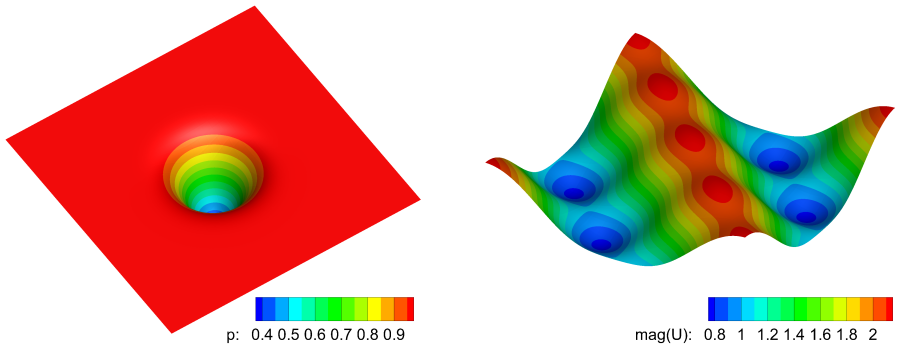

components equal to 1. Perturbations are given by

$$\begin{aligned} \delta u_1 &= -\frac{\alpha}{2\pi}\left(y - y_0\right) e^{\phi\left(1-r^2\right)}, \\ \delta u_2 &= \frac{\alpha}{2\pi}\left(x - x_0\right) e^{\phi\left(1-r^2\right)}, \\ \delta T &= -\frac{\alpha^2\left(\gamma - 1\right)}{16\phi\gamma\pi^2} e^{2\phi\left(1-r^2\right)}, \end{aligned} \tag{4.1}$$

where $\gamma = 1.4$ is the gas specific heats ratio, $\phi = 0.8$ and $\alpha = 4$ are parameters defining the vortex strength and r is the distance of a point (x, y) from the vortex center (x_0, y_0), placed at $(5, 5)$ at time $t^0 = 0$, that moves on the diagonal of a square domain $[0, 10] \times [0, 10]$ with all periodic boundaries. Therefore, the vortex period T is equal to ten non-dimensional convective times.

The travelling waves (waves) solution on the doubly-periodic unit square $[0.25, 1.25] \times [0.5, 1.5]$ is

$$u_1\left(x, y, t\right) = 1 + 2\cos\left(2\pi\left(x - t\right)\right)\sin\left(2\pi\left(y - t\right)\right) e^{-8\pi^2\nu t}, \tag{4.2}$$

$$u_2\left(x, y, t\right) = 1 - 2\sin\left(2\pi\left(x - t\right)\right)\cos\left(2\pi\left(y - t\right)\right) e^{-8\pi^2\nu t}, \tag{4.3}$$

$$p\left(x, y, t\right) = -\left(\cos\left(4\pi\left(x - t\right)\right) + \cos\left(4\pi\left(y - t\right)\right)\right) e^{-16\pi^2\nu t}, \tag{4.4}$$

with $\nu = 1\mathrm{e}{-2}$. Waves period T is equal to one non-dimensional convective time.

The initial pressure and initial velocity magnitude fields of isentropic vortex and travelling waves, respectively, are shown in Fig. 4.1. Solutions are computed at $t^N = T$ using a very accurate DG space discretization on a uniform quad mesh to keep the space discretization error well below the time integration error (see Tab. 4.1).

Results shown in Fig. 4.2 and 4.3 demonstrate that all ESDIRK and Rosenbrock schemes verify the formal order of convergence for all working variables

Table 4.1: *Inviscid vortex & travelling waves - DG space discretization data.*

	vortex	waves
Grid	16×16	4×4
Polynomial degree	$\mathbb{P}^{12}$	$\mathbb{P}^{13}$
DoF for each variable	23296	1680

Figure 4.2: *Isentropic vortex - Convergence analysis for the global error norm of working variables*

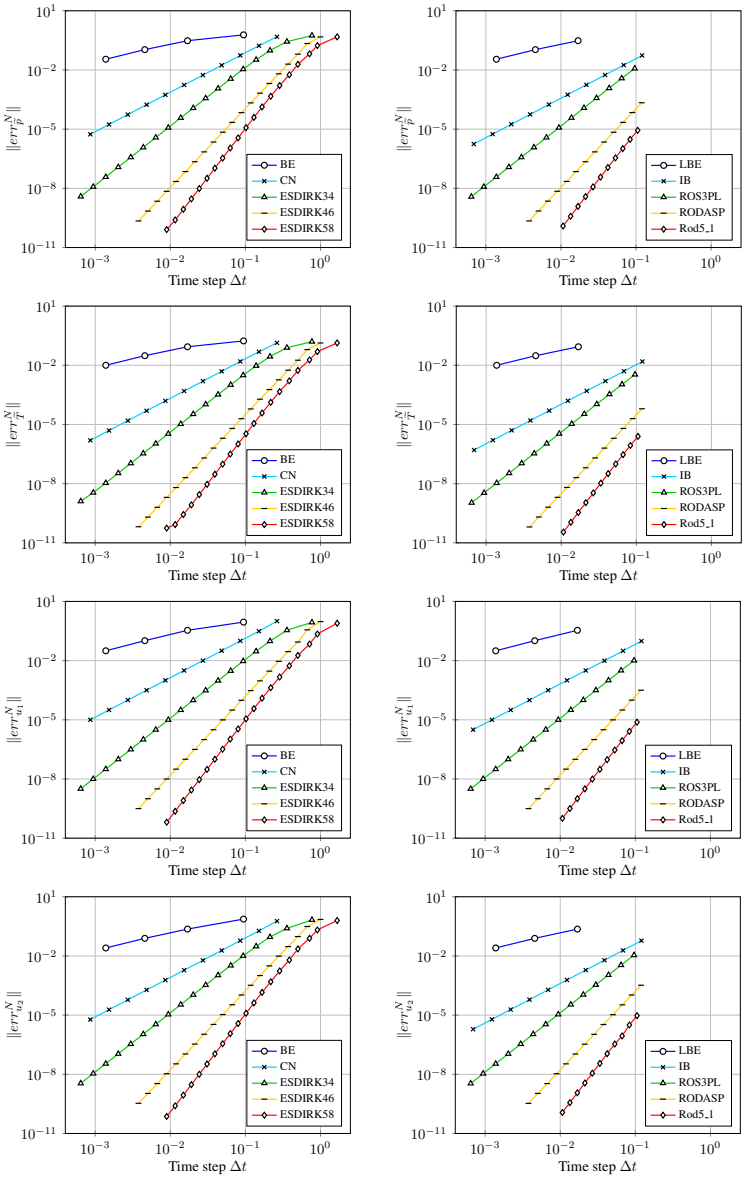

Table 4.2: *Isentropic vortex - List of local, global and estimator constants and orders*

	scheme	ψ_g^N	ψ_l^1	ψ_r^1	q_g	q_l	q_r
$\widetilde{p}$	BE	$2.53\mathrm{E}+01$	$1.93\mathrm{E}+00$	$1.21\mathrm{E}+00$	1	2	1
	CN	$7.42\mathrm{E}+00$	$1.34\mathrm{E}+00$	$1.93\mathrm{E}+00$	2	3	2
	ESDIRK34	$1.43\mathrm{E}+01$	$2.12\mathrm{E}+00$	$1.00\mathrm{E}-01$	3	4	3
	ESDIRK46	$1.10\mathrm{E}+00$	$4.84\mathrm{E}-01$	$1.89\mathrm{E}-02$	4	5	4
	ESDIRK58	$1.15\mathrm{E}+00$	$7.45\mathrm{E}-01$	$1.16\mathrm{E}-01$	5	6	6
	LBE	$2.53\mathrm{E}+01$	$1.93\mathrm{E}+00$	$1.21\mathrm{E}+00$	1	2	1
	IB	$3.69\mathrm{E}+00$	$7.21\mathrm{E}-01$	$8.01\mathrm{E}-01$	2	3	2
	ROS3PL	$1.43\mathrm{E}+01$	$2.13\mathrm{E}+00$	$3.61\mathrm{E}-01$	3	4	3
	RODASP	$1.11\mathrm{E}+00$	$6.24\mathrm{E}-01$	$3.53\mathrm{E}-01$	4	5	4
	Rod5_1	$8.81\mathrm{E}-01$	$6.67\mathrm{E}-01$	$6.37\mathrm{E}-01$	5	6	5
$\widetilde{T}$	BE	$7.24\mathrm{E}+00$	$5.53\mathrm{E}-00$	$3.46\mathrm{E}+01$	1	2	1
	CN	$2.12\mathrm{E}+00$	$3.84\mathrm{E}-01$	$5.53\mathrm{E}-01$	2	3	2
	ESDIRK34	$4.09\mathrm{E}+00$	$6.05\mathrm{E}-01$	$2.86\mathrm{E}-02$	3	4	3
	ESDIRK46	$3.15\mathrm{E}-01$	$1.38\mathrm{E}-01$	$5.40\mathrm{E}-03$	4	5	4
	ESDIRK58	$3.33\mathrm{E}-01$	$2.13\mathrm{E}-01$	$3.33\mathrm{E}-02$	5	6	6
	LBE	$7.24\mathrm{E}+00$	$5.53\mathrm{E}-01$	$3.46\mathrm{E}-01$	1	2	1
	IB	$1.05\mathrm{E}+00$	$2.06\mathrm{E}-01$	$2.29\mathrm{E}-01$	2	3	2
	ROS3PL	$4.09\mathrm{E}+00$	$6.09\mathrm{E}-01$	$1.03\mathrm{E}-01$	3	4	3
	RODASP	$3.18\mathrm{E}-01$	$1.78\mathrm{E}-01$	$1.01\mathrm{E}-01$	4	5	4
	Rod5_1	$2.52\mathrm{E}-01$	$1.91\mathrm{E}-01$	$1.82\mathrm{E}-01$	5	6	5
u_1	BE	$2.27\mathrm{E}+01$	$2.66\mathrm{E}+00$	$1.99\mathrm{E}+00$	1	2	1
	CN	$1.35\mathrm{E}+01$	$1.45\mathrm{E}+00$	$2.66\mathrm{E}+00$	2	3	2
	ESDIRK34	$1.20\mathrm{E}+01$	$1.80\mathrm{E}+00$	$1.08\mathrm{E}-01$	3	4	3
	ESDIRK46	$1.56\mathrm{E}+00$	$3.22\mathrm{E}-01$	$1.83\mathrm{E}-02$	4	5	4
	ESDIRK58	$1.09\mathrm{E}+00$	$4.29\mathrm{E}-01$	$7.73\mathrm{E}-02$	5	6	6
	LBE	$2.27\mathrm{E}+01$	$2.66\mathrm{E}+00$	$1.99\mathrm{E}+00$	1	2	1
	IB	$6.61\mathrm{E}+00$	$1.12\mathrm{E}+00$	$1.10\mathrm{E}+00$	2	3	2
	ROS3PL	$1.20\mathrm{E}+01$	$1.86\mathrm{E}+00$	$5.28\mathrm{E}-01$	3	4	3
	RODASP	$1.56\mathrm{E}+00$	$3.99\mathrm{E}-01$	$4.08\mathrm{E}-01$	4	5	4
	Rod5_1	$7.27\mathrm{E}-01$	$3.16\mathrm{E}-01$	$3.83\mathrm{E}-01$	5	6	5
u_2	BE	$1.84\mathrm{E}+01$	$2.66\mathrm{E}+00$	$1.99\mathrm{E}+00$	1	2	1
	CN	$8.10\mathrm{E}+00$	$1.45\mathrm{E}+00$	$2.66\mathrm{E}+00$	2	3	2
	ESDIRK34	$1.31\mathrm{E}+01$	$1.79\mathrm{E}+00$	$1.08\mathrm{E}-01$	3	4	3
	ESDIRK46	$1.68\mathrm{E}+00$	$3.19\mathrm{E}-01$	$1.83\mathrm{E}-02$	4	5	4
	ESDIRK58	$1.19\mathrm{E}+00$	$3.97\mathrm{E}-01$	$7.13\mathrm{E}-02$	5	6	6
	LBE	$1.84\mathrm{E}+01$	$2.66\mathrm{E}+00$	$1.99\mathrm{E}+00$	1	2	1
	IB	$4.02\mathrm{E}+00$	$1.12\mathrm{E}+00$	$1.10\mathrm{E}+00$	2	3	2
	ROS3PL	$1.31\mathrm{E}+01$	$1.85\mathrm{E}+00$	$5.28\mathrm{E}-01$	3	4	3
	RODASP	$1.68\mathrm{E}+00$	$3.96\mathrm{E}-01$	$4.05\mathrm{E}-01$	4	5	4
	Rod5_1	$8.34\mathrm{E}-01$	$3.24\mathrm{E}-01$	$3.73\mathrm{E}-01$	5	6	5

and both for ODEs (vortex) and DAEs (waves), where all errors are computed with respect to the available analytic solutions.

In Tab. 4.2, 4.3 are reported global, local and estimator constants and the respective orders obtained for both test cases. In particular, observing the orders

Table 4.3: *Travelling waves - List of local, global and estimator constants and orders*

	scheme	ψ_g^N	ψ_l^1	ψ_r^1	q_g	q_l	q_r
p	BE	$1.65\mathrm{E}+01$	$7.90\mathrm{E}+01$	$8.92\mathrm{E}+00$	1	2	1
	CN	$3.56\mathrm{E}+01$	$1.66\mathrm{E}+02$	$5.60\mathrm{E}+01$	2	3	2
	ESDIRK34	$1.39\mathrm{E}+02$	$6.49\mathrm{E}+02$	$8.76\mathrm{E}+00$	3	4	3
	ESDIRK46	$5.76\mathrm{E}+01$	$2.66\mathrm{E}+02$	$3.96\mathrm{E}+00$	4	5	4
	ESDIRK58	$9.71\mathrm{E}+01$	$4.46\mathrm{E}+02$	$3.30\mathrm{E}+01$	5	6	6
	LBE	$1.65\mathrm{E}+01$	$7.89\mathrm{E}+01$	$1.27\mathrm{E}+01$	1	2	1
	IB	$1.59\mathrm{E}+01$	$6.52\mathrm{E}+00$	$3.31\mathrm{E}+01$	2	2	2
	ROS3PL	$1.40\mathrm{E}+02$	$8.53\mathrm{E}+00$	$3.14\mathrm{E}+00$	3	3	2
	RODASP	$5.76\mathrm{E}+01$	$2.80\mathrm{E}+02$	$1.09\mathrm{E}+02$	4	5	4
	Rod5_1	$4.31\mathrm{E}+01$	$2.54\mathrm{E}+02$	$5.74\mathrm{E}+02$	5	6	5
u_1	BE	$2.58\mathrm{E}+01$	$5.61\mathrm{E}+01$	$8.92\mathrm{E}+00$	1	2	1
	CN	$5.55\mathrm{E}+01$	$1.18\mathrm{E}+02$	$5.60\mathrm{E}+01$	2	3	2
	ESDIRK34	$2.16\mathrm{E}+02$	$4.60\mathrm{E}+02$	$8.76\mathrm{E}+00$	3	4	3
	ESDIRK46	$8.89\mathrm{E}+01$	$1.89\mathrm{E}+02$	$3.96\mathrm{E}+00$	4	5	4
	ESDIRK58	$1.52\mathrm{E}+02$	$3.19\mathrm{E}+02$	$3.30\mathrm{E}+01$	5	6	6
	LBE	$2.58\mathrm{E}+01$	$5.60\mathrm{E}+01$	$8.92\mathrm{E}+00$	1	2	1
	IB	$2.69\mathrm{E}+01$	$5.71\mathrm{E}+01$	$2.32\mathrm{E}+01$	2	3	2
	ROS3PL	$2.16\mathrm{E}+02$	$4.60\mathrm{E}+02$	$2.92\mathrm{E}+01$	3	4	3
	RODASP	$8.88\mathrm{E}+01$	$1.89\mathrm{E}+02$	$6.90\mathrm{E}+01$	4	5	4
	Rod5_1	$6.75\mathrm{E}+01$	$1.40\mathrm{E}+02$	$1.26\mathrm{E}+02$	5	6	5
u_2	BE	$2.58\mathrm{E}+01$	$5.61\mathrm{E}+01$	$8.92\mathrm{E}+00$	1	2	1
	CN	$5.55\mathrm{E}+01$	$1.18\mathrm{E}+02$	$5.60\mathrm{E}+01$	2	3	2
	ESDIRK34	$2.16\mathrm{E}+02$	$4.60\mathrm{E}+02$	$8.76\mathrm{E}+00$	3	4	3
	ESDIRK46	$8.89\mathrm{E}+01$	$1.89\mathrm{E}+02$	$3.96\mathrm{E}+00$	4	5	4
	ESDIRK58	$1.52\mathrm{E}+02$	$3.19\mathrm{E}+02$	$3.30\mathrm{E}+01$	5	6	6
	LBE	$2.58\mathrm{E}+01$	$5.60\mathrm{E}+01$	$8.92\mathrm{E}+00$	1	2	1
	IB	$2.69\mathrm{E}+01$	$5.71\mathrm{E}+01$	$2.32\mathrm{E}+01$	2	3	2
	ROS3PL	$2.16\mathrm{E}+02$	$4.60\mathrm{E}+02$	$2.92\mathrm{E}+01$	3	4	3
	RODASP	$8.88\mathrm{E}+01$	$1.89\mathrm{E}+02$	$6.90\mathrm{E}+01$	4	5	4
	Rod5_1	$6.75\mathrm{E}+01$	$1.40\mathrm{E}+02$	$1.26\mathrm{E}+02$	5	6	5

found for the incompressible case we can see that the local order on pressure field for IB and ROS3PL schemes turns out to be lower than expected. Besides, for ROS3PL scheme only we also observe a reduction of the estimator order on pressure field.

As regards Peer schemes we want to show the effects of the new starting procedure proposed in Sec. 3.6. The procedure is here adopted using as one-step schemes the Rosenbrock ROS3PL, RODASP and Rod5_1 schemes, where the ROS3PL is used for all Peer methods while higher order RODASP and Rod5_1 are applied only to peer5A and peer6A, respectively. In Tabs. 4.4 and 4.5 are reported global errors and orders obtained for the travelling wave test case using on one hand the exact starting values $\mathbf{W}^{i,0}$ and on the other hand the numerical values computed with the starting procedure. Notice that for all

Figure 4.3: *Travelling waves - Convergence analysis for the global error norm of working variables*

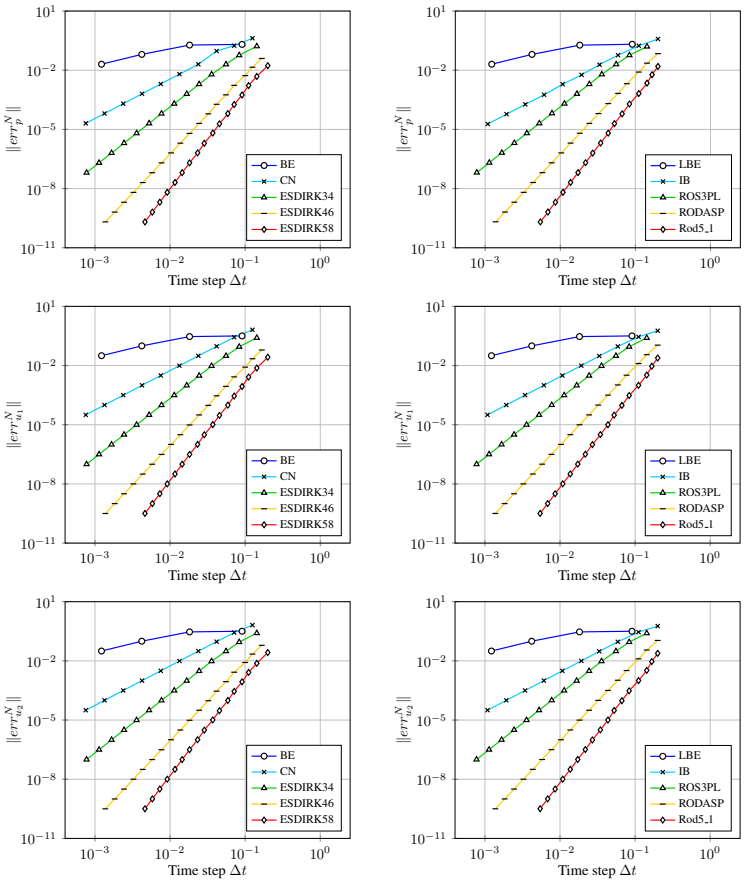

Peer methods and with all one-step schemes the starting procedure preserves the global accuracy. Nevertheless, we point out that with a lower order one-step scheme the starting procedure becomes more expensive thus reducing the overall efficiency of the Peer method as shown in Tab. 4.5 for the peer5A and peer6A schemes in terms of work unit. Notice that, due to the machine error limit, the peer6A scheme is not able to verify the order of convergence at smallest time step.

It could be useful knowing that for all temporal schemes the CFL condition, *i.e.* CFL$= 1$ where the Courant number is computed with respect to the maximum eigenvalue of the Jacobian matrix, applied to all mesh elements requires $\Delta t < 1/400$ and $\Delta t < 1/23000$ for the vortex and the waves, respectively. Therefore, results here obtained prove that, thanks to the implicit treatment of the integration in time, for these benchmark test cases and with the applied very high-order DG discretization we are able to perform simulations through step-

Table 4.4: *Travelling waves - Pressure and velocity components global error norms and computed orders of convergence for Peer schemes with exact initial values* $\mathbf{W}^{i,0}$. $T = t^N = 1$ *is the time integration period.*

	Δt	$\|err_p^N\|$	order	$\|err_{u_1}^N\|$	order	$\|err_{u_2}^N\|$	order
	T/40	1.78E-01	1.57	2.76E-01	1.57	2.76E-01	1.57
	T/80	3.74E-02	2.92	5.82E-02	2.92	5.82E-02	2.92
peer3A	T/160	4.84E-03	2.98	7.54E-03	2.98	7.54E-03	2.98
	T/320	6.13E-04	2.99	9.54E-04	2.99	9.54E-04	2.99
	T/400	3.15E-04	-	4.90E-04	-	4.90E-04	-
	T/40	8.53E-03	3.74	1.33E-02	3.73	1.33E-02	3.73
	T/80	6.01E-04	3.93	9.36E-04	3.93	9.36E-04	3.93
peer4A	T/160	3.88E-05	3.98	6.04E-05	3.98	6.04E-05	3.98
	T/320	2.45E-06	3.99	3.82E-06	3.99	3.82E-06	3.99
	T/400	1.01E-06	-	1.57E-06	-	1.57E-06	-
	T/40	2.75E-04	4.89	4.28E-04	4.89	4.28E-04	4.89
	T/80	9.07E-06	4.97	1.41E-05	4.97	1.41E-05	4.97
peer5A	T/160	2.87E-07	4.99	4.47E-07	4.99	4.47E-07	4.99
	T/320	9.02E-09	5.00	1.40E-08	5.00	1.40E-08	5.00
	T/400	2.96E-09	-	4.60E-09	-	4.60E-09	-
	T/40	7.66E-06	5.98	1.19E-05	5.98	1.19E-05	5.98
	T/80	1.20E-07	6.01	1.86E-07	6.01	1.86E-07	6.01
peer6A	T/160	1.87E-09	5.80	2.89E-09	6.03	2.89E-09	6.03
	T/320	1.78E-10	-	4.06E-11	-	4.06E-11	-
	T/400	1.76E-10	-	1.81E-11	-	1.81E-11	-

sizes even one hundred times larger than the CFL limit without any stability issue.

4.1.1 Time integration robustness and efficiency improvements

The results presented above have been obtained without using neither time adaptation nor improved initial guess strategies reported in Chap. 3. Moreover the stopping criterion has been set to machine error limit. These results, hereinafter referred as base results (base), are now compared with results obtained using respectively the initial guess approach (guess), the stopping criterion (stop), the time step adaptation (adp) and all strategies activated (all). We would like to underline that the stopping criterion is here applied for both test cases imposing the severe limit values $\zeta_s = 1$ and $M \to \infty$. This means that the threshold tolerance is exactly $\tau_{s,w_j} = \min(LTE_{w_j}^{n+1}, r_{w_j}^{n+1})$ and the scaling ratio r_s is frozen during the whole simulation to the value found at the first time step.

Here for the sake of simplicity we analyse the robustness and efficiency improvements of developed numerical approaches only for the 4th order ESDIRK46 and RODASP schemes as examples of implicit and linearly-implicit

Table 4.5: *Travelling waves - Pressure and velocity components global error norms and computed orders of convergence for Peer schemes with numerical starting procedure. The one-step scheme used for the starting procedure is reported inside the brackets.* $T = t^N = 1$ *is the time integration period.*

	Δt	$\|err_p^N\|$	order	$\|err_{u_1}^N\|$	order	$\|err_{u_2}^N\|$	order	work unit
	T/40	1.78E-01	1.57	2.76E-01	1.57	2.76E-01	1.57	2.66E+03
	T/80	3.74E-02	2.92	5.82E-02	2.92	5.82E-02	2.92	3.02E+03
peer3A (ROS3PL)	T/160	4.84E-03	2.98	7.54E-03	2.98	7.54E-03	2.98	3.88E+03
	T/320	6.13E-04	2.99	9.54E-04	2.99	9.54E-04	2.99	5.58E+03
	T/400	3.15E-04	-	4.90E-04	-	4.90E-04	-	6.55E+03
	T/40	8.52E-03	3.74	1.33E-02	3.73	1.33E-02	3.73	1.78E+03
	T/80	6.01E-04	3.93	9.35E-04	3.93	9.35E-04	3.93	2.22E+03
peer4A (ROS3PL)	T/160	3.88E-05	3.98	6.04E-05	3.98	6.04E-05	3.98	3.28E+03
	T/320	2.45E-06	3.99	3.81E-06	3.99	3.81E-06	3.99	6.16E+03
	T/400	1.01E-06	-	1.57E-06	-	1.57E-06	-	7.15E+03
	T/40	2.75E-04	4.89	4.29E-04	4.89	4.29E-04	4.89	1.60E+03
	T/80	9.07E-06	4.97	1.41E-05	4.97	1.41E-05	4.97	2.14E+03
peer5A (RODASP)	T/160	2.87E-07	4.99	4.47E-07	4.99	4.47E-07	4.99	3.62E+03
	T/320	9.02E-09	5.00	1.40E-08	5.00	1.40E-08	5.00	6.03E+03
	T/400	2.96E-09	-	4.60E-09	-	4.60E-09	-	7.63E+03
	T/40	2.75E-04	4.89	4.29E-04	4.89	4.29E-04	4.89	1.54E+03
	T/80	9.08E-06	4.97	1.41E-05	4.97	1.41E-05	4.97	2.25E+03
peer5A (ROS3PL)	T/160	2.87E-07	4.99	4.48E-07	4.99	4.48E-07	4.99	3.89E+03
	T/320	9.03E-09	4.99	1.41E-08	5.00	1.41E-08	5.00	7.50E+03
	T/400	2.96E-09	-	4.61E-09	-	4.61E-09	-	7.78E+03
	T/40	7.66E-06	5.98	1.19E-05	5.98	1.19E-05	5.98	1.66E+03
	T/80	1.20E-07	6.01	1.86E-07	6.01	1.86E-07	6.01	2.24E+03
peer6A (Rod5_1)	T/160	1.87E-09	5.80	2.89E-09	6.03	2.89E-09	6.03	3.81E+03
	T/320	1.78E-10	-	4.06E-11	-	4.06E-11	-	6.16E+03
	T/400	1.79E-10	-	1.81E-11	-	1.81E-11	-	6.75E+03
	T/40	7.65E-06	5.99	1.19E-05	5.98	1.19E-05	5.98	2.32E+03
	T/80	1.20E-07	6.00	1.86E-07	6.00	1.86E-07	6.00	4.72E+03
peer6A (ROS3PL)	T/160	1.86E-09	5.79	2.89E-09	6.02	2.89E-09	6.02	9.03E+03
	T/320	1.79E-10	-	4.05E-11	-	4.05E-11	-	1.98E+04
	T/400	1.74E-10	-	1.80E-11	-	1.80E-11	-	2.42E+04

time integration schemes respectively. Moreover we report only the results for the velocity component u_2, the working variable on which is defined the adaptive algorithm, knowing that all the conclusions are also valid for the remaining variables.

First of all, we prove that all developed numerical approaches preserve the theoretical order of convergence. This can be easily seen in Figs. 4.4 and 4.5 where none approach degrades the schemes accuracy.

Furthermore, it is of particular interest to see the effects of the tolerance proportionality and calibration applied with step-size adaptation (see Figs. 4.6 and 4.7). Thanks to the proportionality, a variation on absolute tolerance leads to vary the global error of the same quantity. Besides, with the calibration constants τ_ψ reported in Tab. 4.6 we are able to ensure the condition $\tau_a =$

Figure 4.4: *Isentropic vortex - Comparison of the velocity component u_2 global error norm obtained using ESDIRK46 and RODASP schemes with the initial guess approach (guess), the stopping criterion (stop), the time step adaptivation (adp) and all strategies (all) activated. For the base configuration (base) standard initial guesses and constant step-sizes are used and machine error limit is required to system solution.*

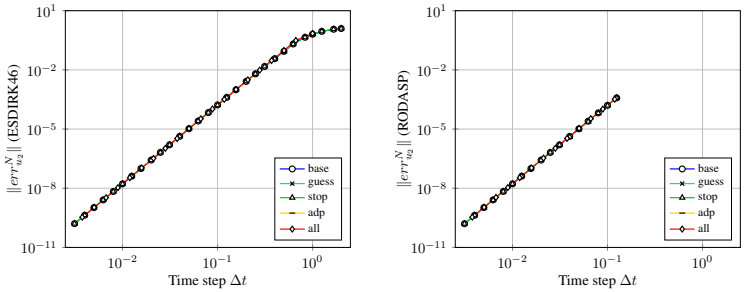

Figure 4.5: *Travelling waves - Comparison of the velocity component u_2 global error norm obtained using ESDIRK46 and RODASP schemes with different strategies activated.*

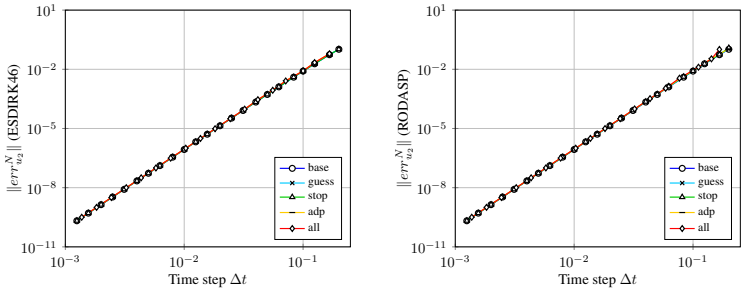

Table 4.6: *Inviscid vortex & travelling waves - List of calibration constants τ_ψ (3.28) computed for the velocity component u_2.*

	$\tau_{\psi,vortex}$	$\tau_{\psi,waves}$
ESDIRK46	$1.17\text{E}-02$	$3.04\text{E}-02$
RODASP	$2.61\text{E}-01$	$5.33\text{E}-01$

$\|err^N_{u_2}\|$. The relative tolerance τ_r is here set to the machine error limit.

In Figs. 4.8 and 4.9 we compare efficiency improvements in terms of total number of GMRES iterations. We can see that each strategy has a different behaviour with respect to the step-size. Since it is based on an extrapolation process which produces more accurate initial guesses for $\Delta t \to 0$, the initial guess approach gives best improvements for smallest time steps. Conversely the hybrid stopping criterion ensures better efficiency enhancements for higher step-sizes since temporal scheme accuracy requirements are less restrictive thus allowing to consider higher threshold tolerance values. The adaptive algorithm instead does not show performance increments because the step-size

Figure 4.6: *Isentropic vortex - Velocity component u_2 global error norm versus the adaptive absolute tolerance τ_a imposed in Eq.* (3.21) *where the relative tolerance τ_r is set to the machine error limit. Dashed lines represent the condition $\tau_a = \|err^N_{u_2}\|$.*

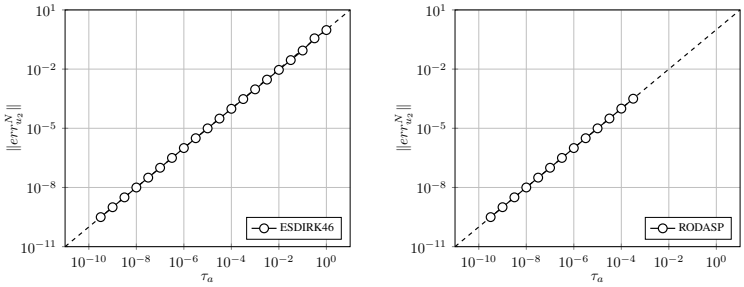

Figure 4.7: *Travelling waves - Velocity component u_2 global error norm versus the adaptive absolute tolerance τ_a imposed in Eq.* (3.21) *where the relative tolerance τ_r is set to the machine error limit. Dashed lines represent the condition $\tau_a = \|err^N_{u_2}\|$.*

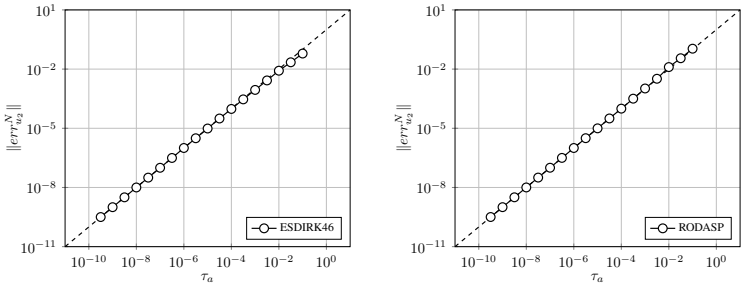

Figure 4.8: *Isentropic vortex - Comparison of the velocity component u_2 global error norm in terms of total number of GMRES iterations obtained using ESDIRK46 and RODASP schemes with the different strategies activated.*

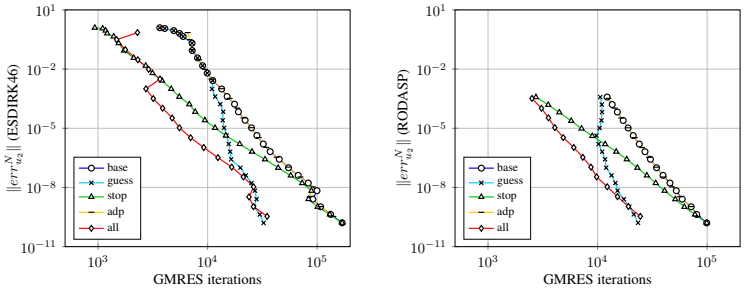

remains roughly constant for these simple test cases. Moreover, no step rejection is needed. Finally, the simultaneous activation of all strategies minimizes the computational effort on iterative system solution by fulfilling the advantages of each approach except for few simulations at extremely high step-sizes where some step rejection occurred.

In Figs. 4.10 and 4.11 we show performances enhancements in term of com-

Figure 4.9: *Travelling waves - Comparison of the velocity component u_2 global error norm in terms of total number of GMRES iterations obtained using ESDIRK46 and RODASP schemes with the different strategies activated.*

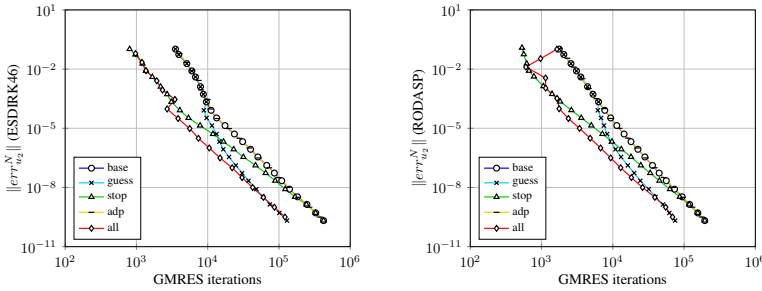

Figure 4.10: *Isentropic vortex - Comparison of the velocity component u_2 global error norm in terms of wall time [s] obtained using ESDIRK46 and RODASP schemes with the different strategies activated.*

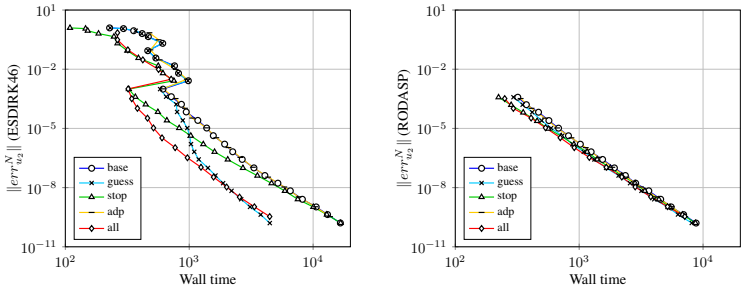

Figure 4.11: *Travelling waves - Comparison of the velocity component u_2 global error norm in terms of wall time [s] obtained using ESDIRK46 and RODASP schemes with the different strategies activated.*

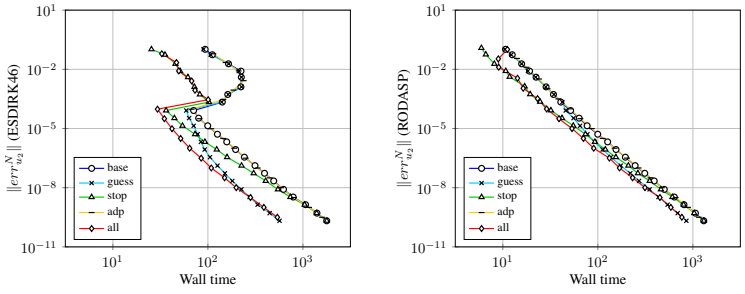

putational time. All considerations previously derived regarding GMRES iterations are here still valid. Furthermore, we are also able to analyse the Jacobian matrix impact on the computational cost. More in particular, for the ESDRIK46 scheme, as for all temporal schemes that use the modified newton method here applied, for sufficiently small step-sizes the matrix is usually

Table 4.7: *Isentropic vortex - Time integration efficiency enhancements for ESDIRK46 and RODASP schemes in terms of GMRES iterations ($\Delta_{\%}It_{GMRES}$) and wall time ($\Delta_{\%}t_{wall}$) reduction.*

	τ_a	Δt	$\|err_v^N\|$	$\Delta_{\%}It_{GMRES}$	$\Delta_{\%}t_{wall}$	speedup
ESDIRK46	$1.00\text{E}-04$	$8.85\text{E}-02$	$1.04\text{E}-04$	-79.2	-58.7	2.42
	$1.00\text{E}-05$	$5.00\text{E}-02$	$1.06\text{E}-05$	-78.0	-62.6	2.68
	$1.00\text{E}-06$	$2.82\text{E}-02$	$1.06\text{E}-06$	-73.1	-62.9	2.69
	$1.00\text{E}-07$	$1.59\text{E}-02$	$1.07\text{E}-07$	-69.3	-61.9	2.62
	$1.00\text{E}-08$	$8.94\text{E}-03$	$1.07\text{E}-08$	-71.3	-65.8	2.92
	$1.00\text{E}-09$	$5.03\text{E}-03$	$1.06\text{E}-09$	-75.5	-67.8	3.10
RODASP	$1.00\text{E}-04$	$8.89\text{E}-02$	$1.03\text{E}-04$	-78.5	-28.7	1.40
	$1.00\text{E}-05$	$5.03\text{E}-02$	$1.08\text{E}-05$	-78.4	-19.2	1.24
	$1.00\text{E}-06$	$2.82\text{E}-02$	$1.06\text{E}-06$	-76.1	-19.2	1.24
	$1.00\text{E}-07$	$1.59\text{E}-02$	$1.07\text{E}-07$	-74.7	-10.6	1.12
	$1.00\text{E}-08$	$8.94\text{E}-03$	$1.08\text{E}-08$	-74.2	-10.3	1.11
	$1.00\text{E}-09$	$5.03\text{E}-03$	$1.08\text{E}-09$	-73.2	-7.3	1.08

frozen through several time steps while for very high values of Δt it is computed more than once for each step hence increasing considerably the execution time. Conversely, for RODASP scheme, and more in general for linearly implicit schemes, the matrix must always be computed once per step and therefore represents a large part of the step computational cost independently on the Δt value. As a consequence, the efficiency improvements in terms of wall time are limited especially for ODEs system, *i.e.* vortex test case, where the GMRES method converges very quickly.

Results reported in Tab. 4.7 and 4.8 and obtained by activating all the strategies developed in this work clearly show what has been previously mentioned. Indeed, although we are able to reduce the total number of GMRES iterations of $60/80\%$ for both linear and non-linear iterative methods and for both ODEs and DAEs, the computational effort reduction ($\Delta_{\%}t_{wall}$) for the RODASP scheme ($\approx -20/-30\%$) is strongly limited with respect to the ESDIRK46 one ($\approx -60\%$). Nevertheless, we can see that the proposed approaches are able to provide a remarkable maximum speedup equal to 3 for ESDIRK46 and to $1.4/1.7$ for RODASP schemes for both inviscid vortex and travelling waves test cases.

4.2 Flow over periodic hills

The reliability of the proposed implicit and globally high-order approach to the simulation of unsteady turbulent flows is here demonstrated on the ILES of the compressible flow over periodic hills. More in particular, no subgrid-scale models are included in the governing equations and all numerical approaches developed in Chap. 3 and tested in Sec. 4.1 are applied.

Table 4.8: *Travelling waves - Time integration efficiency enhancements for ESDIRK46 and RODASP schemes in terms of GMRES iterations ($\Delta_{\%}It_{GMRES}$) and wall time ($\Delta_{\%}t_{wall}$) reduction.*

	τ_a	Δt	$\|err_{u_2}^N\|$	$\Delta_{\%}It_{GMRES}$	$\Delta_{\%}t_{wall}$	speedup
ESDIRK46	$1.00\text{E}-04$	$3.22\text{E}-02$	$9.54\text{E}-05$	-75.3	-56.3	2.29
	$1.00\text{E}-05$	$1.81\text{E}-02$	$9.73\text{E}-06$	-71.9	-61.3	2.59
	$1.00\text{E}-06$	$1.03\text{E}-02$	$1.00\text{E}-06$	-72.6	-66.0	2.94
	$1.00\text{E}-07$	$5.78\text{E}-03$	$9.95\text{E}-08$	-69.8	-67.5	3.08
	$1.00\text{E}-08$	$3.26\text{E}-03$	$1.00\text{E}-08$	-67.9	-66.4	2.98
	$1.00\text{E}-09$	$1.83\text{E}-03$	$1.00\text{E}-09$	-67.7	-66.5	2.99
RODASP	$1.00\text{E}-04$	$3.22\text{E}-02$	$9.80\text{E}-05$	-76.4	-43.1	1.76
	$1.00\text{E}-05$	$1.81\text{E}-02$	$9.91\text{E}-06$	-72.5	-38.2	1.62
	$1.00\text{E}-06$	$1.03\text{E}-02$	$1.00\text{E}-06$	-69.1	-39.7	1.66
	$1.00\text{E}-07$	$5.78\text{E}-03$	$1.00\text{E}-07$	-66.7	-37.0	1.59
	$1.00\text{E}-08$	$3.26\text{E}-03$	$1.00\text{E}-08$	-62.7	-33.6	1.51
	$1.00\text{E}-09$	$1.83\text{E}-03$	$1.00\text{E}-09$	-57.9	-33.9	1.51

Figure 4.12: *Second order curved mesh for the periodic hill test case.*

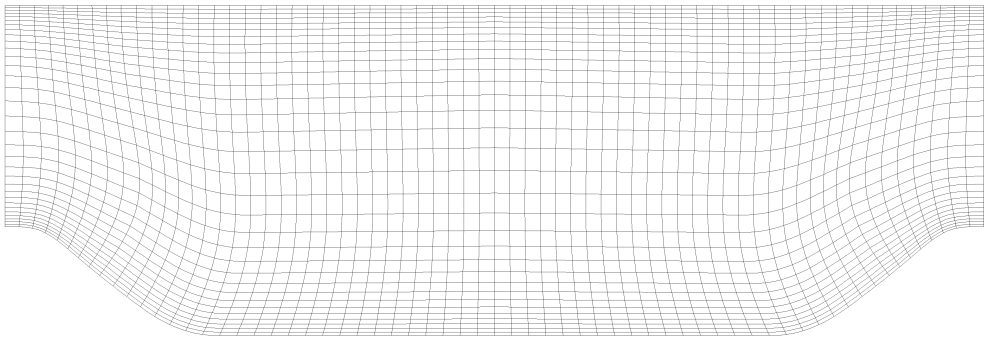

The flow over periodic hills is a test case deeply analysed in literature [17,32,49] and it is part of the test case repository defined inside the EU project TILDA (Towards Industrial LES/DNS in Aeronautics - Paving the Way for Future Accurate CFD). The flow is computed for the hill hight h based Reynolds number $\mathrm{Re}_h = 10595$ and for the Mach number $\mathrm{M} = 0.1$, thus matching incompressible conditions. The channel length and heigh are $L_x = 9h$ and $L_y = 3.035h$, respectively, and the spanwise extent is $L_z = 4.5h$. The second order mesh is composed of $64 \times 32 \times 32$ elements (see Fig. 4.12). Computations are performed with DG $\mathbb{P}^2$ and $\mathbb{P}^4$ polynomial degrees leading to $655\,360$ and $2\,293\,760$ DoF per equation, respectively.

The domain is periodic in streamwise and spanwise directions. At solid upper and lower walls the isothermal no-slip boundary condition is imposed using non-dimensional temperature of $T_w = 1$. The non-periodic behaviour of the pressure distribution is handled by adding the mean pressure gradient

Figure 4.13: *Periodic hills - Comparison of the velocity component u_2 global error norm in terms of wall time [s] obtained using DG $\mathbb{P}^2$ (left) and $\mathbb{P}^4$ (right).*

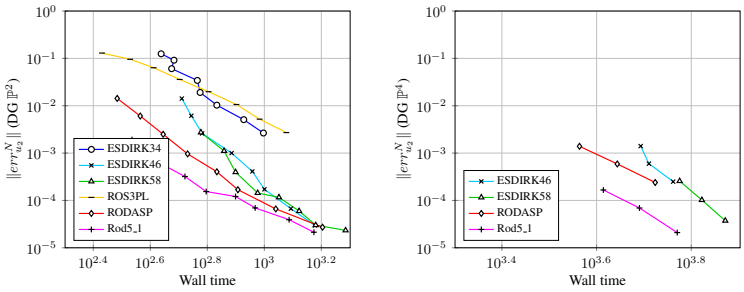

as a source term, imposed uniform over the whole domain, to the momentum equation in streamwise direction.

The pressure gradient $\partial p^n/\partial x$, set constant at time step Δt^n, is derived following the Benocci and Pinelli approach [13] modified in order to take into account of non constant step-sizes

$$\frac{\partial p}{\partial x}^n = \frac{\partial p}{\partial x}^{n-1} + \zeta_h \frac{2}{\rho_h \Delta t^n \left(1+\sigma^n\right)} \left[\dot{m}_h - \dot{m}^n \left(1+\sigma^n\right) + \dot{m}^{n-1}\sigma^n\right], \quad (4.5)$$

where $\sigma^n = \Delta t^n/\Delta t^{n-1}$ and $\zeta_h = 1/10$ is a safety factor that proved to be very useful to control temporal oscillations of the forcing term when dealing with high time steps. The parameter $\dot{m}_h$ is the mass flow rate, here considered averaged on the whole domain, which ensures the prescribed Re_h. $\dot{m}^n$ and $\dot{m}^{n-1}$ are the numerical averaged mass flow rates computed at previous steps.

The choice of the temporal scheme is performed by comparing the efficiencies of high order ESDIRK and Rosenbrock schemes for $\mathbb{P}^2$ and $\mathbb{P}^4$ DG discretizations with initial guess approach and hybrid stopping criterion activated. More in detail, for the stopping criterion, data reported in Tab. 4.9 are used. The comparison between different temporal schemes obtained after one reference period $T = L_x/u_b$, with u_b the prescribed bulk velocity at hill crest, and starting from a fully-developed turbulent flow is shown in Fig. 4.13. The step-sizes considered are $\Delta t \in [T/80, T/400]$ and $\Delta t \in [T/256, T/400]$ for DG $\mathbb{P}^2$ and $\mathbb{P}^4$, respectively. All errors are computed with respect to a reference solution obtained for each polynomial degree with the ESDIRK58 scheme and $\Delta t = T/1000$.

Since the Rosenbrock Rod5_1 proves to be the most efficient temporal scheme then it is used for the integration in time over 100 and 60 reference periods T for DG $\mathbb{P}^2$ and $\mathbb{P}^4$ simulations, respectively. The adaptive algorithm is carried out imposing the calibration factor $\tau_\psi = 1$ and an absolute tolerance value τ_a in such a way to verify $\Delta t \approx T/400$ (again the relative tolerance τ_r is set equal to the machine error limit). Moreover for the hybrid stopping criterion

Table 4.9: *Periodic hills - List of local and estimator constants and orders.*

	scheme	ψ_l^1	ψ_r^1	q_l	q_r
$\widetilde{p}$	ESDIRK34	$1.62\text{E}-04$	$1.84\text{E}-05$	4	3
	ESDIRK46	$6.36\text{E}-06$	$2.18\text{E}-06$	5	4
	ESDIRK58	$3.98\text{E}-06$	$1.67\text{E}-06$	6	6
	ROS3PL	$2.38\text{E}-04$	$4.89\text{E}-04$	4	3
	RODASP	$9.18\text{E}-04$	$8.48\text{E}-04$	5	4
	Rod5_1	$6.47\text{E}-05$	$3.62\text{E}-04$	6	5
$\widetilde{T}$	ESDIRK34	$3.80\text{E}-04$	$3.64\text{E}-05$	4	3
	ESDIRK46	$1.18\text{E}-05$	$1.79\text{E}-06$	5	4
	ESDIRK58	$7.70\text{E}-06$	$9.54\text{E}-07$	6	6
	ROS3PL	$3.63\text{E}-04$	$1.98\text{E}-04$	4	3
	RODASP	$1.31\text{E}-03$	$7.91\text{E}-04$	5	4
	Rod5_1	$9.55\text{E}-05$	$2.36\text{E}-04$	6	5
u_1	ESDIRK34	$3.27\text{E}-03$	$4.45\text{E}-04$	4	3
	ESDIRK46	$7.94\text{E}-05$	$1.39\text{E}-05$	5	4
	ESDIRK58	$4.76\text{E}-05$	$5.76\text{E}-06$	6	6
	ROS3PL	$3.11\text{E}-03$	$1.94\text{E}-03$	4	3
	RODASP	$9.85\text{E}-03$	$7.57\text{E}-03$	5	4
	Rod5_1	$7.68\text{E}-04$	$2.35\text{E}-03$	6	5
u_2	ESDIRK34	$5.55\text{E}-03$	$6.70\text{E}-04$	4	3
	ESDIRK46	$1.60\text{E}-04$	$2.55\text{E}-05$	5	4
	ESDIRK58	$8.80\text{E}-05$	$9.87\text{E}-06$	6	6
	ROS3PL	$5.31\text{E}-03$	$2.58\text{E}-03$	4	3
	RODASP	$1.68\text{E}-02$	$1.13\text{E}-02$	5	4
	Rod5_1	$8.14\text{E}-04$	$2.20\text{E}-03$	6	5
u_3	ESDIRK34	$6.13\text{E}-03$	$7.34\text{E}-04$	4	3
	ESDIRK46	$1.58\text{E}-04$	$2.58\text{E}-05$	5	4
	ESDIRK58	$9.97\text{E}-05$	$1.11\text{E}-05$	6	6
	ROS3PL	$5.88\text{E}-03$	$2.84\text{E}-03$	4	3
	RODASP	$1.71\text{E}-02$	$1.18\text{E}-02$	5	4
	Rod5_1	$9.08\text{E}-04$	$2.36\text{E}-03$	6	5

we require one recalculation of the scaling ratio r_s every reference period, *i.e.* $M = 400$. The maximum Courant number obtained with this time integration configuration is $CFL_{max} \approx 180$.

Fig. 4.15 shows the contours of the averaged streamwise velocity for $\mathbb{P}^2$ and $\mathbb{P}^4$ computations. Both discretizations show the expected recirculation bubble and the post-reattachment-recovery region after the hill crest. Fig. 4.14 displays the instantaneous *Q*-criterion for $\mathbb{P}^2$.

In Fig. 4.16, 4.17, 4.18, 4.19, 4.20 and 4.21 are shown respectively the mean velocity $\langle u_1 \rangle / u_b$, $\langle u_2 \rangle / u_b$, the Reynolds stresses $\langle u_1' u_1' \rangle / u_b^2$, $\langle u_2' u_2' \rangle / u_b^2$, $\langle u_1' u_2' \rangle / u_b^2$ and the turbulent kinetic energy $\langle k \rangle / u_b^2$ profiles obtained with DG $\mathbb{P}^2$ and $\mathbb{P}^4$. All the results are obtained by averaging both in time and in spanwise direction. Data comparison is performed with numerical results reported

Figure 4.14: *Periodic hill - Volume rendering of the instantaneous Q criterion field (DG $\mathbb{P}^2$).*

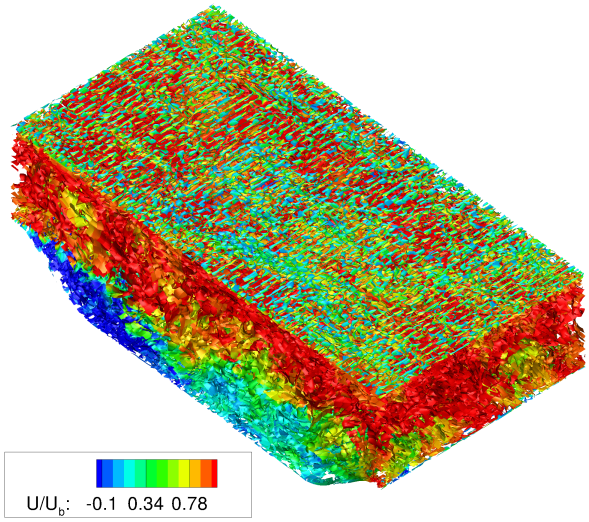

Figure 4.15: *Periodic hill - Averaged streamwise velocity contour.*

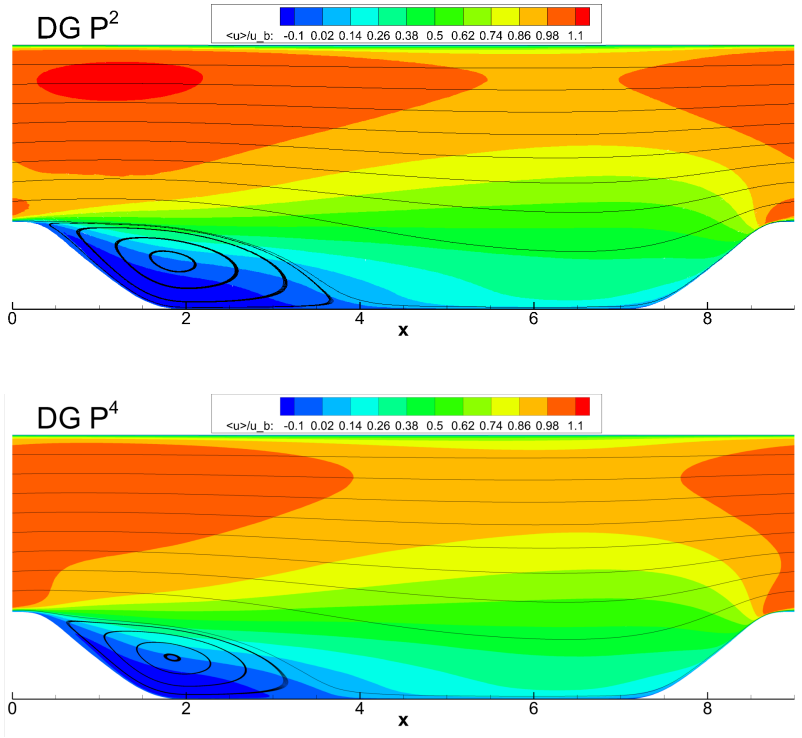

by Breuer *et al.* in [17] and available on ERCOFTAC database. Despite the coarse mesh and the low number of DoFs, a good agreement is achieved with

Figure 4.16: *Periodic hill - Averaged velocity $\langle u_1 \rangle / u_b$ profiles at different positions.*

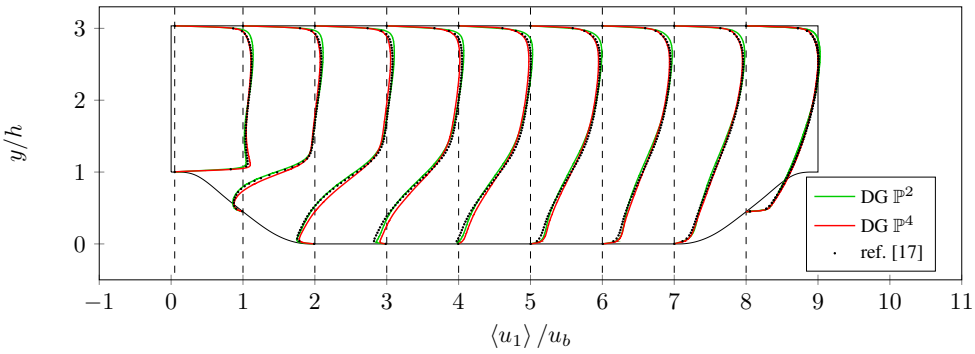

Figure 4.17: *Periodic hill - Amplified averaged velocity $\langle u_2 \rangle / u_b$ profiles at different positions.*

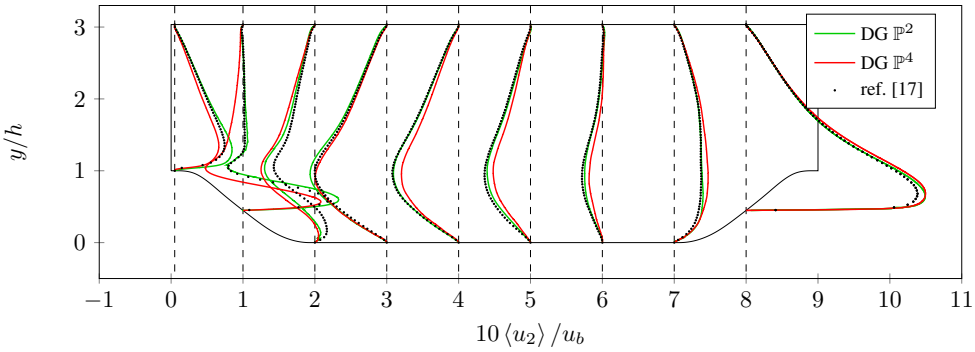

Figure 4.18: *Periodic hill - Amplified Reynolds stresses $\langle u_1' u_1' \rangle / u_b^2$ profiles at different positions.*

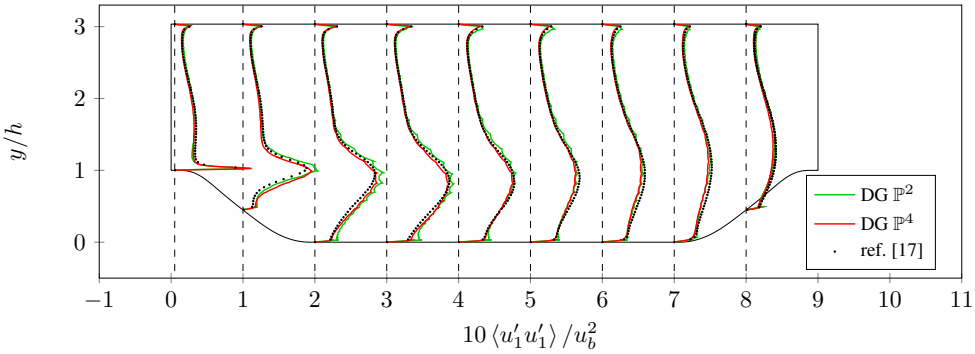

respect to the reference data, especially for the DG $\mathbb{P}^4$ solution. Notice that the vertical velocity, the Reynolds stresses and the turbulent kinetic energy profiles are about one order of magnitude smaller than the streamwise velocity and, thus, they are here amplified when shown in figures for the sake of comprehension. As a consequence, also the discrepancies with respect to the

Figure 4.19: *Periodic hill - Amplified Reynolds stresses $\langle u_2' u_2' \rangle / u_b^2$ profiles at different positions.*

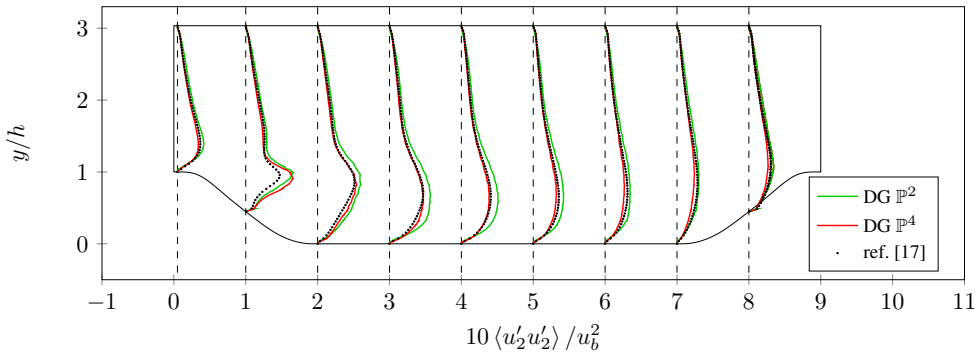

Figure 4.20: *Periodic hill - Amplified Reynolds stresses $\langle u_1' u_2' \rangle / u_b^2$ profiles at different positions.*

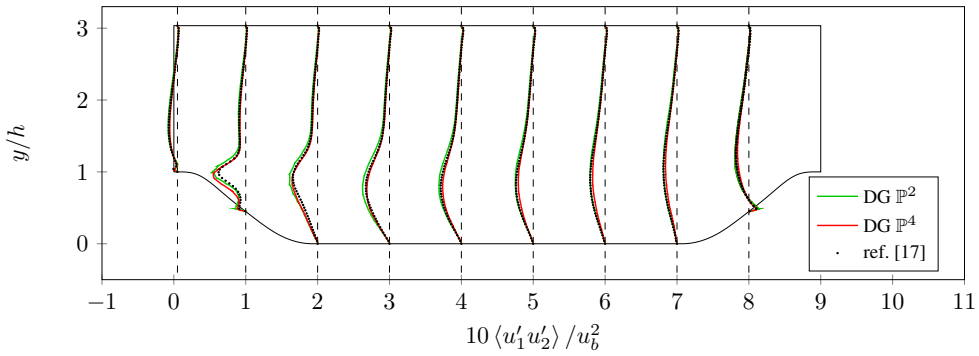

Figure 4.21: *Periodic hill - Amplified turbulent kinetic energy $\langle k \rangle / u_b^2$ profiles at different positions.*

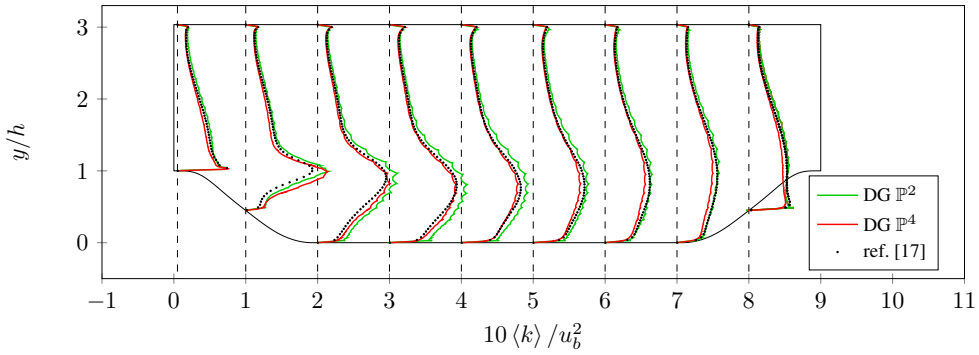

reference solution are amplified.

Finally, in Tab. 4.10 we report the time integration performance improvements obtained for the periodic hill test case. Thanks to the strategies devel-

Table 4.10: *Periodic hills - Time integration efficiency enhancements in terms of GMRES iteration reduction ($\Delta_{\%}It_{GMRES}$), wall time reduction ($\Delta_{\%}t_{wall}$), speedup, CPU hours saving (h_{CPU}) and man hours saving (h_{man}) obtained applying all numerical strategies developed in this work to the Rod5_1 scheme for DG $\mathbb{P}^2$ and $\mathbb{P}^4$ polynomial approximations.*

	$\Delta_{\%}It_{GMRES}$	$\Delta_{\%}t_{wall}$	speedup	h_{CPU}	h_{man}
$\mathbb{P}^2$	-54.08	-15.51	1.18	$6\,200$	6
$\mathbb{P}^4$	-59.21	-9.71	1.11	$40\,908$	40

oped in this work, for the DG $\mathbb{P}^2$ computation we are able to reduce the total number of GMRES iterations more than 50% and the global computational time of $\approx 15\%$, thus leading to a speedup of 1.18. Moreover, the total number of saved CPU hours is $6\,200$, corresponding to 6 man hours (here we used 1024 cores). For the DG $\mathbb{P}^4$ simulation, we obtain a lower computational time reduction ($\approx 10\%$) and speedup (1.11) because of the higher cost of the Jacobian matrix computation. However, we achieve the remarkable a CPU hours saving of $40\,908$ and a man hours saving of 40.

CHAPTER 5

Numerical results: part B

In this chapter we want to show the potential of the proposed Discontinuous Galerkin approach to the simulation of incompressible multicomponent free surface flows. The advection of an inviscid squared drop and the dry bed inviscid dambreak problem are here analysed. Moreover in order to illustrate the possibility of the proposed DG formulation to perform simulations with more than two fluids, a dry bed inviscid double-dambreak problem is here introduced and solved.

All simulations are performed with a Backward Euler (BE) scheme. Here, all the approaches proposed in Chap. 3 are applied considering for simplicity $\psi_l = \psi_r = 1$ for each working variable. Furthermore, for hybrid stopping criterion we require $M = 25$ and for adaptive algorithm $\tau_\psi = 1$, $\tau_a = 0.005$ and $\tau_r = \varepsilon$.

5.1 Advection of a square drop

This 2D test case consists of the advection of a square liquid drop inside a gas. Pressure and velocity fields are considered unitary in whole the doubly-periodic square domain $[0, 10] \times [0, 10]$. The drop, placed at $(5, 5)$ at time $t^0 = 0$, has the initial dimension of $(1.25, 1.25)$ and moves on the diagonal of the domain thus completing one advection period in $T = 10$ convective times. Drop density is imposed unitary $\rho_l = 1$ while gas density $\rho_g = \rho_l / r_\rho$ is defined

Figure 5.1: *Square drop - Mesh and initial density ρ field.*

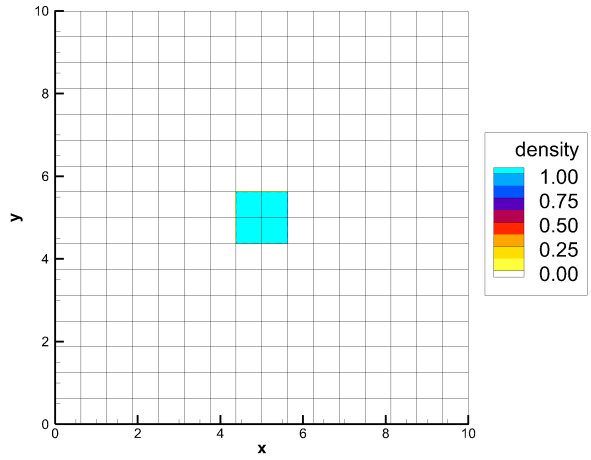

Figure 5.2: *Square drop - Density ρ iso-lines after one period T.*

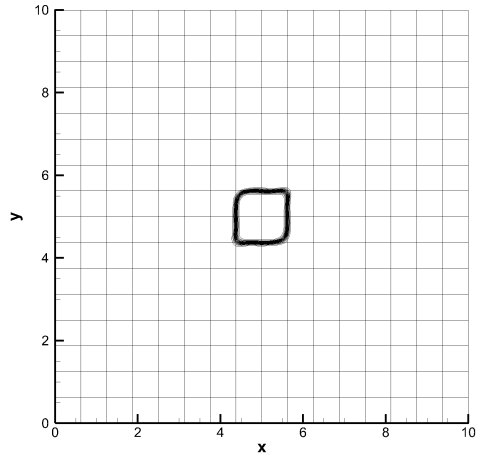

by means of the density ratio kept here equal to $r_\rho = 816.33$, *i.e.* water-air density ratio. Solutions are computed using a $\mathbb{P}^6$ DG polynomial discretization on a uniform 16×16 quad mesh hence ensuring an exact projection of the initial working density $\widetilde{\rho}$ field (see Fig. 5.1).

The solution performed at the output time $t^N = T$ is shown in Fig. 5.2. Despite the large dimension of mesh elements, the small quantity of the numerical diffusion introduced by the local artificial viscosity allows to capture the interface as a very thin layer with continuous sharp gradients. Moreover, in Fig. 5.3 are shown the working density and density profiles along the domain diagonal $x = y$. Thanks to the proposed change of variables, the density is positive and under/overshoots are strongly limited. As a result, the overall shape of the drop is well preserved. Finally, solving each BE non-linear system at the machine

Figure 5.3: *Square drop - Working density $\widetilde{\rho}$ and density ρ profiles on the domain diagonal after one period T.*

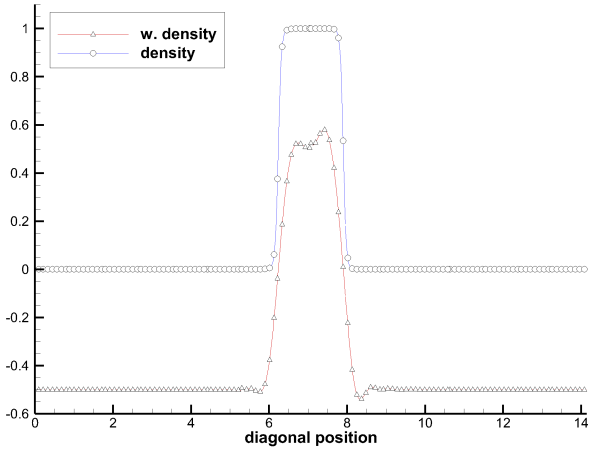

Table 5.1: *Square drop - Working variables field errors.*

$\|err_p^N\|$	$\|err_{u_1}^N\|$	$\|err_{u_2}^N\|$	$\|err_{\widetilde{\rho}}^N\|$
8.64e−14	7.21e−12	6.86e−12	3.98e+00

error limit no appreciable variation on pressure and velocity fields are found, as reported in Tab. 5.1 where errors are defined with respect to the available exact solution.

5.2 Dry bed inviscid dambreak problem

The dambreak problem over a dry bed is a classical free surface problem that consists on a collapse of a vertical wall that separates water from air. An exact solution of the shallow water (SW) model has been already derived for this test case by Ritter [57] in 1892.

Following the problem set-up proposed by Dumbser [29], the domain $[-50, 50] \times [0, 4]$ initially contains liquid in the region $[-50, 0] \times [0, 1.4618]$. The body acceleration is set according to the gravity constant and velocity components are imposed null thus requiring an hydrostatic initial pressure profile. Again we consider the water-air density ratio with a unitary liquid density. Transmissive condition is applied to the top boundary and no-slip wall condition is considered for remaining borders. Solutions are computed using a $\mathbb{P}^6$ DG polynomial discretization on the 260×8 and 520×16 meshes generated in order to ensure the exact projection on the polynomial space of the initial working density field (see Fig. 5.4).

In Figs. 5.5 results obtained for both meshes are compared with the exact solution of the shallow water model at convective time $t = 5$. An ex-

Figure 5.4: *Dambreak - Meshes zoom for $x \in [-5, 5]$ and initial density ρ contour.*

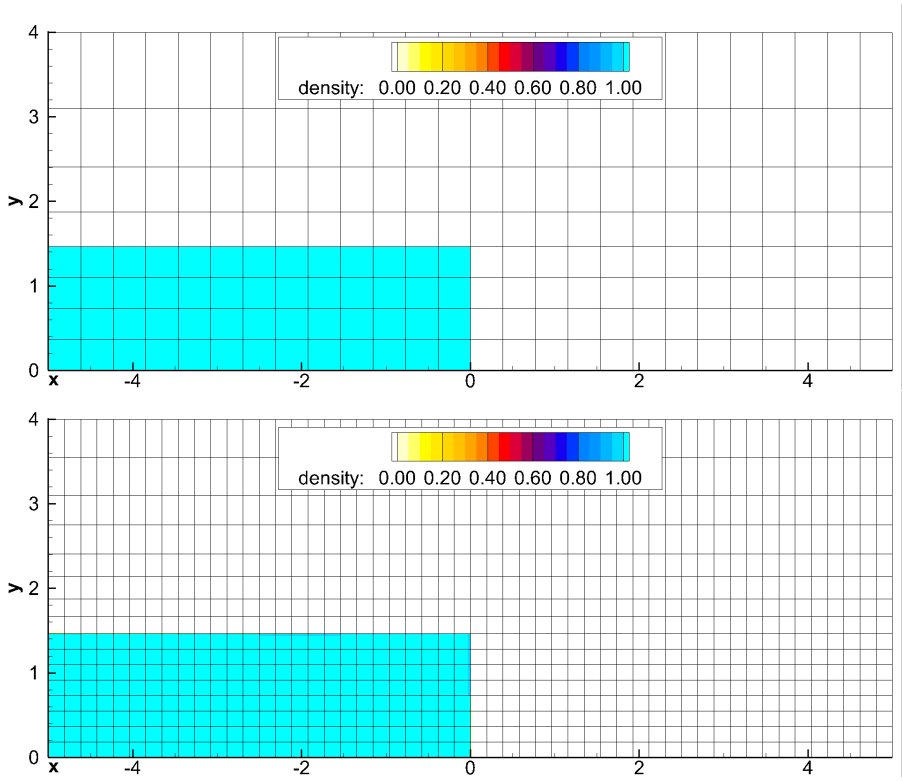

cellent agreement is achieved in terms of the free surface position except for the predicted position of the liquid front which is moved forward in the shallow water solution. This behaviuor is explained by the fact that shallow water equations assume that vertical accelerations are negligible compared with horizontal ones [28]. As a consequence, the exact solution shows a maximum velocity, $|u|_{max} = 2\sqrt{gH}$ with H the liquid high, constant in time and thus it predicts a faster moving liquid front in early times.

5.3 Dry bed inviscid double-dambreak problem

In order to show the capabilities of the proposed DG variable density incompressible formulation to deal with more than two fluids we perform a dambreak problem with two different liquids and one gas. The gas and the first liquid are again air and water meanwhile the last fluid is a liquid with an intermediate density, *i.e.* the arithmetic mean value of air and water densities. For the sake of simplicity, the last fluid is here named oil. This test case is challenging since entails both high (water-air, oil-air) and low (water-oil) density ratio interactions.

Figure 5.5: *Dambreak - Comparison of coarse and fine mesh results with respect to the exact shallow water solution at convective time $t = 5$ in terms of free surface position and velocity component u_1 profiles at bottom boundary.*

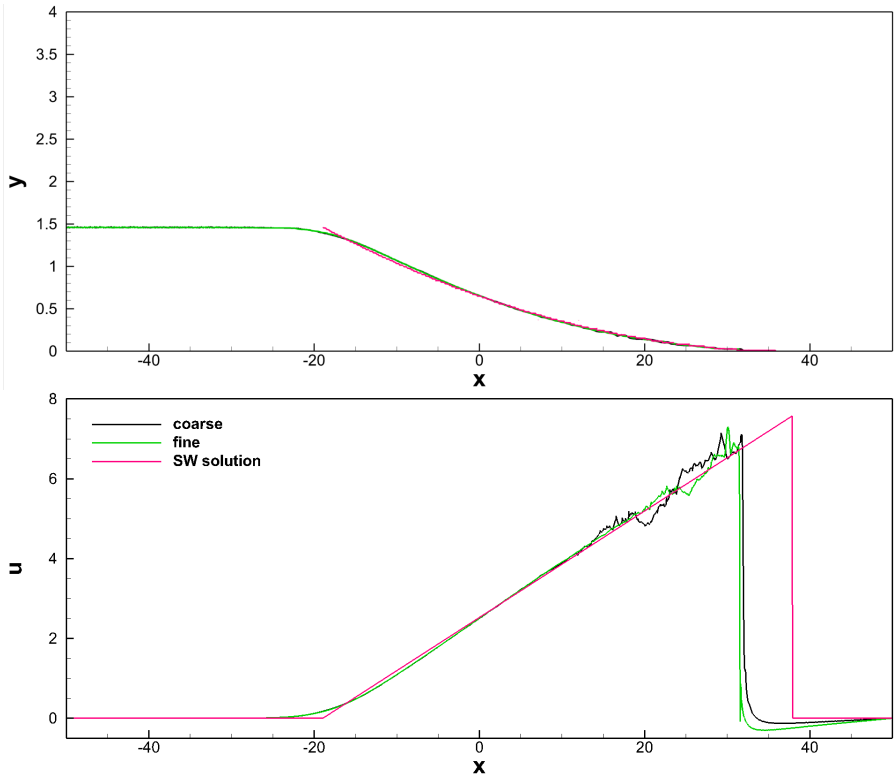

The domain $[-5, 5] \times [0, 8]$ contains two liquid regions $[-5, -3.8] \times [0, 3.6]$ and $[3.8, 5] \times [0, 3.6]$ for water and oil, respectively, while the remaining part is filled by the air. Null velocity component fields and hydrostatic pressure profile are imposed as initial conditions and no-slip wall condition is applied to all boundaries. Solutions are computed using a $\mathbb{P}^6$ DG polynomial approximation on a coarse 25×20 and a fine 50×40 mesh. At start time, the projection on the polynomial space of the working density is exact.

Since no references are available on this test case, we only show and analyse the evolution in time of the double-dambreak problem. In Fig. 5.6 are reported density contours at chosen times for both coarse and fine mesh computations. At early times the problem evolves as a classical single dambreak until liquid fronts collide ($t = 0.25$). As a consequence a wave of both water and oil rises till reaching the maximum hight roughly at $t = 0.5$. After that, in the meantime that the wave collapses on itself incorporating a small air bubble, the water front goes forward into the oil region.

Despite the large elements dimension, thanks to the high order DG approx-

imation the coarse mesh is able to capture quite well the interface evolution in time. Nevertheless, finer mesh provides better spatial resolutions which allow to detect smaller flow features.

Figure 5.6: *Double-dambreak - Density ρ contour at different times for coarse (left) and fine (right) meshes. Blue is water and red is oil.*

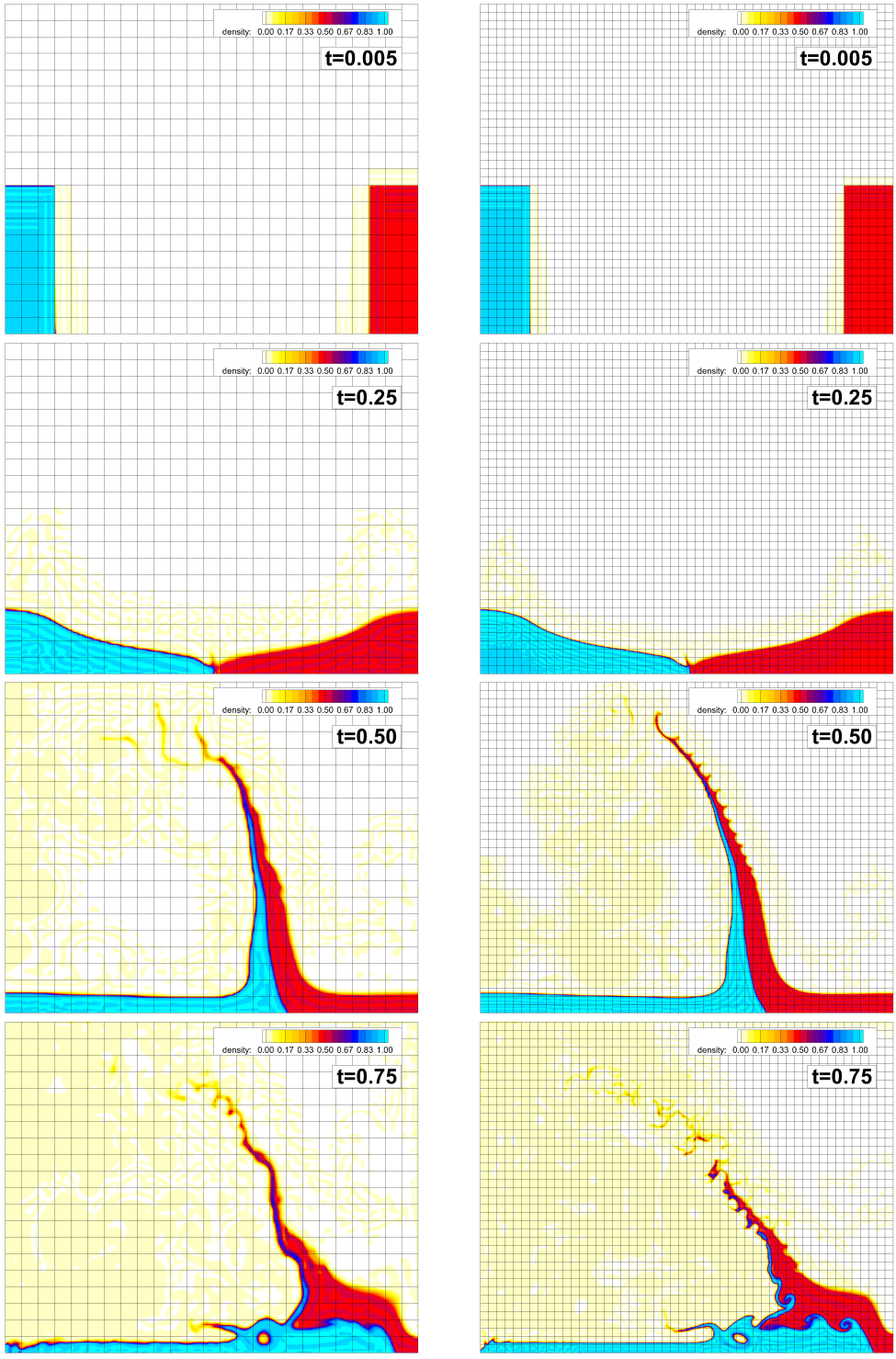

Conclusions

In this work we developed, improved and implemented several numerical approaches for the robustness and efficiency enhancement of the implicit high-order time integration performed by means ESDIRK and Rosenbrock schemes. A new starting procedure able to preserve the theoretical order of accuracy for multi-step Peer methods is derived as well.

The efficiency of the proposed numerical strategies have been exhaustively examined on compressible and incompressible benchmark test cases and finally demonstrated by computing the implicit Large Eddy simulation of the massively separated compressible flow over periodic hills at $\mathrm{Re}_h = 10595$.

Furthermore, we proposed a high-order Discontinuous Galerkin method for the simulation of variable density incompressible flows which is able to treat interface problems in a diffuse fashion. More in detail, a change of variables is introduced in order to ensure the density positivity and limit under/overshoots, a local artificial viscosity approach is applied to handle spurious density oscillations that occur at interfaces, and an exact Riemann solver based on the artificial compressibility approach is derived for the inviscid interface flux treatment.

Promising results on numerical experiments involving high-density ratios (water-air) and the possible interaction of more than two fluids have been obtained using a very high-order polynomial representation of the solution on relatively coarse grids.

Bibliography

[1] D. N. Arnold, F. Brezzi, B. Cockburn, and L. D. Marini. Unified analysis of discontinuous Galerkin methods for elliptic problems. *SIAM J. Numer. Anal.*, 39(5):1749–1779, 2002.

[2] S. Balay, S. Abhyankar, M. F. Adams, J. Brown, P. Brune, K. Buschelman, L. Dalcin, V. Eijkhout, W. D. Gropp, D. Kaushik, M. G. Knepley, L. C. McInnes, K. Rupp, F. Barry, K. R. Smith, S. Zampini, and H. Zhang. PETSc Web page. `http://www.mcs.anl.gov/petsc`, 2016.

[3] F. Bassi, L. Botti, A. Colombo, A. Crivellini, A. Ghidoni, A. Nigro, and S. Rebay. Time integration in the Discontinuous Galerkin code MIGALE - Unsteady problems. 2014. *in press*.

[4] F. Bassi, L. Botti, A. Colombo, D. A. Di Pietro, and P. Tesini. On the flexibility of agglomeration based physical space discontinuous Galerkin discretizations. *J. Comput. Phys.*, 231(1):45 – 65, 2012.

[5] F. Bassi, L. Botti, A. Colombo, A. Ghidoni, and F Massa. Linearly implicit Rosenbrock-type Runge-Kutta schemes for the Discontinuous Galerkin solution of compressible and incompressible unsteady flows. *Computers & Fluids*, 118:305–320, 2015.

[6] F. Bassi, A. Crivellini, D. A. Di Pietro, and S. Rebay. An artificial compressibility flux for the discontinuous Galerkin solution of the incompressible NavierStokes equations. *Journal of Computational Physics*, 218(2):794 – 815, 2006.

[7] F. Bassi, A. Crivellini, D. A. Di Pietro, and S. Rebay. An implicit high-order discontinuous Galerkin method for steady and unsteady incompressible flows. *Comput. Fluids*, 36:1529–1546, 2007.

[8] F. Bassi, A. Crivellini, S. Rebay, and M. Savini. Discontinuous Galerkin solution of the Reynolds-averaged Navier-Stokes and k-ω turbulence model equations. *Comput. Fluids*, 34:507–540, 2005.

[9] F. Bassi, C. De Bartolo, R. Hartmann, and A. Nigro. A discontinuous Galerkin method for inviscid low Mach number flows. *J. Comput. Phys.*, 228(11):3996 – 4011, 2009.

[10] F. Bassi and S. Rebay. A high order discontinuous Galerkin method for compressible turbulent flows. In *Discontinuous Galerkin Methods. Theory, Computation and Applications*, volume 11 of *Lecture Notes in Computational Science and Engeneering*, pages 77–88. Springer-Verlag, 2000. First Internation Symposium on Discontinuous Galerkin Methods, May 24–26, 1999, Newport, RI, USA.

[11] F. Bassi, S. Rebay, G. Mariotti, S. Pedinotti, and M. Savini. A high-order accurate discontinuous finite element method for inviscid and viscous turbomachinery flows. In R. Decuypere and G. Dibelius, editors, *Proceedings of the 2nd European Conference on Turbomachinery Fluid Dynamics and Thermodynamics*, pages 99–108, Antwerpen, Belgium, March 5–7 1997. Technologisch Instituut.

[12] A.D. Beck, T. Bolemann, D. Flad, H. Frank, G.J. Gassner, F. Hindenlang, and C.-D. Munz. High-order discontinuous galerkin spectral element methods for transitional and turbulent flow simulations. *Internat. J. Numer. Methods Fluids*, 76(8):522–548, 2014.

[13] C. Benocci and A. Pinelli. The role of the forcing term in the large eddy simulation of equilibrium channel flow. *Engineering Turbulence Modeling and Experiments*, pages 287–296, 1990.

[14] D.S. Blom, P. Birken, H. Bijl, F. Kessels, A. Meister, and A.H. van Zuijlen. A comparison of rosenbrock and esdirk methods combined with iterative solvers for unsteady compressible flows, 06 2016.

[15] P.D. Boom and D.W. Zingg. Time-accurate flow ssimulation using an efficient newton-krylov-schur approach with high-order temporal and spatial discretization. Grapevine (Dallas/Ft. Worth Region), Texas, January 2013. 51st AIAA Aerospace Sciences Meetin including the New Horizon Forum and Aerospace Exposition.

[16] L. Botti. Influence of reference-to-physical frame mappings on approximation properties of discontinuous piecewise polynomial spaces. *J. Sci. Comput.*, pages 1–29, 2011.

[17] M. Breuer, N. Peller, Ch. Rapp, and M. Manhart. Flow over preriodic hills - numerical and experimental study in a wide range of reynolds numbers. *Computers & Fluids*, 38:433–457, 2009.

[18] F. Brezzi, G. Manzini, D. Marini, P. Pietra, and A. Russo. Discontinuous Galerkin approximations for elliptic problems. *Numer. Meth. Part. D. E.*, 16:365–378, 2000.

[19] C. Carton de Wiart, K. Hillewaert, M. Duponcheel, and G. Winckelmans. Assessment of a discontinuous Galerkin method for the simulation of vortical flows at high Reynolds number. *Int. J. Numer. Methods Fluids*, 74(7):469–493, 2014.

[20] J. R. Cash. On the integration of stiff systems of O.D.E.s using Extended Backward Differentiation Formulae. *Numerische Mathematik*, (34):235–246, 1980.

[21] J. R. Cash. The integration of stiff initial value problems in ODEs using Modified Extended Backward Differentiation Formulae. *Computers & Mathematics with Applications*, 5(9):645–657, 1983.

[22] J.-B. Chapelier, M. de la Llave Plata, F. Renac, and E. Lamballais. Evaluation of a high-order discontinuous Galerkin method for the {DNS} of turbulent flows. *Comput. Fluids*, 95(0):210 – 226, 2014.

[23] Y.-H. Choi and C. L. Merkle. The application of preconditioning in viscous flows. *J. Comput. Phys.*, 105(2):207 – 223, 1993.

[24] A. Crivellini, V. D'Alessandro, and F. Bassi. A Spalart-Allmaras turbulence model implementation in a discontinuous Galerkin solver for incompressible flows. *J. Comput. Phys.*, 241:388–415, 2013.

[25] G. Di Marzo. RODAS5(4) - Méthodes de Rosenbrock d'ordre 5(4) adaptées aux problemes différentiels-algébriques. *MSc Mathematics Thesis; Faculty of Science, University of Geneva, Switzerland*, 1993.

[26] D. A. Di Pietro and A. Ern. *Mathematical Aspects of Discontinuous Galerkin Methods*, volume 69 of *Mathématiques et Applications*. Springer-Verlag, 2012.

[27] V. Dolejší. Semi-implicit interior penalty discontinuous Galerkin methods for viscous compressible flows. *Commun. Comput. Phys.*, 4:231–274, 2008.

[28] F. Dressler. Comparison of theories and experiments for the hydraulic dam-break wave. *Proc. Intl Assoc. of Scientific Hydrology Assemblée Générale*, 3(38):319–328, 1954.

[29] M. Dumbser. A simple two-phase emethod for the simulation of complex free surface flows. *Comput. Meth. Appl. Mech. Engng.*, 200:1204–1219, 2011.

[30] S.C. Eisenstat and H.F. Walker. Choosing the forcing terms in an inexact newton method. *SIAM Journal on Scientific Computing*, 17:16–32, 1994.

[31] D. T. Elsworth and E. F. Toro. Riemann solvers for solving the incompressible navier-stokes equations using the artificial compressibility method. Technical Report 9208, College of Aeronautics, Cranfield Institute of Technology, 1992.

[32] J. Frohlich, J. M. Melenk, W. Rodi, L. Temmerman, and M.A. Leschziner. Highly resolved large-eddy simulation of separated flow in a channel with streamwise periodic constrictions. *Journal of Fluid Mechanics*, 526:19–66, 2005.

[33] G. J. Gassner, F. Lörcher, and C.-D. Munz. A discontinuous Galerkin scheme based on a space-time expansion II. Viscous flow equations in multi dimensions. *J. Sci. Comput.*, 34:260–286, 2008.

[34] A. Gerisch, J. Lang, H. Podhaisky, and R. Weiner. High-order linearly implicit two-step perr - finite element methods for time-dependent pdes. *Applied Numerical Mathematics*, 59:624 – 638, 2009.

[35] J. J. Gottlieb and C. P. T. Groth. Assessment of Riemann solvers for unsteady one-dimensional inviscid flows of perfect gases. *J. Comput. Phys.*, 78:437–458, 1988.

[36] J.-L. Guermond and A. Salgado. A splitting method for incompressible flows with variable density based on a pressure poisson equation. *Journal of Computational Physics*, 228(8):2834–2846, 2008.

[37] E. Hairer and G. Wanner. *Solving ordinary differential equations II*. Springer Verlag, 2010.

[38] R. Hartmann, J. Held, and T. Leicht. Adjoint-based error estimation and adaptive mesh refinement for the RANS and k-ω turbulence model equations. *J. Comput. Phys.*, 230:4268–4284, 2011.

[39] J. S. Hesthaven and T. Warburton. *Nodal Discontinuous Galerkin Methods*. Springer, 2008.

[40] C. Hu and C.-W. Shu. Weighted essentially non-oscillatory schemes on triangular meshes. *J. Comput. Phys.*, 150(1):97–127, 1999.

[41] G. S. Iannelli and A. J. Baker. A stiffly-stable implicit Runge-Kutta algorithm for CFD applications. AIAA Paper 88-0416, 1988.

[42] J. Jaffre, C. Johnson, and A. Szepessy. Convergence of the discontinuous Galerkin finite element method for hyperbolic conservation laws. *Math. Models Methods Appl. Sci*, 5(3):367–286, 1995.

[43] C. A. Kennedy and M. H. Carpenter. Additive runge-kutta schemes for convection-diffusion-reaction equations. Technical Report TM-2001-211038, NASA, 2001.

[44] Andreas Klöckner, Timothy Warburton, and Jan S Hesthaven. Viscous shock capturing in a time-explicit discontinuous galerkin method. *Math. Model. Nat. Phenom.*, 6(3):57 – 83, 2011.

[45] D.A. Knoll and D.E. Keyes. Jacobian-free Newton-Krylov methods: a survey of approaches and applications. *J. Comput. Phys.*, 193(2):357–397, 2004.

[46] J. Lang and D. Teleaga. Towards a fully space-time adaptive fem for magnetoquasistatics. *IEEE Transactions on Magnetics*, 44(6):1238–1241, June 2008.

[47] P. L. Lions. *Mathematical topics in fluid mechanics - Vol. 1 Incompressible models*. The Clarendon Press, Oxford University Press, 1996.

[48] F. Massa, G. Noventa, Bassi F., A. Colombo, A. Ghidoni, and M. Lorini. High-order linearly implicit two-step peer methods for the discontinuous galerkin solution of the incompressible rans equations. In *ECCOMAS Congress 2016, VII European Congress on Computational Methods in Applied Sciences and Engineering*, volume 2, pages 2664–2683. National Technical University of Athens, June 2016.

[49] C.P. Mellen, J. Frohlich, and W. Rodi. Large eddy simulation of the flow over periodic hills. In *16th IMACS World Congress*, 2000.

[50] A. Nigro, C. De Bartolo, F. Bassi, and A. Ghidoni. Up to sixth-order accurate A-stable implicit schemes applied to the discontinuous Galerkin discretized Navier-Stokes equations. *J. Comput. Phys.*, under review, 2014.

[51] A. Nigro, A. Ghidoni, S. Rebay, and F. Bassi. Modified Extended BDF scheme for the discontinuous Galerkin solution of unsteady compressible flows. *Int. J. Numer. Methods Fluids*, under review, 2014.

[52] G. Noventa, F. Massa, F. Bassi, A. Colombo, N. Franchina, and A. Ghidoni. A high-order discontinuous galerkin solver for unsteady incompressible turbulent flows. *Computers & Fluids*, 139:248–260, November 2016.

[53] Per-Olof Persson and Jaime Peraire. Sub-cell shock capturing for discontinuous galerkin methods. *44th AIAA Aerospace Sciences Meeting and Exhibit. Reno, Nevada*, 2006.

[54] H. Podhaisky, R. Wiener, and B.A. Schmitt. Rosenbrock-type 'peer' two-step methods. *Applied Numerical Mathematics*, 53, 2005.

[55] G.-Y. Psihoyios and J.R. Cash. A stability result for general linear methods with characteristic function having real poles only. *BIT Numerical Mathematics*, 38(3):612–617, 1998.

[56] W. H. Reed and T. R. Hill. Triangular mesh methods for the neutron transport equation. Report LA-UR-73-479, Los Alamos Scientific Laboratory, 1973.

[57] A. Ritter. Die fortpflanzung der wasserwellen. *Z. Ver. Deut. Ing*, 36:947–954, 1892.

[58] G. Söderlind. Digital Filters in Adaptive Time-Stepping. *ACM Transactions on Mathematical Software*, pages 1–24, 2005.

[59] G. Söderlind and L. Wang. Adaptive time-stepping and computational stability. *J. Comput. and App. Math.*, 185:225–243, 2006.

[60] G. Steinebach. Order-reduction of ROW-methods for DAEs and method of lines applications. Preprint-Nr. 1741, FB Mathematik, TH Darmstadt, 1995.

[61] P. Tesini. *An* h*-Multigrid Approach for High-Order Discontinuous Galerkin Methods*. PhD thesis, University of Bergamo, Bergamo, Italy, January 2008.

[62] A. Uranga, P.-O. Persson, M. Drela, and J. Peraire. Implicit Large Eddy Simulation of transition to turbulence at low reynolds numbers using a Discontinuous Galerkin method. *International Journal for Numerical Methods in Engineering*, 87(1-5):232–261, 2011.

[63] Fedderik van der Bos and Bernard J. Geurts. Computational error-analysis of a discontinuous Galerkin discretization applied to large-eddy simulation of homogeneous turbulence. *Computer Methods in Applied Mechanics and Engineering*, 199(1316):903 – 915, 2010.

[64] J. Von Neumann and R.D. Richtmyer. A method for the numerical calculation of hydrodynamic shocks. *Journal of Computational Physics*, 21:232–237, 1950.

[65] Liang Wei and Andrew Pollard. Direct numerical simulation of compressible turbulent channel flows using the discontinuous galerkin method. *Comput. Fluids*, 47(1):85 – 100, 2011.

[66] J. M. Weiss and W. A. Smith. Preconditioning applied to variable and constant density flows. *AIAA J.*, 33(11):2050–2057, 1995.